M 2018

U.PORTO
FEUP FACULDADE DE ENGENHARIA
UNIVERSIDADE DO PORTO

# NUMERICAL ANALYSIS OF THE VORTICAL FLOW AND AERODYNAMIC BEHAVIOR OF A GENERIC DOUBLE DELTA WING WITH NEGATIVE LEADING EDGE STRAKES

**REBECA NUNES MARINI**

DISSERTAÇÃO DE MESTRADO APRESENTADA
À FACULDADE DE ENGENHARIA DA UNIVERSIDADE DO PORTO EM
MESTRADO DE MÊCANICA COMPUTACIONAL

UNIVERSIDADE DO PORTO




# Numerical analysis of the vortical flow and aerodynamic behavior of a generic double delta wing with negative leading edge strakes

by

**Rebeca Nunes MARINI**

Supervisor at FEUP:
Prof. Doutor João Pedro PÊGO
Mechanical Engineering Department

Supervisor at DLR:
Dr. -Ing. Andreas SCHÜTTE
Institute of Aerodynamics and Flow Technology

*A thesis submitted in fulfillment of the requirements for the degree of Master in Engineering*

*in the*

Master in Computational Mechanics
Faculdade de Engenharia da Universidade do Porto

*"Sometimes science is a lot more art than science. A lot of people don't get that."*

Rick Sanchez, *Rick & Morty*

# Resumo

Esta Tese foi realizada no Instituto de Aerodinâmica e Tecnologia de Escoamento (Aerodynamik und Strömungstechnik) do Centro Aeroespacial Alemão (DLR-Deutsches Zentrum für Luft- und Raumfahrt). O principal objetivo é a análise da física topológico do escoamento em torno de uma asa genérica duplo delta com **strakes** negativos. Para isso foram realizadas várias simulações computacionais usando o **DLR RANS solver TAU**. Foram conduzidos três estudos: de sensibilidade de malha, de sensibilidade de modelo de turbulência e de validação através de dados experimentais. O objetivo é avaliar as sensibilidades quanto à topologia do escoamento, dependendo da malha computacional e do modelo de turbulência. Finalmente, deve ser fornecida uma melhor prática de qual abordagem de malha e escolha do modelo númerico que melhor representar a física do escoamento e características aerodinâmicas em comparação com os dados experimentais. Foi concluído que, para o caso simulado na presente tese, o modelo de turbulência que melhor se adequa foi o *Reynolds Stress Model*.

# Abstract

This Thesis has been conducted at the German Aerospace Center (DLR-Deutsches Zentrum für Luft- und Raumfahrt) at the Institute of Aerodynamics and Flow Technology (Aerodynamik und Strömungstechnik). The main objective is the analysis of the flow topology physics on a generic double delta wing with negative strakes. For this, several computational simulations using the DLR RANS solver TAU have been performed. Three computational studies have been conducted: a grid sensitivity study, a turbulence model sensitivity study and a validation study by use of experimental data. The aim is to evaluate the sensitivities regarding the flow topology depending on the computational grid and turbulence model. Finally, a best practice should provide which grid approach and choice of the numerical model has the best representation of the flow physics and aerodynamic characteristics in comparison with the experimental data. It has been concluded that Reynolds Stress Model presented quantitatively and qualitatively the most accurate results.

# *Acknowledgements*

I would like to thank Dr.-Ing. Andreas Schütte for his guidance and Prof. Dr. João Pedro Pêgo for his accompagnement. This thesis was only academically and personally possible by the supervision of both from beginning to end.

The on going support from my sisters throughout the writing process and my whole Family for their unconditional love and steering enabled a successful thesis.

Lastly, I want to thank João for his encouragement and patience for the whole duration of my exchange program.

# Contents

**Abstract** **v**

**Acknowledgements** **vii**

**Contents** **ix**

**1 Introduction** **1**

**2 Delta Wing Aerodynamics** **7**

**3 Model Configuration** **15**

**4 Numerical Method** **19**
4.1 DLR RANS Methods TAU . . . . . 19
4.2 Turbulence Models . . . . . 21
4.3 Numerical Approach . . . . . 23

**5 Grid Generation** **27**

**6 Experimental Case Study** **33**

**7 Computational Results** **37**
7.1 Grid sensitivity study . . . . . 37
7.2 Turbulence model sensitivity study . . . . . 39
7.3 Reynolds Number Effect . . . . . 43
7.4 Experimental data comparison . . . . . 45

**8 Conclusion and Further Work** **59**

**References** **61**

**List of Figures** **63**

**List of Tables** **67**

**A Results** **69**

# Nomenclature

| | | | |
|---|---|---|---|
| $A_{ref}$ | $[m^2]$ | Wing reference area | |
| $a$ | $[m/s]$ | Speed of sound | |
| $b$ | $[m]$ | Wing span | |
| $c_{ref}$ | $[m]$ | Wing reference length | |
| $c_p$ | $[-]$ | Pressure coefficient | $(p - p_\infty)/q_\infty$ |
| $C_L$ | $[-]$ | Lift coefficient | $L/(q_\infty \cdot A_{ref})$ |
| $C_D$ | $[-]$ | Drag coefficient | $D/(q_\infty \cdot A_{ref})$ |
| $C_m$ | $[-]$ | Pitching moment coefficient | $m/(q_\infty \cdot A_{ref} \cdot c_{ref})$ |
| $C_l$ | $[-]$ | Rolling moment coefficient | $l/(q_\infty \cdot A_{ref} \cdot c_{ref})$ |
| $M_\infty$ | $[-]$ | Mach number | $V_\infty/a$ |
| $p$ | $[N/m^2]$ | Pressure | |
| $Re_\infty$ | $[-]$ | Reynolds number | $\rho \cdot V_\infty \cdot c_{ref}/\mu$ |
| $q_\infty$ | $[-]$ | Dynamic pressure coefficient | $\rho_\infty \cdot V_\infty^2/2$ |
| $V_\infty$ | $[-]$ | Velocity | |
| $y^+$ | $[-]$ | dimensionless wall distance | $(y \cdot \sqrt{\tau/\rho})/\nu$ |
| $\alpha$ | $[^\circ]$ | Angle of attack | |
| $\beta$ | $[^\circ]$ | Angle of sideslip | |
| $\triangle\alpha$ | $[^\circ]$ | Angle of attack amplitude | |
| $\mu$ | $[Nm/s^2]$ | Dynamic viscosity | |
| $\nu$ | $[m^2/s]$ | Kinematic viscosity | |
| $\rho$ | $[kg/m^3]$ | Density | |
| $ref$ | | Reference parameter | |
| $\infty$ | | Far field condition | |
| $\tau$ | $[Nm^2]$ | Wall friction | |

| | |
|---|---|
| **AVT** | **A**pplied **V**ehicle **T**echnology Panel |
| **AoA** | **A**ngle **o**f **A**ttack |
| **CAD** | **C**omputer **A**ided **D**esign |
| **C²A²S²E²** | **C**enter for **C**omputer **A**pplications in **A**erospace **S**cience and **E**ngineering |
| **CFD** | **C**omputational **F**luid **D**ynamics |
| **DLR** | **D**eutsches Zentrum für **L**uft- und **R**aumfahrt |
| **LE** | **L**eading **E**dge |
| **LEVCON** | **L**eading **E**dge **V**ortex **CON**trol |
| **MRP** | **M**oment **R**eference**P**oint |
| **NATO** | **N**orth **A**tlantic **T**reaty **O**rganization |
| **PSP** | **P**ressure **S**ensitive **P**aint |
| **RANS** | **R**eynolds **A**veraged **N**avier-**S**tokes |
| **RMS** | **R**eynolds **S**tress **M**odel |
| **SA** | **S**palart-**A**llmaras turbulence model |
| **STO** | **S**cience and **T**echnology **O**rganization |
| **TE** | **T**railing **E**dge |

# Chapter 1

# Introduction

## Background

A combat aircraft, such as a fighter, needs to meet certain performance requirements, namely manoeuvrability and agility in sub-, trans- and supersonic flight. Identification and prediction of in-flight flow situations, that could compromise the aircraft's performance is essential in the design process. As technology advances, computational fluid dynamics (CFD) is progressively included in this process, allowing for a better understanding of in-flight flow behaviour. The flow separation, vortex formation and vortex systems interactions are some examples of flow physics that have knowledge gaps (Hitzel, 2017).

Several national research programs have been established at DLR in Germany for studies regarding these matters, as well as international cooperation groups. These research task groups with other NATO nations within Science and Technology Organization/Applied Vehicle Technoligy Panel(STO/AVT) were established with contributions from NLR (Nationaal Lucht- en Ruimevaartlaboratorium), NASA Langley Research Center and ONERA (Office National d'Etudes et de Recherches Aérospatiales). One of their main purposes is a better understanding of flow topology and aerodynamic performance of different aircrafts, particularly for medium to high Angle of Attack (AoA) and for asymmetric flow conditions. Incorrect predictions of certain flow structures could compromise the aircraft's safety and agility, especially for this range of AoA in low velocity flights.



FIGURE 1: From the project **F**uture **C**ombat **A**ir **S**ystem (FCAS). Courtesy of Airbus.

For flight conditions expected in a military aircraft, the most common configurations are slender or delta-wing type air vehicles for their well-known compact structure with gains in aerodynamic forces and control power. A recent design study by Airbus Defence and Space for a future European fighter is a good example of this kind of configurations as depicted in **Figure 1**. Despite advantages of these wing shapes, they also create challenging issues, such as the vortex dominated flow which develops at small to medium AoA. The vortex development, propagation, vortex-vortex interaction and vortex breakdown phenomena are some examples of challenging flow physics inherent to these configurations. Understanding of these flow phenomena allows for a more correct assessment of a fighter's performance and it can be analysed with experimental or computational studies. Advances in computational resources in the last decades allows for an easier computing of this complex flow. However only with well validated computational methods by experimental data and a proficient theoretical basis one can interpret these computational results correctly.

One of the NATO's STO/AVT Task Groups that dealt with these studies was the AVT-113 on "Understanding and Modeling Vortical Flows to Improve the Technology Readiness Level for Military Aircraft" to better interprete and model vortical flows in CFD for military aircraft (NATO Science and Technology Organization, 2009a). The AVT-113 was formed by two facets: Cranked Arrow Wing Aerodynamics Project International (CAWAPI) and Second International Vortex Flow Experiment (VFE-2). The CAWAPI facet worked on improving the CFD prediction, performing surface flow measurements on the F-16XL-1 aircraft for a variety of Mach numbers and AoA. The VFE-2 Group focused on the analysis of the wind-tunnel surface-pressure test results in order to have experimental data to validate the computational methods. For years the AVT-113 Task Group worked with participations from various NATO's nations researchers in a common effort to develop knowledge regarding the vortex flow. This Task Group increased the overall insight on vortex understanding, prediction and computation. One of its most interesting conclusions was that analysis of a vortex dominated flow in a transonic speed is the most complex to compute in CFD and to test in the wind tunnel.

Another important issue for the present application is the complexity of separated flow fields. The AVT-080 Task Group "Vortex Breakdowns over Slender Delta Wings"

(NATO Science and Technology Organization, 2009b) focused on collecting and assessing reliable experimental data to validate CFD methods in order to create a data base for future investigations on vortex breakdown phenomena, since it critically limits the control power of the aircraft. To complete this complex analysis, the Task Group had three different cores: analysing experimental data, analysing CFD performance and an analytical sub-group. There were two important factors characterizing the vortex breakdown phenomena: (1) location of the transition from laminar to turbulent flow and (2) location of the primary vortex. However, it remains unclear this flow separation physics and prediction.

Following AVT-113 and 080, the NATO research Task Group AVT-161 was established to extend and impro the knowledge in the computational ability to predict complex aerodynamics (Cummings and Schütte, 2010). The Task Group was separated into three subgroups: experimental data acquisition; CFD simulations and analysis of experimental and computational data. It versed over static and dynamic behaviour of vortex-dominated flows of delta wing type aircrafts, namely for typical UCAV (Unmanned Combat Areal Vehicle) and fighter type configurations like the X-31. The final work provided great insight in aerodynamics regarding the ability to predict complex flow fields.

In more recent studies, AVT-183 Task Group on "Reliable Prediction of Flow Separation Onset and Progression for Air and Sea Vehicles" (Hitzel, 2015) was created to improve CFD usage to predict the complexity involved in vortex-dominated flows. This Task Group mainly focused in the description of flow separation at highly swept round leading edge and its development along the wing, in an effort to complement information with latter AVT research groups. Even though simulations were performed on a diamond wing type aircraft with round leading edges, it provided great knowledge in vortex formation, vortex-vortex interaction and computational differences captured by the usage of different grids and turbulence models.

These Task Groups brought great advances in this field, but there were also several individuals who achieved interesting results with their investigations and tests. In 1979, the aeronautical engineer James Luckring conducted a series of experimental tests in a variety of swept delta-wings with different strakes coupled in the leading edge. In analysing lift, drag and pitching moment characteristics from a 44° swept wing [6], Luckring proved that strakes provide lift increments for high AoA but do not have much influence in low AoA. Polhamus analogy (Polhamus, 1969), still used today, accurately predicts the lift and drag-due-to-lift of slender, sharp-edge delta wings. This investigator also included non-delta wings, such as double delta, where the application of this analogy indicates that these platforms produce greater values for vortex lift than delta wings. Lamar (Lamar, 1980) extended the knowledge in Polhamus suction analogy and provided a strake wing design along with the procedure and data results proving the benefit of such structures in vortex stability. In 1983, Hoeikmakers et. al (Hoeijmakers, Vaatstra, and Verhaagen, 1983) proposed a new computational method to predict pressure and velocity distribution along a delta and a double-delta wing.

A computational model or method can only be validated through successful comparisons with experimental data. Hummel et al. (Hummel, John, and Staudacher, 1984) addressed a series of wing-body combinations to study unstable rolling moments and how to stabilize them. In this study, Hummel concludes that small modifications in the contour of the body will make favourable interference in vortex flow to stabilize the aircraft for the entire AoA range studied. The experimental study also performed by Hummel (Hummel, 1986) provided great insight in vortex formation, namely the interaction of vortex-vortex and wing-vortex. Although these are older data, they are still useful for recent comparisons and understanding of flow physics. Among others, the First International Vortex Flow Experiment (VFE-1) (Drougge, 1988) and the Task Groups mentioned

before, provide great knowledge with experimental data and computational techniques that allows until today to use these results for computational methods and models validation and development.

Nowadays, there is a continuous improvement in computational methods and experimental techniques are more accurate and sophisticated, allowing for a deeper understanding and better prediction of vortex dominated flow fields. However, there are still important gaps hindering a correct prediction of these complex phenomena. The main goal in the engineering community is to have computational resources that allow for creation of smarter designs and less wind tunnel testing.

## Motivation

In the $20^{th}$ century as well as in the past two decades, several engineers, investigators and investigation groups, have joined efforts to: (1) better understand flow physics around a delta or double-delta configuration and (2) validate computational models and methods. While the understanding of flow physics can lead to smarter designs and overcome challenges faced in the past for military aircraft, the improvement of computational aid is a powerful tool to reduce cost in production and wind tunnel testing. It is in this context that questions emerge on vortex-vortex interaction, vortex-wing interaction, vortex breakdown prediction and aircraft's safety and power control issues.

In this sense, the DLR established an internal project and is involved as well in a NATO STO/AVT Task Group to contribute for the growth in this complex subject. This thesis was done within the scope of this subject and additionally to be part of the preliminary investigation of this Task Group. Moreover, the opportunity of writing a thesis in DLR's Institute Aerodynamic and Flow Technology in partnership with FEUP comes with great professional and academic leverage. The possibility of participating in the scope of this field and adding knowledge towards future investigations has a boastfully personal and professional interest and accomplishment.

## Objectives

This investigation was designed to provide information on how grid refinement influences results obtained for the same configuration, test parameters and computational model. Moreover, it is also set to conduct a sensitivity study of turbulence models. These two studies are related to vortex location, pressure distribution and interaction. In addiction, a comparison with experimental data is provided for evaluation of best practice. Finally a brief discussion on flow physics and the aerodynamic performance is given.

Adding to these academical objectives, comes the main goal of providing more information to the aerodynamic science community in order to continue the work done in the last century.

## Approach

To accomplish these objectives, this thesis will begin by a theoretical explanation on vortical flow physics (Chapter 2), followed by description of model configuration used for all computational simulations (Chapter 3), of used turbulence models (Chapter 4) and of grid generation and its study ( Chapter 5). The experimental approach in the wind tunnel will be explained (Chapter 6) as well as it will be provided computational results for

the present investigation and its relation to flow physics (Chapter 7). Conclusions and recommendations for future work will be provided at Chapter 8.

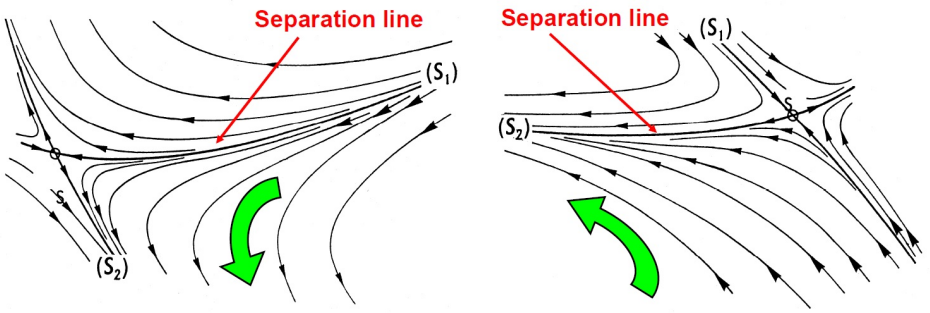
# Chapter 2

# Delta Wing Aerodynamics

Airflow can be characterized by its compressibility, steadiness and/or viscosity. Compressibility is a measurement of density variation with pressure and/or temperature modification; Steadiness is the evaluation of properties in time, e.g if they keep constant, then it is a steady flow; and viscosity is a measure of resistance of a fluid to deformation by shear stress. The concept of viscosity is important when describing the boundary layer of the flow. When inertial forces are greater than the viscous ones, the viscosity can be neglected and the Navier-Stokes equations result in the Euler equations. Since the boundary layer is turbulent, the complete Navier Stokes equations must be applied. The boundary layer concept is thoroughly explained in the book by Schlichting (1951) *"Boundary Layer Theory"* (Schilichting, 1951).

The high performance demand for an aircraft, namely a military aircraft, calls for an accurate prediction of the flow topology and this applies especially for the vortex dominated flow phenomena. Flow separates and rolls up to a vortex at low to moderate AoA and the vortex formation will take place at the leading-edge. With increasing AoA, they start interacting with one another forming a wider/stronger vortex, leading to its breakdown at some angle of incidence.

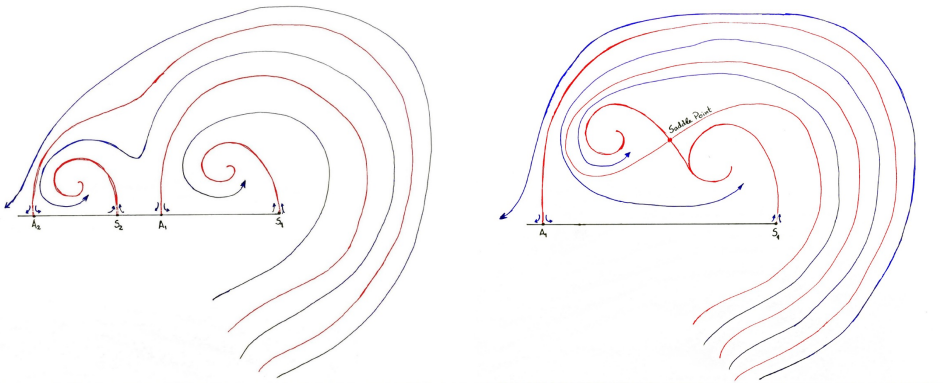
The viscous layer separates at the leading edge due to its sharp configuration and rolls upward and forward into a vortex sheet. This separation can be identified by plotting of skin friction lines, the trajectory lines of the skin friction vector field. The behaviour these lines have in the vicinity of a saddle point, indicates a separation or attachment line making up a barrier for streamlines coming from different nodes. Thus, depending on which type is present it can exist separation or attachment surface. **Figure 2** exemplifies this concept. While in Figure 2a the lines diverge from the ones who goes through the saddle point ($S_1$ and $S_2$), creating an attachment surface, in Figure 2b they converge to those lines, creating then a separation surface. This rapid convergence of the skin friction lines implies effective separation (Délery, 1992).




(a) (b)

FIGURE 2: Attachment (a) or separation (b) line schematic. Courtesy of ONERA.

When analysing a multiple delta wing aircraft there are several vortex structures occurring on the upper surface. In **Figure 3** there is a hand drawn sketch of how the topology can be described for two vortex cores side by side and a saddle point, or also called a double-branched vortex. Furthermore, the complexity is lightened in these figures, where the secondary vortex was left out of the sketch. In Figure 3a, the flow separates at $S_1$ and while some flow reattaches at $A_1$ and feeds the vortex, some flow will reattach and separate again at $S_2$ forming a more inboard vortex. At $A_2$ the flow mass will go either to the second vortex or continue in the fuselage direction. With increasing AoA, the lines $A_1$ and $S_2$ will merge and form a saddle point. This point, as seen in Figure 3b, is not attached to the surface and provokes a double-branched vortex formation. These sketches are a 2-dimensional view but when analysing a 3-dimensional flow the visualization is more complex.




(a) (b)

FIGURE 3: Two dimensional sketch of (a) two close together vortices and (b) a saddle point, where the lines represent flow mass.

The lift production in a delta wing type has the advantage of a non-linearity coming from the vortex formation above the wing at a relatively small AoA. Though linear lift contribution is smaller, due to a small aspect ratio, the AoA range is extended by this non-linearity. A gain in the AoA range gives a lead to the delta wing type comparing to a high aspect ratio swept wing in a commercial airplane. This is more explicit when analysing **Figure 4**, where the green line plots a typical curve for a delta wing, the red one belongs to a high aspect ratio swept wing. In Polhamus suction analogy (Polhamus, 1969), the suction that occurs at the leading edge will create a lift-due-vortex and for this reason delta wings have a lift coefficient ($C_L$) increase at AoA where conventional swept wings would be stalled.

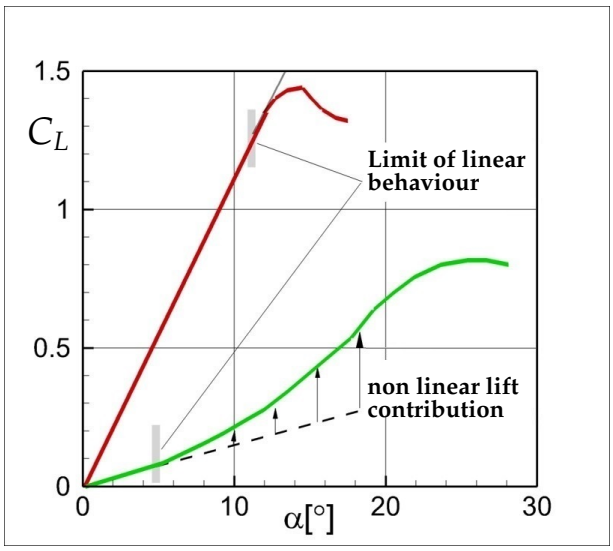



FIGURE 4: Lift coefficient and angle of attack plot comparing a regular swept wing (red) and a delta wing (green). Copyright Dr.-Ing. Andreas Schütte.

Since the last century, requirements for a military aircraft keeps accentuating and the highly swept/low aspect ratio wings in a triangular shape are the most common configuration - the *delta wing type* (Anderson Jr., 2007). The delta wing type has some variants such as the cropped delta or the double delta. Simple delta and its variants are the most used shapes for high-speed aircraft, and so their aerodynamic configuration is rather important. A schematic of the flow field over the top of a delta wing is shown in **Figure 5**. Although the aircraft is designed to perform high-speed manoeuvres most of the in-flight conditions are at a low speed, i.e. at subsonic speed. As seen in Figure 5, there are two vortices occurring at leading edge, that occurs even for very small AoA. These structures are formed by the difference in pressures between the bottom and top surface of the wing. The pressure below is higher so the flow will curl around the leading edge to overcome a natural imposition upon a sharp corner and it will separate.

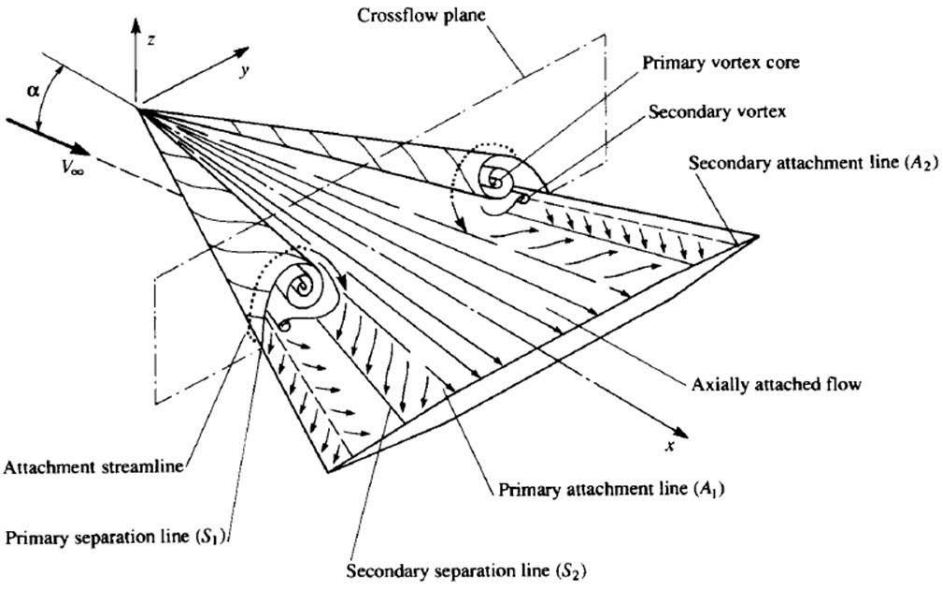



FIGURE 5: Flow topology scheme over a delta wing (Anderson Jr., 2007).

The primary vortex will come from the separation line, $S_1$, that exists at the leading edge and will reattach in $A_1$, the primary attachment line. The same happens with the secondary vortex with its own separation and attachment lines, $S_2$ and $A_2$, respectively. Both primary and secondary vortices stay contained in a loop by their separation and attachment lines. As said previously and showed in Figure 2, while the streamlines flow away from $A_1$ and $A_2$ they come towards $S_1$ and $S_2$. In Figure 5, it is also possible to see that the streamlines inboard the wing are almost unaffected by the vortical structures as they continue to be attached to the surface. In **Figure 6**, the pressure distribution is plotted with the sketch of the vortical structures on top.

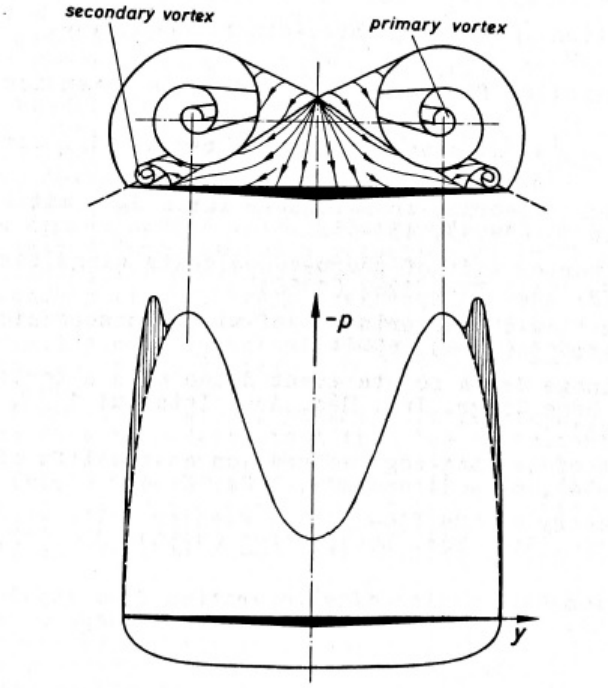



FIGURE 6: Vortex topology with the pressure distribution along the wing (Hummel, 1986).

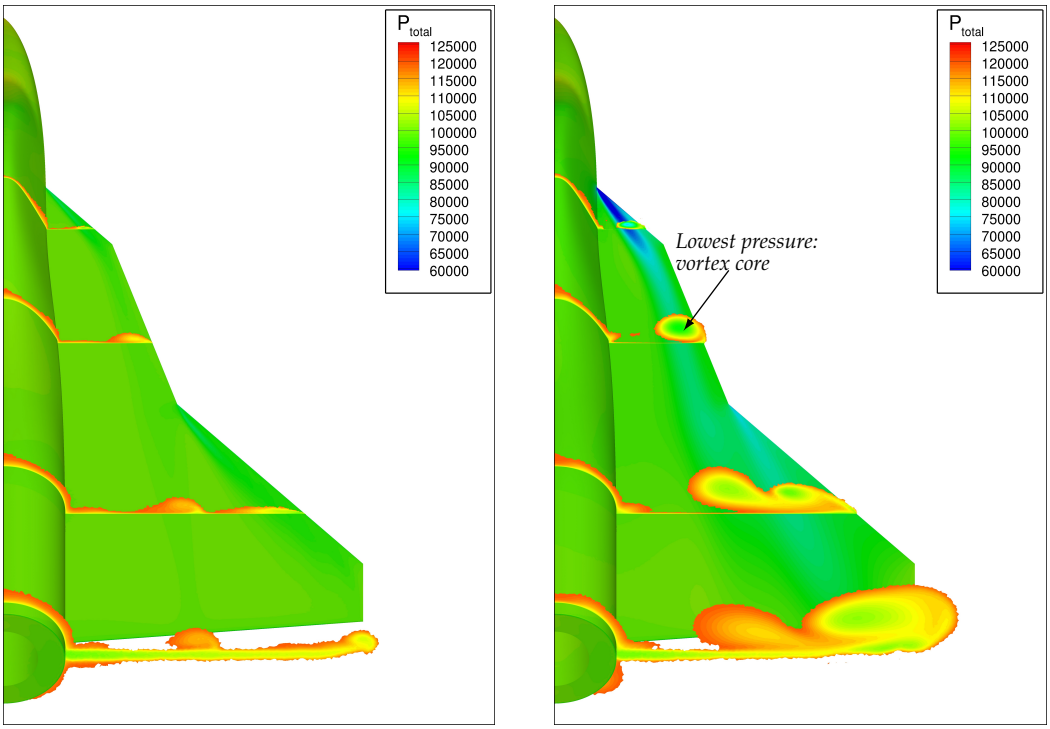
To interpret the vortex formation on the upper wing surface and its interaction with the aircraft and other vortices, one must begin by looking at surface pressure distribution. It visualizes how the pressure is distributed on the upper side surface wing and where low pressure occurs, locating the footprint of the corresponding vortex.

Evaluation of the pressure distribution is essential when describing the vortex topology on the upper side of the wing. The pressure is conveniently plotted with the negative value upwards. It is possible to interpret that both vortex cores it will have the lowest surface pressure and it gets higher as it goes inboard. At the lower surface the pressure keeps almost constant throughout the wing span and higher than at the upper surface. This pressure gradient at the leading edge creates a strong suction on that region providing the normal force distribution in the upward direction as well.

In the vortex core there is a region of continuously vorticity with a much higher velocity than in the freestream exist. With increasing AoA, this core gets wider and it is accompanied by flow fluctuations that leads to the phenomenon of *vortex breakdown.* The position along the wing depends on a combination of sweep angle and the incidence of

the wing (Hummel, 1986). Since the 50's this phenomenon has been subjected to studies by various researchers and engineers (Werlé, 1984). Lambourne and Bryer studies in (Lambourne and Bryer, 1961) separated the vortex breakdown into two types: (1) spiral type and (2) bubble type. The latter one is the most common to delta wings in compressible turbulent flow regions. Once the vortex has burst, the lift and the pitching moment will decrease and a stall situation will develop, as seen in Figure 4.

In the scope of this thesis, pressure distribution will be evaluated qualitatively, with a plot of surface pressure coefficient distribution, and quantitatively, with slices distributed along the wing. Furthermore, a field pressure distribution is evaluated with the plot of total pressure distribution. These plots can be all compared with streamlines distribution. These image comparisons and review allows for interpretation of the vortex interaction, at which location they start interacting and to determine the distance of vortex core to the surface. One example of total pressure distribution for the current configuration is displayed in **Figures 7a and 7b**.

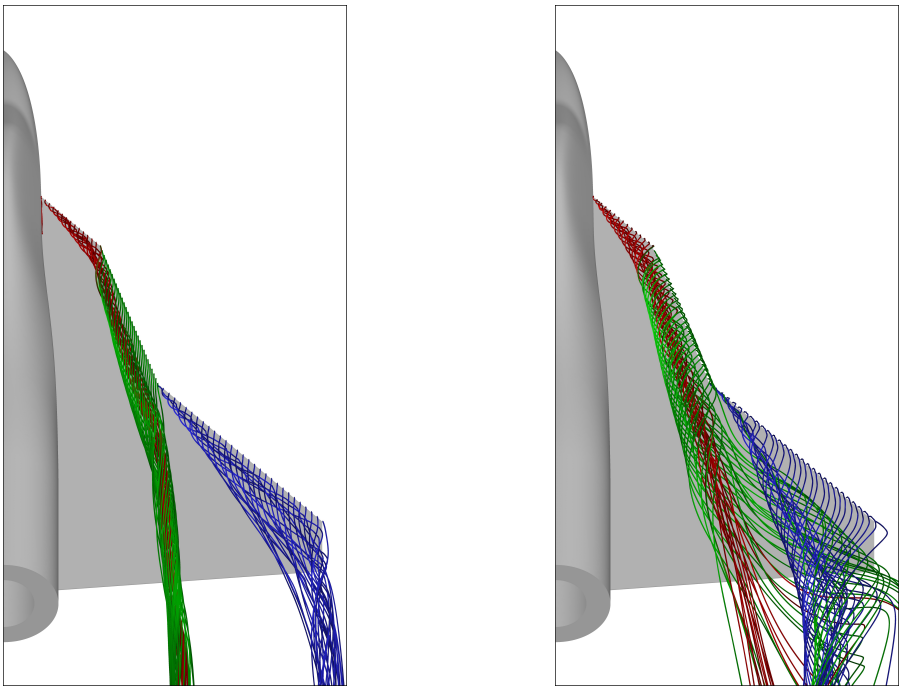



(a) (b)

FIGURE 7: Total pressure distribution in the upper surface for 2° (a) and 16° (b) angle of attack.

The general flow topology of a sharp leading edge delta wing remains even when considering a double or multiple delta wing planform. For these wing-type configurations, it is expected that for each delta, with a sharp leading edges, there will be separation and therefore a vortex formation. In comparison to single delta wings not only one pair vortices occur but multiple ones and they can interact with one another.

In **Figure 8a**, with the streamlines plot it is possible to ascertain this situation even for low angles of incidence. The Leading Edge Vortex CONtrol, or LEVCON, (red) and the Delta 1 (green) vortex are merged from small angles of incidence therfore is treated as a single vortex called Delta 1 vortex. At 16° angle of incidence in **Figure 8b** the Delta 1 and Delta 2 vortex are merged, forming a wider and stronger vortex.



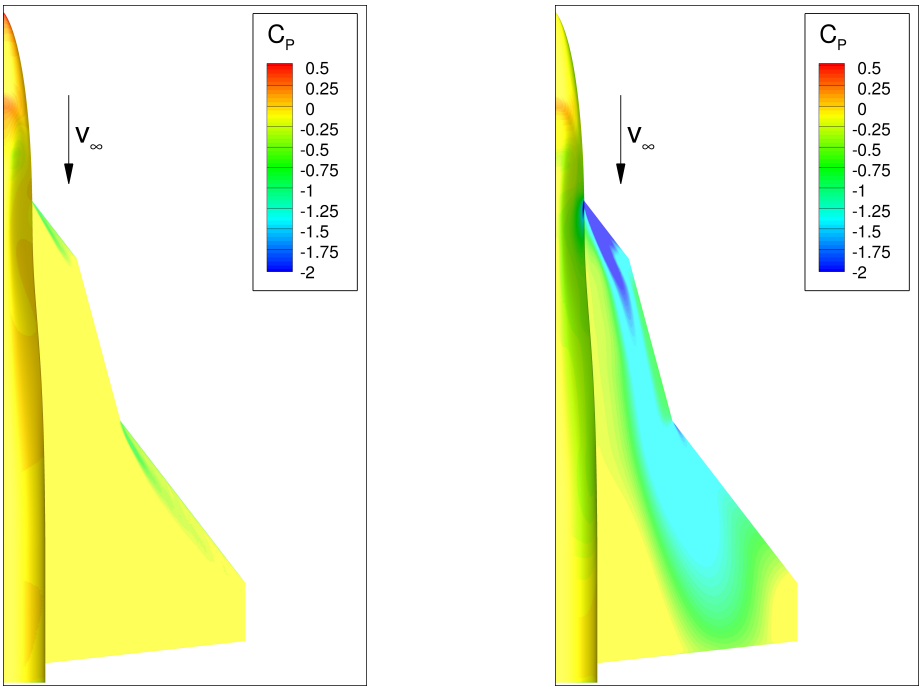
(a) (b)

FIGURE 8: Streamlines plot over a straked double delta for 2° (a) and 16° (b) angle of attack.

In **Figures 9** and **10** depict the surface pressure distribution and skin friction lines for a negative strake double delta configuration for an angle of attack of 2° and 16°. There is a clear distinction between these AoA. For 2°, in **Figures 9a and 10a** both vortices separating at the leading edge are weak and do not influence the pressure distribution all that much. This is relatable to Figures 8a and 7a where there is a small but distinct core for the strake vortex and Delta 2 vortex. When the AoA increases to 16°, in **Figures 9b and 10b**, the pressure coefficient is clearly much lower indicating a stronger vortex core with merging of the Delta 1 and Delta 2 vortices.

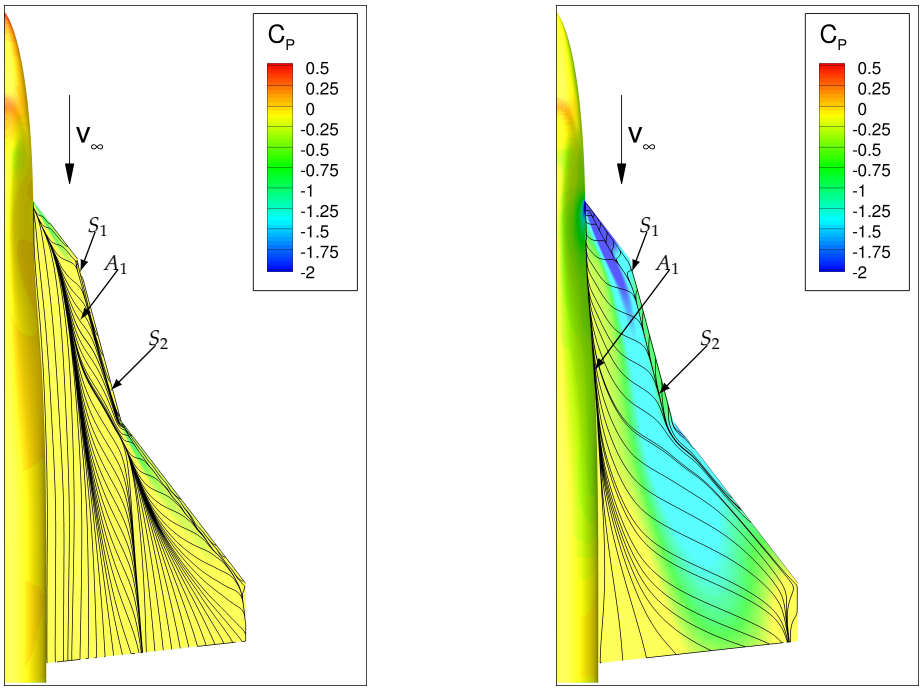
This latter merging is observed in the skin friction lines as well. The analysis of pressure distribution along with the skin friction lines, permits a understanding of flow topology, particularly identifying vortex interaction. As explained before, converging lines will tend to create a flow separation region, while diverging ones an attachment region. At the low angle of incidence it is noticeable two separation lines and two attachment lines, as depicted in Figure 10a. At 16° AoA, in Figure 10b, the separation continues at the sharp leading edge and the attachment region has shifted inboard.

When comparing to the streamlines, in Figure 8b, and the total pressure distribution, in Figure 7b, this merging is visible from 2/3 of the Delta 1 leading edge. With these four sets of Figures, 7, 8, 9 and 10, it is possible to describe the flow topology in the upper surface of this wing type. It is expected that, with the increase of the AoA, these merged vortices will get wider and it will burst, causing the same negative aspects as in a simple delta wing.




(a) (b)

FIGURE 9: Pressure distribution over a straked double delta for 2° (a) and 16° (b) angle of attack.




(a) (b)

FIGURE 10: Pressure distribution along with skin friction lines over a straked double delta for 2° (a) and 16° (b) angle of attack.

These Figures will be further discussed on chapter 7, along with the qualitative and quantitative comparison with the available experimental data.

# Chapter 3

# Model Configuration

A model of a generic fighter aircraft configuration has been established to perform the computational simulations throughout this investigation. The used configuration is enrolled within a current DLR project in cooperation with a NATO STO/AVT research Task Group aiming to evaluate the current CFD methods in predicting the vortex-vortex and vortex-wing interaction effects. The understanding of the vortex-vortex interaction should lead to improvements in the current design methods for a military aircraft, enabling a smarter design from an early stage with a main goal to improve the non-stop ageing aircraft fleet in the current market.

## Geometry

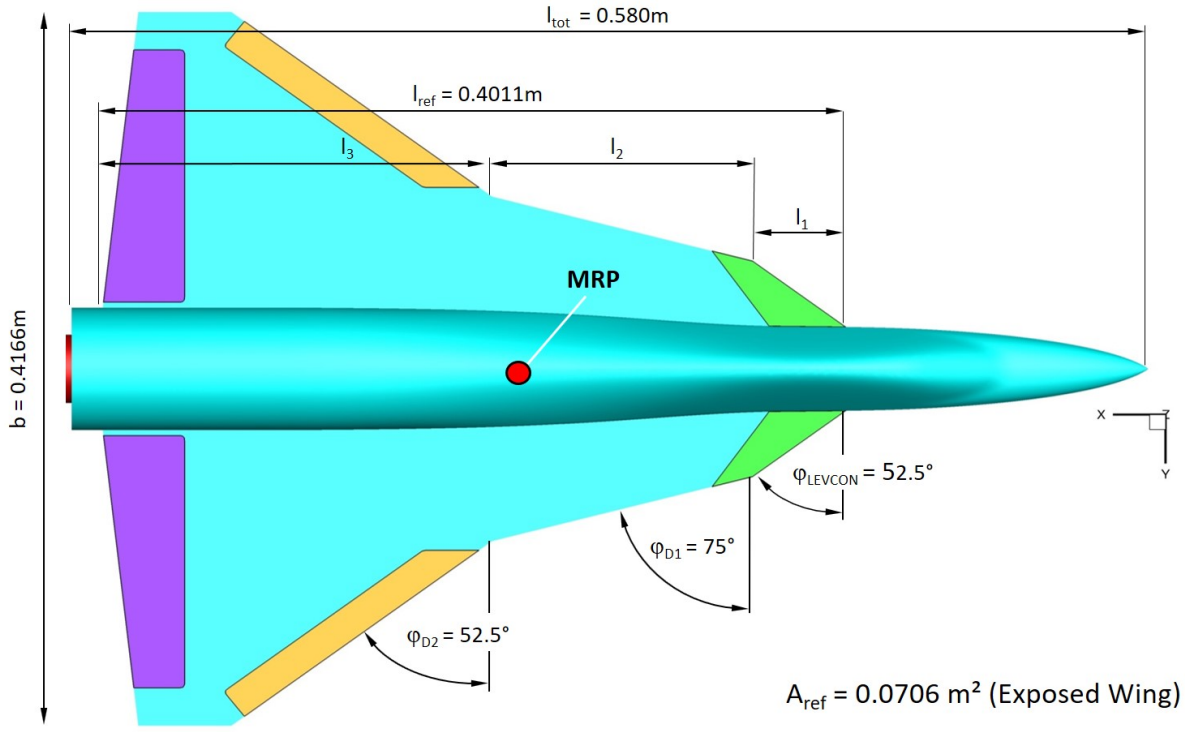



FIGURE 11: Model geometry without the representation of the sting and with reference lengths displayed.

The current model geometry is based on a generic double delta wing aircraft and a generic fuselage geometry negative strake, or LEVCON. For the wind tunnel testing a

rear support, called sting, is necessary, which was also included in the computational design. As seen in **Figure 11**, the wing is separated in three different lengths with different sweep angles. $l_1$ has 12.5% of the total length, $l_{tot}$, as for $l_2$ and $l_3$ both have 35%, resulting in a chord, $l_{ref}$, of $0.4011m$ . The exposed wing, also called reference area $A_{ref}$, of this configuration is of $0.0706m^2$, its model reference point (MRP) is located at $(0.4795m, 0m, 0.1m)$ and the wingspan, $b$, has $0.4166m$ of length. These reference values will be used later for the solver set up. The model is also designed with a sufficient leading edge (LE) thickness to perform the expected behaviour of a sharp LE.

In **Figures 11 and 12**, the coloured displayed areas in green, yellow and purple are the representing the negative strake, a slat and an aileron, respectively. Although the configuration was prepared to evaluate the effect of these three different vortex control devices, in the present thesis only the clean wing will be taken into account. For future applications of this model all of these control devices will be used in the simulation and experimental tests. In **Figure 13** the lateral perspective of the model is displayed.

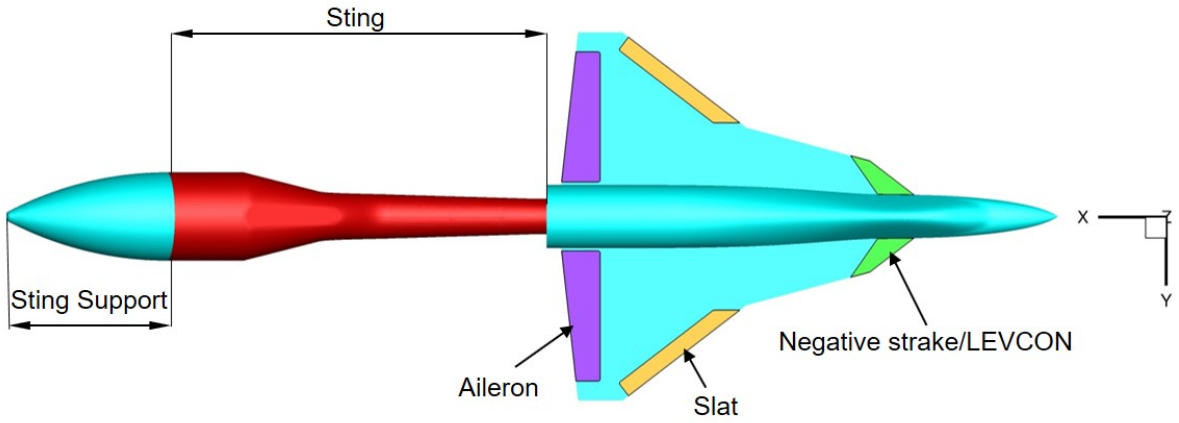



FIGURE 12: Entire model representation, namely the sting and the sting support.

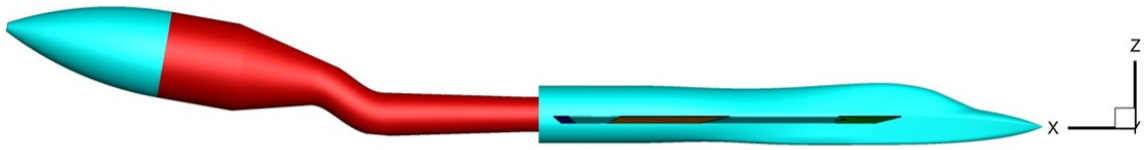



FIGURE 13: Entire model representation, in lateral view.

In Bertin and Cummings (2009) (Bertin and Cummings, 2009) there are four forces acting on an aircraft: lift, drag, weight and thrust. These forces determine the motion of an aircraft in a vehicle-fixed-coordinate system e.g. the air motions around the vehicle producing pressure and velocity variations in the flow field. Moreover, these forces produce: (1) a rolling moment resulting from differential lift (outcome of spoilers and/or ailerons); (2) a yawing moment in the vertical axis which points the direction of the aircraft; and (3) a pitching moment resulting from lift and drag. The moments are depicted in **Figure 14**.

The aerodynamic parameters that govern the forces and moments are, among others, the angle of attack ($\alpha$), the Reynolds number ($Re_\infty$) and the Mach number ($M_\infty$). The convention of forces and moments is very important for the data calculation and validation.

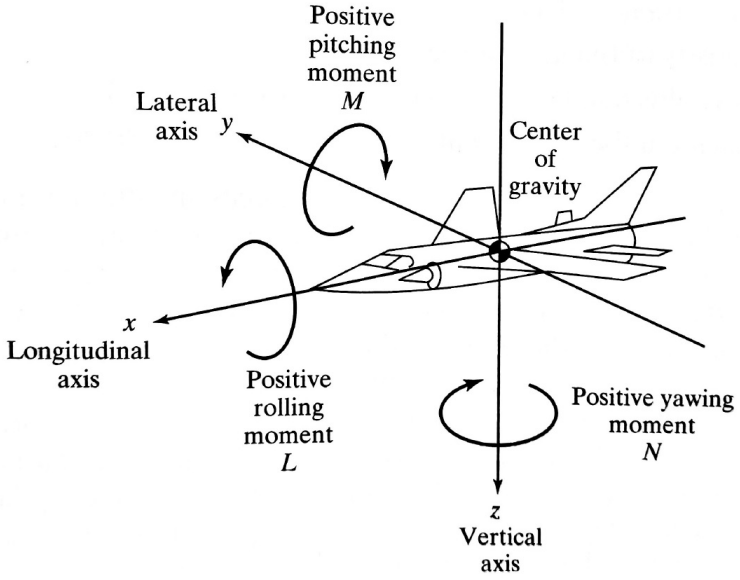



FIGURE 14: Convention of moments on a generic aircraft, by (Bertin and Cummings, 2009).

For the understanding of a vortex flow is necessary to interpret certain non-dimensional coefficients that result from forces and moments that have been mentioned. In this thesis, the following will be used:

- Pressure coefficient ($C_P$) - the local pressure ($p$) is measured relatively to the free-stream pressure ($p_\infty$). Used for plotting of pressure distribution and to compare with results of experimental data;
- Skin friction coefficient ($C_f$) - used to build skin friction velocity located at the viscous region of the turbulent boundary layer;
- Lift coefficient ($C_L$) - The lift in an aircraft will increase as AoA increases, until a certain maximum value where it starts to decrease and that point it's called stall. One aspect that can significantly change the lift-AoA relation is the leading edge radius, e.g. sharp leading edges have more abrupt stall;
- Drag coefficient ($C_D$) - The drag is the force that opposes the movement and is divided in four types: skin friction drag due to a viscous sub-layer near surface; pressure drag because of the pressure differences causing suction; vortex drag created by the wing vortex and wave drag caused in the event of a shock wave. One of the greatest challenges when designing an aircraft is the fact that as the lift increases, the drag will increase the square of the lift;
- Pitching moment coefficient ($C_m$) - The pitching moment is the moment around the y-axis and is the result of the lift and drag forces. It defines the direction of the nose of the aircraft, e.g. when this value is positive it indicates a nose-up direction;
- Rolling moment coefficient ($C_l$) - The rolling moment is defined by the differential lift forces caused by control systems, as a strake. This moment around the x axis is very sensitive and with great significance for the fighter's stability.

The latter four coefficients represent the aerodynamic coefficients of an airfoil, especially conceptualized to permit the comparison between different shape airfoils. The way they are defined allows for a direct comparison between their values and the AoA, Reynolds number and Mach number.

# Chapter 4

# Numerical Method

Computational fluid dynamics problems can be resolved by solving the Navier-Stokes, Euler or Bernoulli equations. The Euler equations are applied strictly to inviscid flows and the Bernoulli ones are a simplification of the Navier Stokes. For the interest of this thesis solving the Navier Stokes equations was chosen since its solves a time-depending variation of the viscosity and density.

The process of solving the instantaneous Navier-Stokes equations, requires solving the three-dimensional, time-dependent equations for all scales of motion, in time and space. This is computationally demanding and thus, non-feasible for engineering problems. As alternative, Reynolds proposed to separate the flow field in its mean and instantaneous components and solving the time-averaged Navier-Stokes equations.

For the process of Reynolds averaging, the flow is decomposed to an averaged and fluctuating component. When used in the Navier-Stokes equations, these become averaged as well, yielding an momentum description for the averaged motion. This is possible to be done when it is possible to assume a stationary turbulence. Furthermore, these equations are now called Reynolds Averaged Navier-Stokes (RANS). All these equations can be thoroughly consulted in several books about CFD, for example in Pozrikidis (1997) (Pozrikidis, 1997). While averaging the Navier-Stokes equations, fluctuating quantities called Reynolds stress terms occur. These terms provide more unknowns but not more equations, meaning that is necessary to provide equations to define these terms, a process that is usually called *closure*, and each turbulence method has its own closing method.

Discretization is a method of processing continuum problems into discrete elements. In the scope of this investigation, the Finite Volume Method (FVM) was chosen. FVM discretize the problem in finite control volumes to solve the second-order partial differential equations (PDEs). In comparison to other methods, the FVM is less likely to break down facing discontinuities (Leveque, 2004).

This chapter will include an explanation on the DLR RANS method TAU used in this dissertation and how it was applied. Furthermore, a brief theoretical explanation on the different turbulence models used will be given. Finally, the numerical approach will be shown.

## 4.1 DLR RANS Methods TAU

In order to analyse, predict and compute a fluid flow, DLR's Institute of Aerodynamics and Flow Technology developed a CFD method thoroughly described in (DLR Institute of Aerodynamics and Flow Technology, 2017a; DLR Institute of Aerodynamics and Flow Technology, 2017b). In the following it is briefly described how to use the solver TAU and how to correctly parametrize the problem to be solved. TAU is resolving the Reynols Averaged Navier Stokes (RANS) equations for compressible, three-dimensional, steady or unsteady flows using a finite volume formulation (Schütte, Hummel, and Hitzel, 2010).

The set-up starts with modifying a file which contains the parameters names, or keywords, and values. Each keyword is defined and explained in the documents provided by DLR, see (DLR Institute of Aerodynamics and Flow Technology, 2017a; DLR Institute of Aerodynamics and Flow Technology, 2017b). This file will define how the problem is solved, for example which turbulence model is used. Although for this study the default values for the preprocessor and solver modules parameters were used, they must be congruent with the ones found in the literature. These modules will determine the partitioning method used for the creation of dual-grids from the initial primary grid, the grid definition and re-definition to capture, respectively, flow phenomena and the basic parameters to solve the flow equations. Despite the fact that this file contains various keywords definitions, a list was made of the most important for this investigation:

- **Geometry data** - the solution will depend on these values, so it must be in agreement with the model configuration described in the previous chapter;
- **Reference data** - this has a reasonable impact factor since it must be coincident with the experimental data tests for an accurate comparison, e.g. the free stream Mach number, pressure, Reynolds numbers, among other quantities;
- **Inviscid flux discretization type** - between the options *Central* or *Upwind*, it will depend on 'where' the flux is going, e.g. the *Upwind* type considers that flow is going in only one direction, hence to solve supersonic flows, and the *Central* one considers all directions flow;
- **Central dissipation scheme** - when using the *Central* discretization type it is possible to use a *Scalar dissipation* or a *Matrix dissipation*, being the latter one more accurate and precise. For high AoA, it was a good practice to use *Scalar dissipation* in order to provide a starting solution followed by restarting it with *Matrix dissipation*;
- **Grid metric** - on the contrary of the cell-centred method, cell-vertex will group a number defined by the user into one single point. For the present simulations, the grid metric control grid factor is 5. So, as the grid resolution is defined by the number of points, the method must be clear, since in the cell-vertex method will have 5 times less points than the cell-centred one;
- **Multi-grid** - in this section the definition of start up steps can be defined, e.g. the steps done with the original grid before partitioning it to a dual-grid (multi-grid). The multi-grid allows an acceleration convergence process by clearing disturbances and damping in each step. DLR solver TAU will create a single finite volume from six cells;
- **CFL number** - the Courrant-Friedrichs-Levy number defines the stability and convergence of a FVM while the grid is redefined by the multi-grid process. This number defines the the velocity of each particle for each time-step, i.e. when it is inferior than 1 then each particle will move from one cell to another, while with values above 1 this same particle can be moving through two or more cells. For the time step size it is necessary to define the CFL number, in most cases a CFL number of 1 has been used but with the increasing the AoA this number was reduced to 0.8;
- **Turbulence** - as the name suggests, this section is dedicated to choosing a *turbulence model* and which *version*, see section 4.2;
- **Dual time stepping** - the user can choose between *steady* and *unsteady* calculations. When the *unsteady* calculation is chosen, a physical time step and its size have to be defined in a way to capture the vortex flow physics accurately.

## 4.2 Turbulence Models

A turbulence model is a CFD approach in order to solve a turbulent state of a flow. These models solve governing equations not for every scale of motion but for an averaged fluctuation. The equations to be solved depend on the model applied and they can be divided in three groups: direct numerical simulations (DNS), large-eddy simulations (LES) and Reynolds averaged Navier-Stokes (RANS). These equations can be consulted in several publications such as in the book by Bertin and Cummings (Bertin and Cummings, 2009).

DNS proposes to resolve all scales of turbulence, which implies a very fine three dimensional grid and very small time steps that result in great computational time. In strict sense DNS is not a turbulence model, rather the solving directly the Navier-Stokes equations for all scales of time and space. The LES approach will model the small scales in a sub-grid while the large scales are resolved. In comparison to DNS, the grid refinement and computational time needed are both reduced. On the other hand, RANS models all scales of turbulence using Reynolds averaged Navier Stokes equations. RANS turbulence model is supposedly the best option when the large eddy does have to be separately solved. Its computational costs can be lower than the other two because it always resolves the equations in an averaged way.

The Boussinesq hypothesis, developed in 1877, introduces the concept of eddy viscosity. Defining the momentum transfer caused by turbulent eddies was the first approach to resolve the closure problem. This problem is caused by the introduction of new variables when the averaging process is done. Boussinesq proposed the assumption that the Reynolds stress - a flow property - could be described as the viscous stress - a fluid property. The introduction of the turbulent viscosity property has many challenges regarding accuracy, as there limitations in its characterization due to lack of experimental data.

There were some attempts at solving the concept of the Reynolds tensor directly before Rotta in 1951 successfully achieved this. Modelling the whole Reynolds tensor ($\tau$) introduces six new equations to describe the Reynolds stress and one more to describe the turbulence length scale.

The RANS turbulence models can be divided into two model subgroups: the Reynolds stress transport models and eddy viscosity models. For the latter group, models are grouped by the number of partial differential equations (PDEs) that are solved. For this investigation, three models were used: a one-equation model, Spalart-Allmaras negative (SA-neg) and two two-equations models, k-$\omega$ and k-$\omega$-TNT and a six-equation model, Reynolds stress transport models or simply Reynolds stress models (RSM).

### Spalart-Allmaras

The first model version was introduced in 1992 by Spalart and Allmaras (Spalart and Allmaras, 1992) and it is usually referred as Spalart-Allmaras turbulence model or in short SA. Since then some proposals for modifications where made, one in particular in 2012 where the problem of under-resolved grids and unphysical transient states were addressed and it was called SA-negative (Spalart, Allmaras, and Johnson, 2012). From the authors themselves this modification will "be passive to the original (SA) model in well-resolved flow fields and should produce negligible differences in most cases", so the problem was solved and it doesn't influence the rest of applications.

The SA turbulence model is a local model, for the solution in one point does not depend on the solution of other points. Its most noticeable advantages include: single transport equation, local formulation, moderate grid resolution requirements, good numerical stability and insensitivity to the freestream value. It is a very common model for computational usage since its application requires less grid refinement and it is solving

just one equation. Some downsides accompany these advantages, such as its weakness regarding massive separation, wakes in pressure gradient, free vortices and unsteady flows.

In TAU, different versions of the Spalart-Allmaras model are implemented. The one used throughout this research was the SA-negative. Although there are some difficulties regarding the accuracy, the model is well validated for highly swept wings with round leading edges. Furthermore, is able to predict the separation on set point at the leading edge quite sufficiently (Schuette, Hummel, and Hitzel, 2010), being fit for a starting point and reference in comparison to the other following approaches.

### k-$\omega$ and k-$\omega$-TNT

This two-equation turbulence model was first created by Kolmogorov (1942) and later developed by Saffman (1970) and since 1972 that Wilcox has been continually studying and improving the k-$\omega$ turbulence model (Wilcox, 2008). This model comes as an attempt to improve the k-$\epsilon$ model, a widely used two-equations model that struggles in solving flows with adverse pressure gradients or with strong separation. While k-$\epsilon$ solves $\epsilon$, the dissipation rate of k (the turbulent kinetic energy), k-$\omega$ solves $\omega$, the specific dissipation rate of k. The k equation, modified in comparison with k-$\epsilon$, and the transport equation for $\omega$ are solved to give the solution for the flow field in study. Although k-$\omega$ does not require computation of the wall distance and is less stiff in the near-wall region, the solution strongly depends on $\omega$ values in free-stream and this dependence is significant for the results in the boundary layer.

One solution for this dependence was presented by Menter in 1993 is the usage of k-$\omega$ formulation for the viscous sub-layer and the k-$\epsilon$ for the free stream field, hence using the best of the two models for each section of the flow field.

Another derivative is the turbulent/non-turbulent (TNT) k-$\omega$ model, developed by NLR. With the modification of diffusion coefficients it was possible to decrease the Wilcox's k-$\omega$ dependence on the free-stream values (Kok, 2000).

The DLR solver TAU is providing various two-equations models including all mentioned above. For the present report, the k-$\omega$ in the version from Wilcox and the k-$\omega$ TNT were used. These two models present a downside on assuming that the turbulent viscosity is isotropic while in this complex type of flows anisotropic effects are present. But as it is solving two PDEs is assumed that the benefits of low computational cost will be considerable in comparison to its accuracy.

### Reynolds Stress Model

The RSM closes the Reynolds-averaged Navier-Stokes equations by solving each transport equation from the Reynolds stress tensor plus an equation to solve the turbulence dissipation (Cummings et al., 2015).

The first proposal for this second-moment closure model was made by Rotta in 1951 and in the 1970's it was applied to some flows. Its usage for more complex turbulent flows as involving separation or complex geometries started in the beginning of the 1990's with the increase of computational capability (Thakur and Shyy, 1999). The manner that a RSM deals with the pressure diffusion terms, the pressure-strain rate and the dissipation rate depends on which version of RSM is in use. The model used in this investigation deals with the scalar rate of dissipation of the turbulent kinetic energy, also known as $\epsilon$ equation. Based on the work of Menter in 1994, it was possible to adapt one constant and the expression for turbulent eddy viscosity in order to resolve the length scale required by DLR solver TAU.

Although it is the most computationally expensive it is also the most physically complete turbulence model, i.e. it is the one that is expected to have the highest accuracy predicting the vortical flow in the present work.

## 4.3 Numerical Approach

The $C^2A^2S^2E^2$ high performance computing cluster has been used for all performed simulations. Each node has two processors, each with four cores, with a memory capacity of 16Gb. Three sets of computational simulations have been conducted: a grid sensitivity study, a turbulence model sensitivity study and a validation study by using experimental data. In the presented tables, the test matrix is given with the performed calculations and different test parameters used. For simulations performed in the grid sensitivity study, in **Table 1**, a half model was used in order to reduce computational time. For the turbulence model sensitivity study, in **Table 2**, the four aforementioned models are compared for a symmetric on flow conditions (i.e. $\beta = 0°$). Both studies were performed for an initial AoA of $\alpha = 2°$ and with an increment of $\triangle\alpha = 2°$ up to $\alpha = 10°$, with the exception of the k-$\omega$ where the maximum AoA is $\alpha = 8°$.

The validation study using the experimental data was done using all the turbulent models previously mentioned. These simulations had the Reynolds number changed from $4.5 \cdot 10^6$ to $3.6 \cdot 10^6$ in order to be coincident with the wind tunnel conditions, since these tests were performed after simulations began. In **Table 3**, it is exposed the test matrix to evaluate the effect that different Reynolds numbers can have in the solution.

Finally, in **Table 4**, it is the comparison with the experimental data. In this study, as well as in for the Reynolds effects study, it was possible to include an asymmetric on flow conditions with a side slip angle of $\beta = 5°$ study.

| Grid | $\alpha[°]$ | $\triangle\alpha[°]$ | $\beta[°]$ | Re [-] | Turbulence Model |
|---|---|---|---|---|---|
| coarse | 2 - 10 | 2 | 0 | $4.6 \cdot 10^6$ | SA-neg |
| medium | | | | | |
| fine | | | | | |

TABLE 1: Grid sensitivity study.

| Grid | $\alpha[°]$ | $\triangle\alpha[°]$ | $\beta[°]$ | Re [-] | Turbulence Model |
|---|---|---|---|---|---|
| medium | 2 - 10 | 2 | 0 | $4.6 \cdot 10^6$ | SA-neg |
| | | | | | k-$\omega$ |
| | | | | | k-$\omega$-TNT |
| | | | | | RSM |

TABLE 2: Turbulence model sensitivity study.

| Grid | $\alpha[^\circ]$ | $\triangle\alpha[^\circ]$ | $\beta[^\circ]$ | Re [-] | Turbulence Model |
|---|---|---|---|---|---|
| medium | 2 - 10 | 2 | 0 | $4.6 \cdot 10^6$ | SA-neg |
| | | | | $3.5 \cdot 10^6$ | |
| | | | 5 | $4.6 \cdot 10^6$ | |
| | | | | $3.5 \cdot 10^6$ | |

TABLE 3: Reynolds effects study.

| Grid | $\alpha[^\circ]$ | $\triangle\alpha[^\circ]$ | $\beta[^\circ]$ | Re [-] | Turbulence Model |
|---|---|---|---|---|---|
| medium | 10 - 21 | 1 | 0 | $3.5 \cdot 10^6$ | SA-neg |
| | 10, 12 | | | | k-$\omega$ |
| | 10 | | | | k-$\omega$-TNT |
| | 10, 12, 16 | | | | RSM |
| medium | 12, 16 | | 5 | $3.5 \cdot 10^6$ | SA-neg |
| | | | | | RSM |

TABLE 4: Experimental comparison study.

The monitoring of each simulation was done using the post-processing software *Tec-Plot*. The values for lift, drag, pitching moment and angle of attack were monitored and as soon as the convergence was achieved, the next AoA has been simulated. **Figures 15 and 16** are two examples of the aspect of a convergence history, for a steady and unsteady simulation respectively.

For the present calculations, the density residual ($\rho_{residual}$) has only between 2 and 3 magnitudes but nevertheless the coefficients present a stable behaviour. In Figure 15, the steady convergence for the SA-neg simulation is plotted. The region in A shows the influence of the dual stepping in the density residual. The B region indicates where the steady state cannot further calculate the flow coefficients. Upon the latter situation, the simulation has been changed to unsteady simulation as depicted in Figure 16.

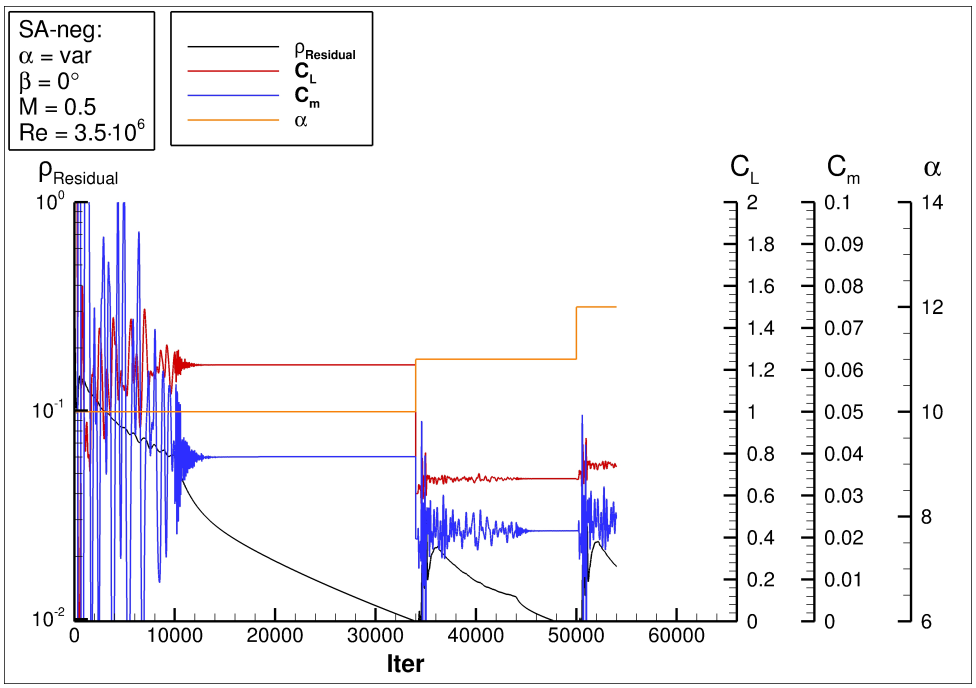



FIGURE 15: Convergence history of an steady simulation.

The monitoring of an unsteady simulation has to be separated in inner (top convergence history) and outer (bottom convergence history) convergence. The aspect is very similar but values in the x-coordinate represent the number of iterations for the inner convergence and time in seconds for the outer one. While inner iterations monitor iterations for each time step, the outer iterations is the convergence of several time steps each simulation has. For each AoA calculation, the outer iterations values had to be stable between 2 and 3 seconds until the next AoA could be calculated.

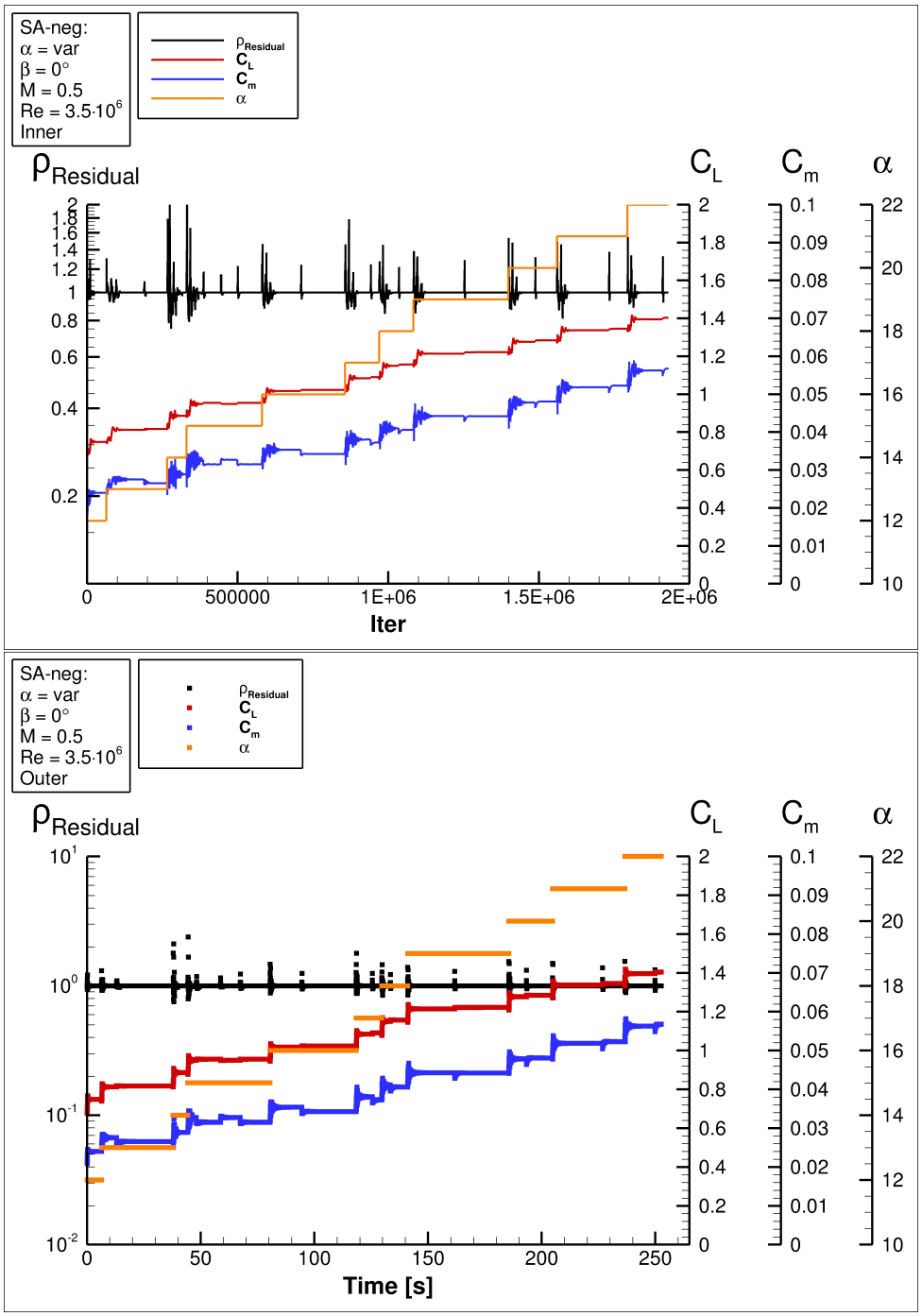



FIGURE 16: Convergence history of an unsteady simulation.

# Chapter 5

# Grid Generation

For the numerical method approach, it is necessary to have a grid to serve as a basis for solving the Partial Differential Equations (PDEs). The grid generation process can be settled with three steps, the surface definition already described in Chapter 3, the surface grid generation and the field grid generation. Each step has its challenges but over the years the improvement in technology and software allows for users to create an adequate mesh for the model/problem with advanced grid generation methods. The grid itself can be classified in three types: structured, unstructured or hybrid, each with its advantages and drawbacks.

Structured grids are defined by a regular pattern and connectivity between points, e.g the location of each cell can be related to the ones in its vicinity. Although this approach is very useful for simple geometries, its simple layout can lead to singularities and inefficiency, as it is more time consuming to create the mesh with more complex geometries when compared to other methods. For complex geometries, the unstructured method was developed by using irregular patterns of tetrahedrons, prisms or other cell types that allow an easier and faster grid generation. With this method, other problems aroused such as the production of skewed cells in the viscous layer and its challenging implementation when using some turbulence models (Cummings et al., 2015).

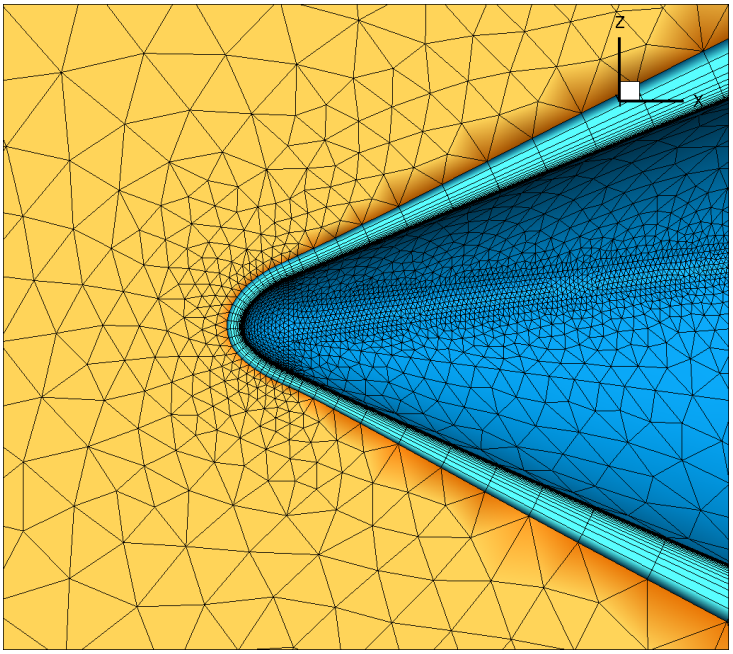



FIGURE 17: Nose fuselage detail of the medium refined grid.

In a CFD analysis of vortical flows, it is important to correctly compute the small scale eddies that occur close to the surface, whereas the viscous layer must have an adequate

grid resolution to capture the phenomena of interest. Hence it is a common practice to implement a hybrid method, where the grid has both structured and unstructured regions. In this case, the viscous layer or boundary layer mesh is created using a semi-structured method and the flow field with the unstructured method. **Figure 17** describes a hybrid topology in general: the dark blue is the surface region with a surface triangular grid, in the light blue area, the boundary layer area, the mesh is structured and the orange region, the far field surrounding the model, the mesh becomes unstructured by applying tetrahedral cells.

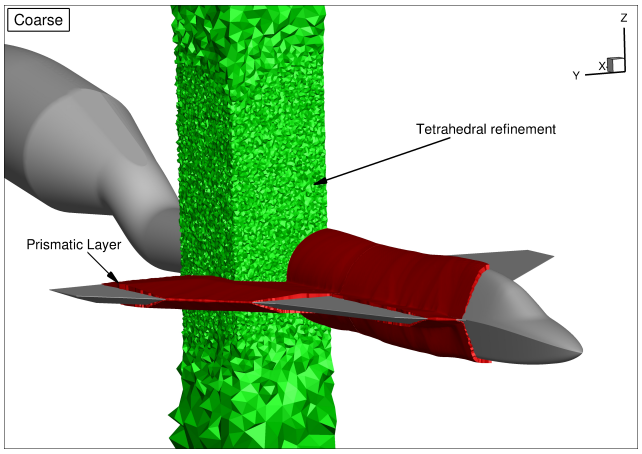
In this chapter, the generated grids are displayed and a brief discussion on how the evaluation is made as well as a comparison of different grid sizes. As the focus is to improve the prismatic layer, resolving the boundary layer flow, the values influencing surface and tetrahedral layer were not changed. The most visible changes occurred when the CAD Source is modified. This allows for different curves, panels and so forth to be grouped together and to apply same length scales and same parameter changes to all entities. In the different grid quality studies, three source values were modified: the LE cockpit, the Trailing Edge (TE)/LE and the geometry source length values (CENTAUR, 2018). **Table 5** provides the parameters modified and the number of points for each grid, including values for the full model grid using the medium refinement parameters. The strategy was based on the best compromise between coarse and fine grids, in order to diminish the total number of elements without losing much accuracy.

| | Course | Medium | Fine | Full model |
|---|---|---|---|---|
| Prismatic layer stretching ratio | 1.35 | 1.3 | 1.3 | 1.3 |
| LE Cockpit length scale | 0.03 | 0.03 | 0.02 | 0.03 |
| TE/LE length scale | 0.1 | 0.15 | 0.05 | 0.15 |
| Geometry source length scale | 2 | 1.5 | 1 | 1.5 |
| Number of elements | $41.6 \cdot 10^6$ | $68.2 \cdot 10^6$ | $203.9 \cdot 10^6$ | $136.5 \cdot 10^6$ |
| Number of points | $11.6 \cdot 10^6$ | $15.9 \cdot 10^6$ | $44.9 \cdot 10^6$ | $31.9 \cdot 10^6$ |

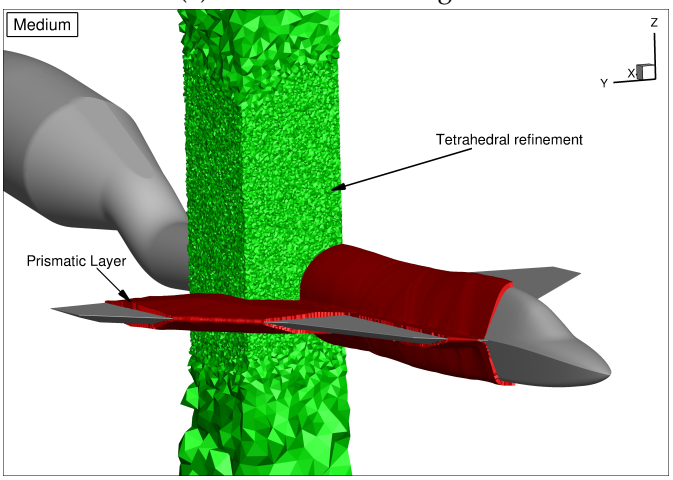
TABLE 5: Parameters changed during the grid sensitivity study.

The number of points is relevant since the cell-vortex method has been used in all simulations. This method allows for calculation at the vertex of a group of cells. This is important when calculating next to the surface. The integration point in the cell-centred method is in the centre of each cell therefore a lot of surface information can be lost. On the other hand, the cell-vertex method will have integration points at the surface since there are vertexes there. Being a more accurate method in calculations next to physical walls and the phenomena in interest, this is the method that has been used in all grids.

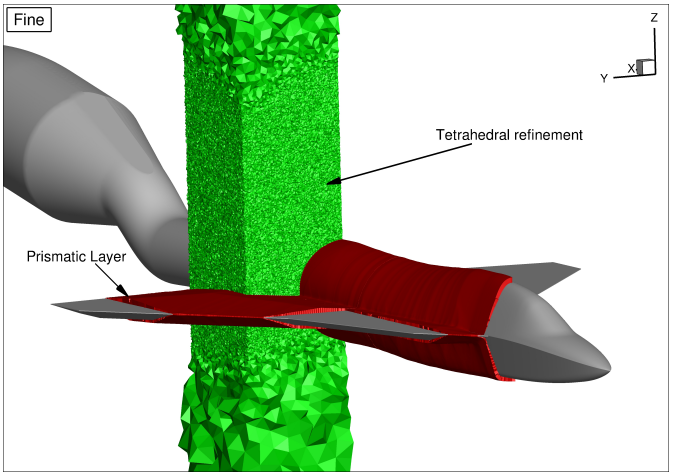
For the present thesis, three different grids were studied using the grid generation software CENTAUR$^{TM}$ (CENTAUR, 2018). The grids are defined by its resolution, i.e. the grids are called *coarse*, *medium* and *fine*. **Figure 18** shows a comparison between grids. It is depicted the prismatic layer in red and the tetrahedral layer in green.




(a) Coarse refinement grid.




(b) Medium refinement grid.




(c) Fine refinement grid.

FIGURE 18: Three dimensional view of the whole model with the three generated grids.

To analyse differences between grids in detail, in **Figure 19** a slice $y = const$ at the wing is depicted and in **Figure 20** the detail of surface grid at the LE. In Figure 18 the difference in the red layer between grids is clear, while the surface detail depicted in Figure 20 shows the difference to obtain different layer heights.

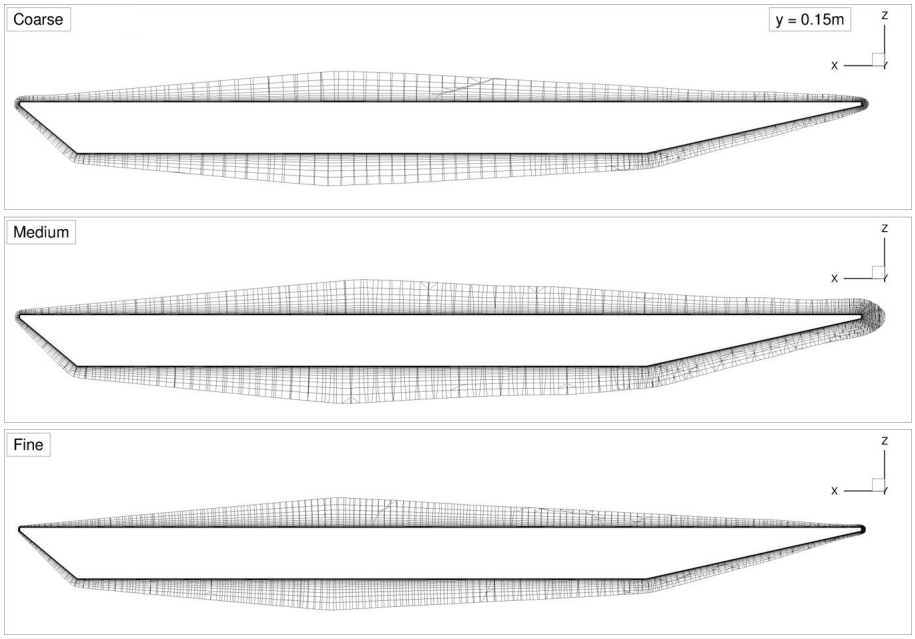



FIGURE 19: $y = const$ at $y = 0.15m$ from the nose figure for prismatic layer visualization.

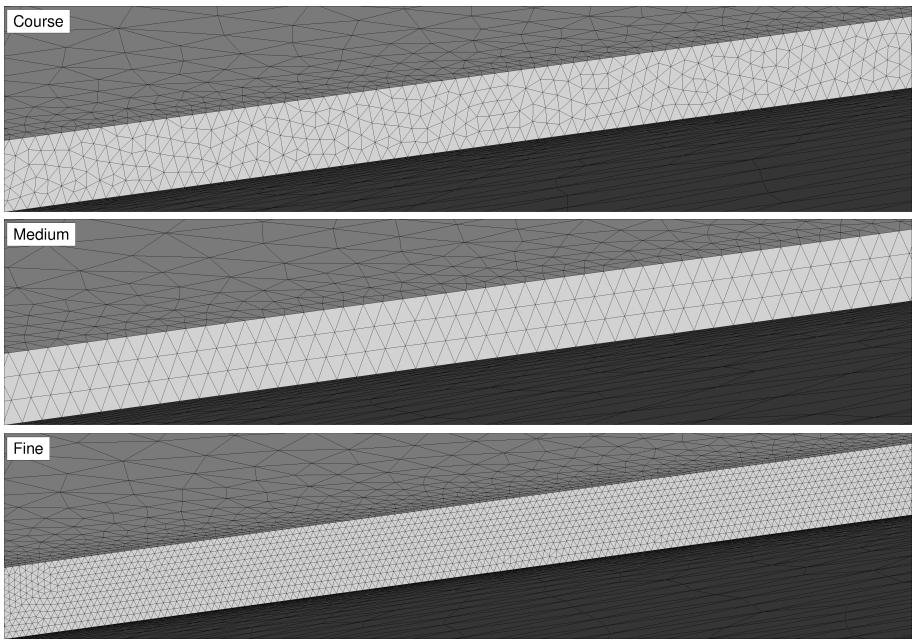



FIGURE 20: Leading edge number of surface elements comparison between grids.

### Boundary layer resolution

To be sure that the entire boundary layer flow is captured by the prismatic layer a plot of the velocity profile is given in order to confirm if the grid was correctly generated. The velocity at wall is zero and increases until it reaches the freestream velocity ($V_\infty$), so the prismatic layer has to end after reaching the maximum velocity. In **Figure 21** the velocity profile is illustrated together with the mesh to evaluate if the prismatic layer is sufficiently thick.

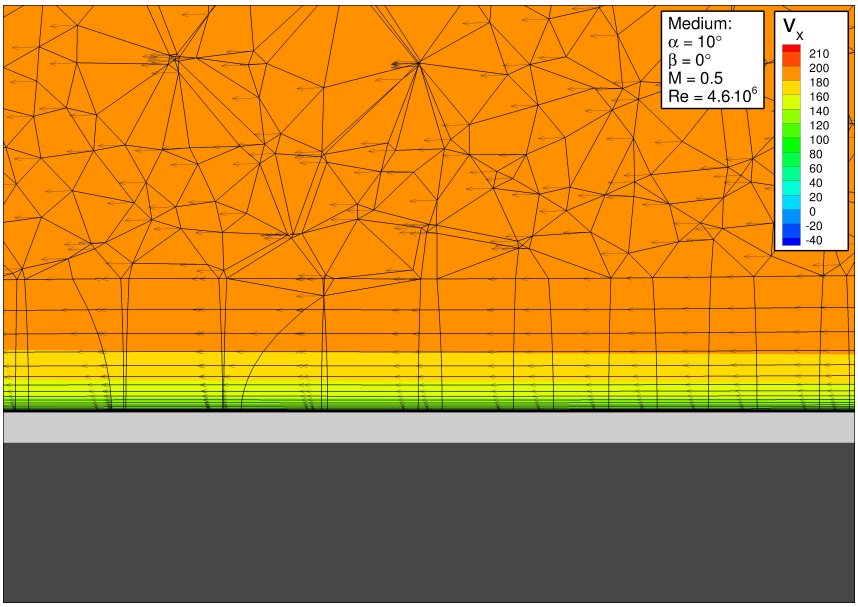



FIGURE 21: Velocity vectors profile for medium refined grid.

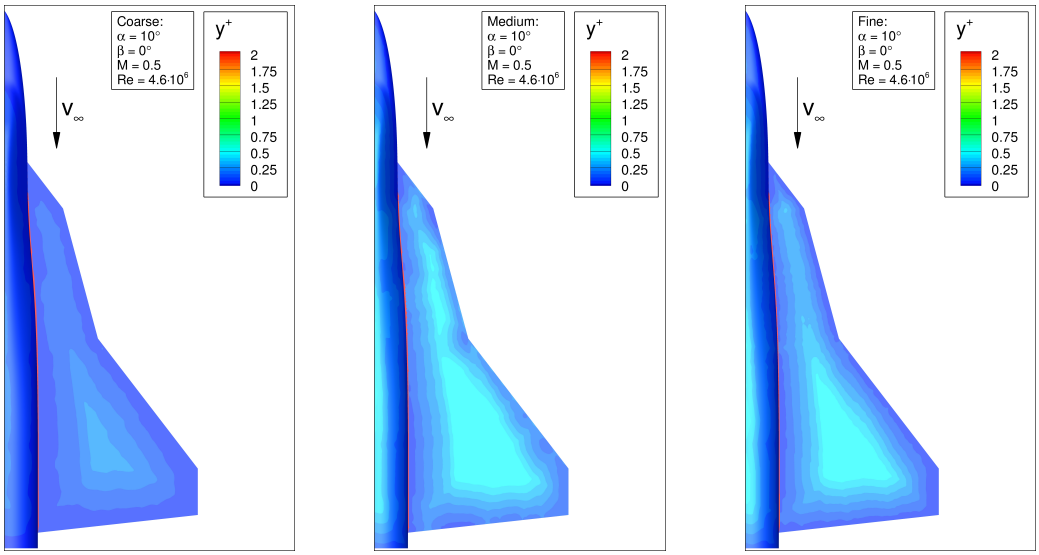
While analysing this last Figure, it is to notice that the prismatic layer is sufficiently high to include all velocities range. Nevertheless, the velocity profile differs from one grid to another. As the number of cells increases from coarse to fine, different disturbances in the flow are captured.

### $y^+$ - Dimensionless wall distance

The prismatic layer has to have enough thickness to include the dimensionless wall distance, $y^+$, a wall function dependent value that is used in different turbulence models. Theodore von Kàrmàn (1930) stated that the mean velocity within a turbulent boundary layer is proportional to the logarithm of the distance from the wall. In the wall vicinity, the flow undergoes abrupt changes and, seen as pressure gradients are normal to the wall, the grid layer must be the finest in the normal direction.

The $y^+$ and the dimensionless velocity, $u^+$, are used to calculate the shear stress equations at wall nodes, so the prediction of $y^+$ has to be accurate for the construction of the prismatic layer accordingly. Although the exact value is only known after the simulation, a prediction has been done using the flat-plate theory with the Reynolds number used in the simulation.

In **Figure 22**, the three $y^+$ surface distribution are presented. Literature indicates that to accurately model the influence of the Reynolds stress tensor, the value of $y^+$, i.e. the thickness of the first cell, must be less than 1. In all grids it has been confirmed that this dimensionless wall distance maintains less than 1.




(a) (b) (c)

FIGURE 22: $y^+$ distribution for each generated grid

# Chapter 6

# Experimental Case Study

This chapter will describe the experimental approach performed with the model designed by Airbus Defence and Space and tested in cooperation with DLR. It is a model made of steel with an internal strain gauge, shown along with the sting and the sting support in **Figure 23**.

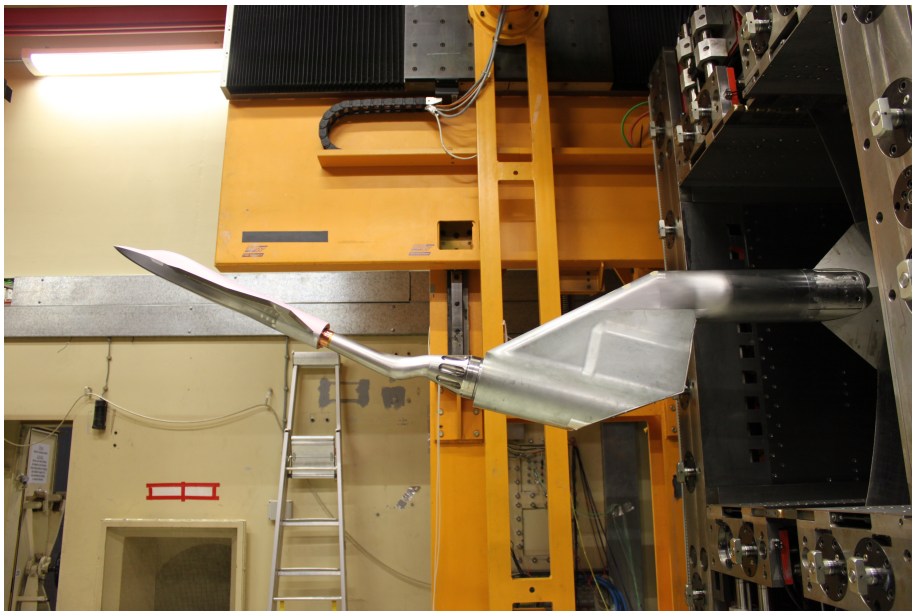


FIGURE 23: Photography of the entire model, the straked double delta with the sting and sting support. Courtesy of DLR/DNW-TWG.

The model, was tested in DNW (German-Dutch Wind Tunnel) Transonic Wind Tunnel in Göttingen, also called DNW-TWG. The TWG, depicted in **Figure 24** is a Göttingentype close-loop wind tunnel with a closed test section. The TWG can operate at Mach numbers in the range between 0.3-2.2 depending on the configuration chosen, e.g. when performing tests with adaptive walls the maximum limit is 0.9. The wind tunnel boundary conditions have been a Mach number $M_\infty = 0.5$ and a Reynolds number $Re_\infty = 3.5 \cdot 10^6$, related to the wing reference length of $l_{ref} = 0.4011m$. The tests have been performed for an AoA range of $\alpha = 10°$ to $\alpha = 40°$ at symmetric and from $\alpha = 12°$ to $\alpha = 40°$ for asymmetric on flow conditions.

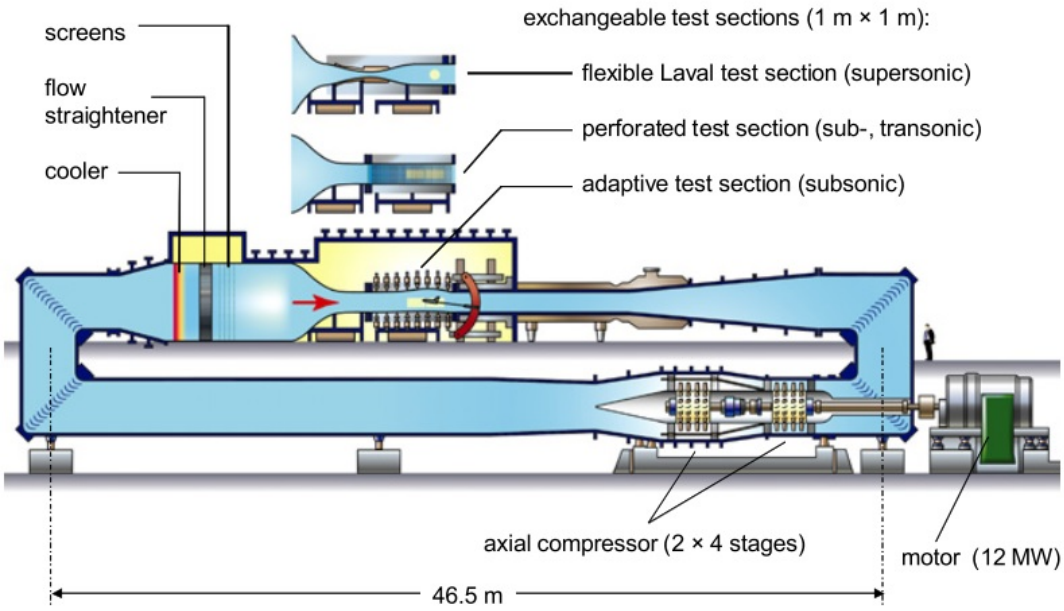



FIGURE 24: TWG model. Courtesy of DLR/DNW-TWG.

*Pressure-Sensitive Paint (PSP)* was used to measure pressure on the surface of the aircraft model. The PSP method is an optical pressure measurement technique. This method quantitatively measures pressure distribution on the model surface without the use of probes and without affecting the surface. In recent years, DLR has employed efforts in improving the method for the usage of PSP - the lifetime-based method (Yorita, Henne, and Klein, 2017). This method has the variant called *two-gate method* based on excitation of molecules via a light source and a fast-shutter camera to capture the luminescence decay. The two images captured by this camera will not have problems with model deformation or displacement. With optimization of several factors, namely the camera's system, LED settings and the paint's quality, DLR is further improving this method to implement it in broader wind tunnel tests since the vast majority that use this PSP technique are performed in low-speed models (Klein et al., 2005).

Regarding the wind tunnel tests, it is necessary to add reference points and a tripping system in the model, as well as to include some reference pressure tubes measurement in the wind tunnel section area. The tripping is the result of the dots on the nose as seen in **Figure 25** and it ensures a fully turbulent flow conditions on the fuselage as assumed in the CFD simulations.



FIGURE 25: Photography of the model close-up to see the tripping system on the nose. Courtesy of DLR/DNW-TWG.

One must stress that the great advantage of this technique is the possibility of obtaining the entire surface pressure distribution and with high spacial resolution. These preliminary results will be calibrated to the temperature distribution and absolute pressure (Klein et al., 2005). In **Figure 26** an example of the final data of a pressure distribution is plotted. The wind tunnel testing also provides the forces and moments acting on the model. These three data sets will be compared in chapter 7 with the computational results in the simulations performed throughout this investigation.

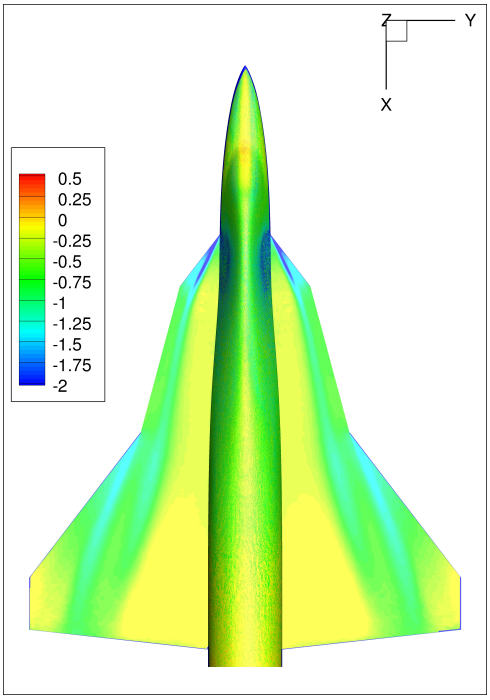



FIGURE 26: Representation of the pressure distribution on the upper surface of the model using PSP technique.

The experimental data was obtained performing wind tunnel tests during the firsts months of 2018 and are published in an internal DLR report by Rein et al. in "Transonic

Wind Tunnel Measurements of Double and Triple Delta-Wing Configurations" (Rein et al., 2018).

# Chapter 7

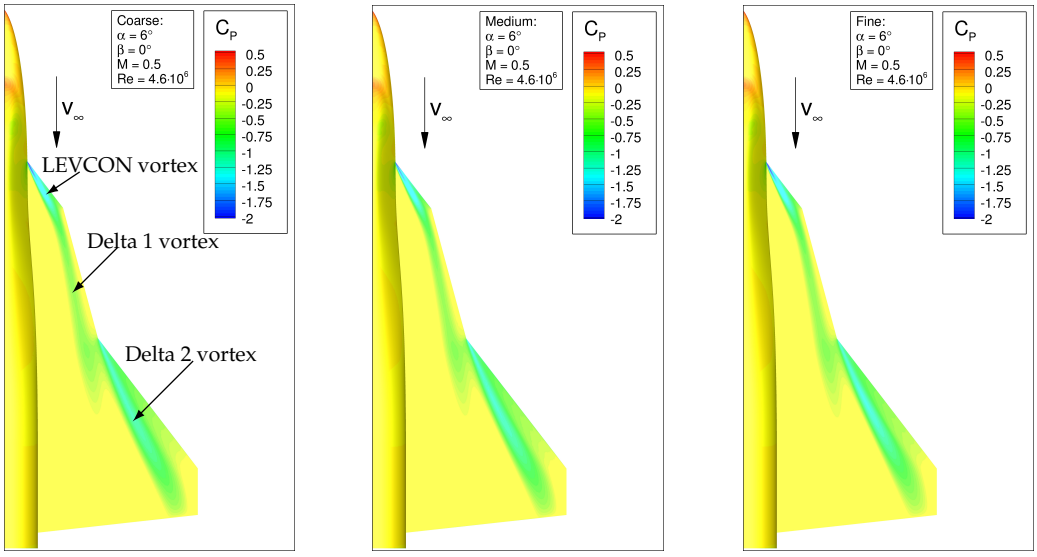
# Computational Results

For this study, several numerical simulations have been performed. The first one is made for the grid generation process, where three grid refinements were tested. In the second study, it will be discussed how the different turbulence models are predicting the flow physics of the double delta wing configuration. Since the wind tunnel tests had a different Reynolds number from the initial simulations, the Reynolds number effect will be discussed as well. Finally, a comparison between experimental data and computational simulations results will also be discussed. (All Figures not seen throughout this chapter can be seen in the Appendix A)

## 7.1 Grid sensitivity study

Grid sensitivity simulations have been performed using a half model, for on-flow Mach number of $M_\infty = 0.5$, a Reynolds number of $Re = 4.6 \cdot 10^6$ and an angle of attack range from $\alpha = 2°$ to $\alpha = 10°$.

In **Figures 27 and 51** the surface pressure distribution ($C_P$) for the coarse, medium and fine grid at an AoA of $\alpha = 6°$ and $\alpha = 10°$ are depicted. In the flow topology, as seen in Figure 27a, there are three different vortices. For the three studied grids, there is no significant difference topology wise. This is the same scenario for results with an AoA of $\alpha = 10°$.

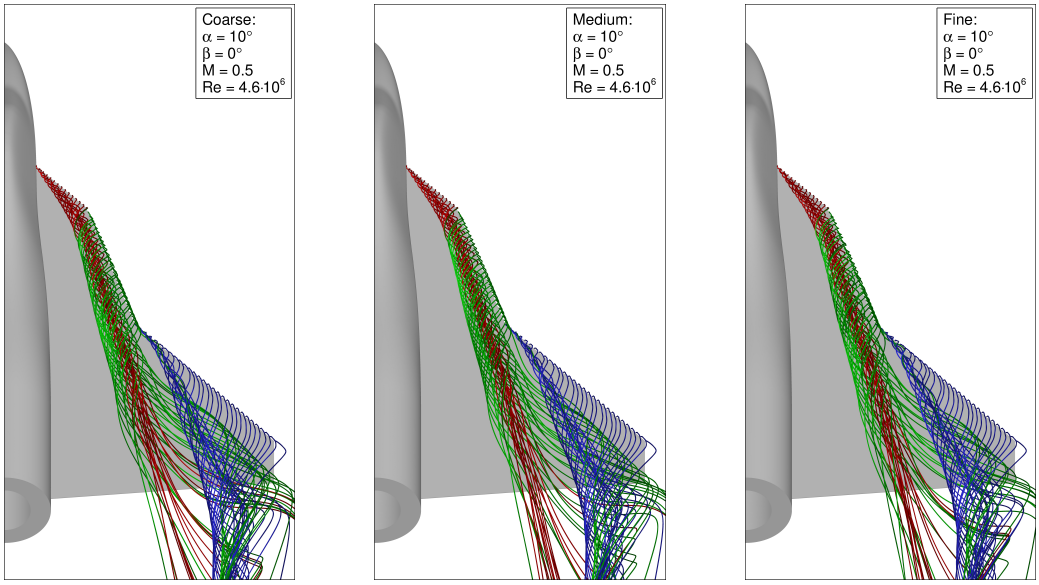



(a) (b) (c)

FIGURE 27: $C_P$ surface distribution for an AoA $\alpha = 6°$ of (a) coarse, (b) medium and (c) fine grid.

This can be confirmed when analysing the skin friction lines in **Figures 52 and 53**. These lines indicate friction velocity and the attachment and separation areas, depicted as $A_n$ and $S_n$, respectively. As seen in the $C_P$ distribution, the topology remains the same for all grids. Even for a higher AoA, when comparing the grid resolution, there is not a noticeable difference, although there is a difference with an augmented AoA as the attachment line $A_1$ moves inboard and there is no $A_2$.

The total pressure distribution, in **Figures 54 and 55**, show values of total pressure on the upper surface of the wing. There is a slight difference on the size of Delta 1 vortex with increasing grid refinement at an AoA $\alpha = 10°$. That is, for the finer grid, in Figure 55c, the Delta 1 vortex at the trailing edge is, on a small scale, wider when comparing to other grids. In **Figures 28 and 56**, a three dimensional view of the velocity on the upper side of the wing is shown. As expected, there is almost no difference whatsoever between grids but it allows for a 3D interpretation of the flow topology. In Figure 56a, unfortunately there is a break on the simulated streamlines that could not be overcome.




(a) (b) (c)

FIGURE 28: Streamlines on the wing upper surface for an AoA $\alpha = 10°$ for (a) coarse, (b) medium and (c) fine grid.

Although qualitatively there is not much difference as seen in the last Figures, analysis of $C_P$, lift $C_L$, drag $C_D$ and the pitching moment $C_m$ coefficients' quantities is advantageous for knowing differences in absolute values.

The $C_P$ quantity evaluation is depicted in **Figures 57, 58 and 59** for an AoA $\alpha = 6°$ and in **Figures 60, 61 and 62** for $\alpha = 10°$. Results for a medium and fine grid are closer to each other when compared to the the coarse grid. These values have been plotted at different $x = constant$ locations along the wing as showed in Figure 57 where the colour of each location coincides with the colour of the different $C_P$ curve.

In each of the Figures 57, 58 and 59 there are two highlighted circular areas: **A** and **B**. In the first location, area A represents the attachment area caused by the $A_1$ line, where the fine grid has a pressure increase in comparison with coarse and medium grids. In area B, albeit not representing much difference between grids, it is important to mention that this low pressure peak represents the LEVCON vortex. When looking at the second location at $x = 0.4m$ from the nose, while area A is again the representation of an attachment line $A_1$ on the wing surface, area B is depicting the Delta 1 vortex with slightly

difference in the peak value for the fine grid in comparison with the other two grids. At the last studied location, where differences are more visible, area A is now representing the second attachment line $A_2$ and area B the Delta 2 vortex. There is a higher difference in the $C_P$ quantity in both highlighted areas in comparison with previous locations. Furthermore, for $x = 0.4m$ and $x = 0.55m$ slices the medium and fine grid, besides having a lower peak pressure, it is slightly outboard in comparison with the coarse grid.

Similar conclusions can be taken for results obtained with an AoA $\alpha = 10°$, where the highlighted areas represent the same for each low or high peak. With the exception of the area A since there isn't an second attachment line depicted in the surface in Figure 53. In Figure 62 the peak in area A can be interpreted by analysing the $C_P$ surface and the total pressure distribution, where the presence of both Delta 1 and Delta 2 vortices is visible. So this area represents a division between vortices that indicates an eminent merging phenomenon.

Finally, an aerodynamic coefficient performance comparison has been made. In **Figure 29** these coefficients are compared between the three grids. Firstly, they all have the same characteristic curve for each coefficient. Looking at each curve individually, there is no difference in lift or drag, but pitching moment that is not the case. Although not significantly, there is a small effect that causes a parallel shifting of values for the fine grid in comparison with the coarse and medium grid.

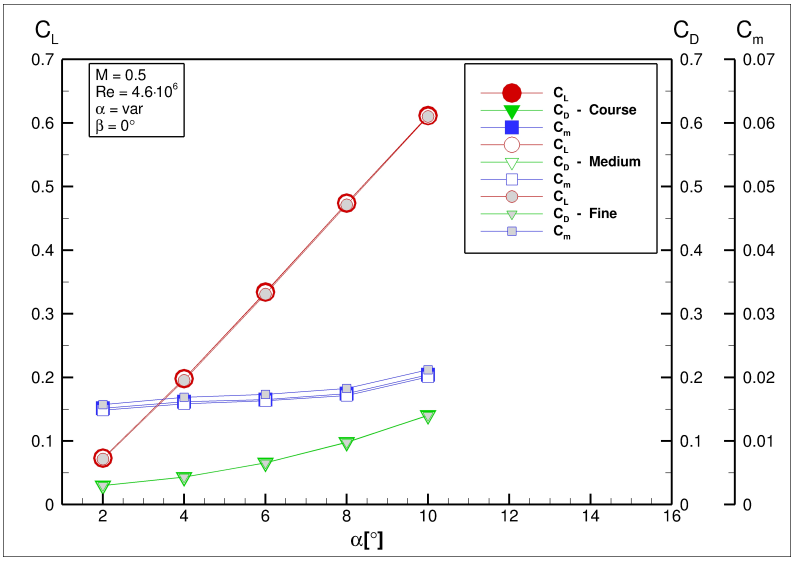



FIGURE 29: Comparison of $C_L$, $C_D$ and $C_m$ values between the three generated grid for multiple AoA.

This sensitivity study allows to choosing between grids, and this comparison, quantitative and qualitative, lead to choose, for the following simulations, the medium grid. Even though its results are very similar to the fine grid's and are better than the coarse one's, medium grid presents a lower computational cost because it has less refinement.

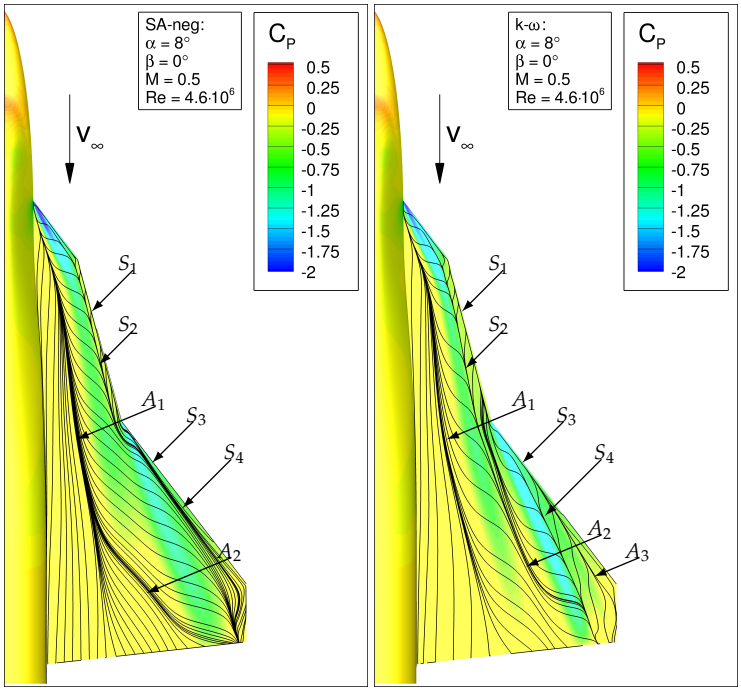
## 7.2 Turbulence model sensitivity study

For the turbulence model sensitivity study the same reference values for flow conditions have been used. This study has been performed using the full model configuration for the study of the Spalart-Allmaras negative and k-$\omega$-TNT turbulence models and the half model for k-$\omega$ and RSM. Nevertheless, since symmetric on flow conditions have been applied this will not be a disturbance in obtained results, with the exception of $C_l$ for the

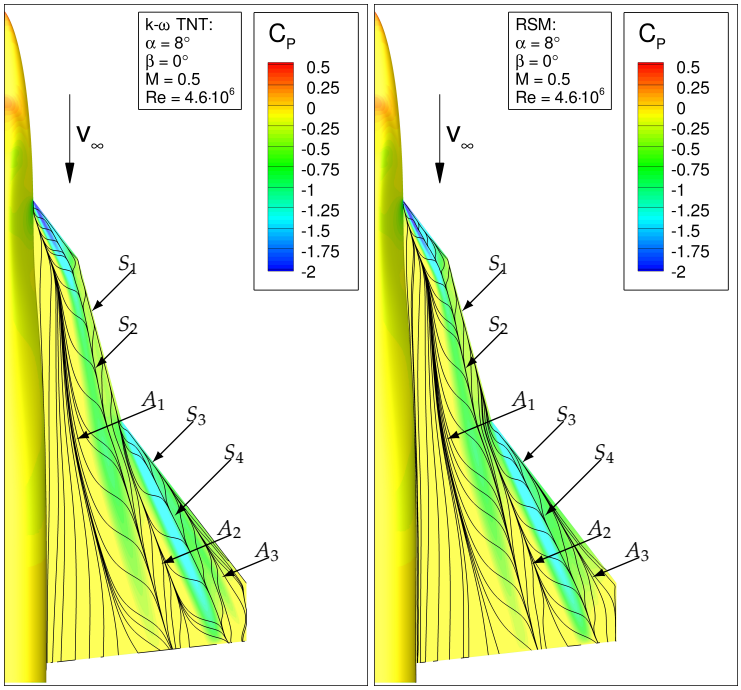
same reason stated before. The comparison shown in the current chapter has been done for an AoA of $\alpha = 8°$.

Surface pressure distribution is depicted in **Figure 63** for Spalart-Allmaras negative (SA-neg), k-$\omega$, k-$\omega$-TNT and Reynolds Stress Model (RSM). The surface topology in this comparison is more disparate than the previous one. Firstly, it is clear that k-$\omega$, k-$\omega$-TNT and RSM models have a closer topology than the SA-neg. This is visible in the Delta 1 vortex footprint extension, where from k-$\omega$ to RSM this topology gets longer and thinner. The Delta 2 vortex also becomes thinner for more sophisticated turbulence models and furthermore, the different topology in this area could indicate a different suction level.

These differences between turbulence models are visible as well when plotting the skin friction lines in **Figure 30**. For the SA-neg topology there are four separation lines and two attachment lines, while the other three models present one more attachment line. As seen in Chapter 2, the vortex arises between an attachment line and a separation line. The topology of this configuration shows that the flow at Delta 1 (D1) separates at the sharp leading edge, depicted as $S_1$, and attaches again at $A_1$. In the kink at the end of D1 and start of Delta 2 (D2) there is an attachment line formation, $A_2$, captured by the turbulence models, except for SA-neg. Between this attachment line and $S_2$ is there is D1 secondary vortex. Similar topology evaluation can be done for D2, while the primary vortex is maintained between $S_3$ and $A_2$, a secondary vortex is formed between $S_3$ and $A_3$. This can be analysed with the Figures depicted in Chapter 2 about the saddle point. While there is the LEVCON vortex, due to flow separation at the leading edge, it is immediately absorbed by the Delta 1 vortex, i.e. they are merged, as seen in the streamlines Figures in the previous section, so it is treated as one vortex named D1 vortex.




(a) (b)




(c) (d)

FIGURE 30: $C_P$ surface distribution with skin friction lines for an AoA $\alpha = 8°$ with (a) SA-neg, (b) k-$\omega$, (c) k-$\omega$ TNT and (d) RSM turbulence model.

When interpreting each case, it is noticeable different footprints of Delta 1 vortex for SA-neg results; this is caused by the lack of capture of the $S_2$ extension and the $A_3$ emergence. Moreover in this area is noticeable the inboard direction of $S_2$ from SA-neg to RSM results. Both $S_2$ and $A_2$ lines in k-$\omega$-TNT and in RSM are longer than in k-$\omega$, even reaching the trailing edge. The secondary vortex is caused by suction at the leading edge and it will influence the primary's vortex location and size.

In **Figure 64**, the total pressure on the upper surface of the wing is plotted. In **Figure 64a** the different vortex cores are highlighted, except for *wing tip vortex*, represented in **Figure 64b**, since the SA-neg did not significantly captures it. The comparison made using these Figures allows a better visualization of differences that each vortex footprint has from one turbulence model to another. This can be seen in the interaction between Delta 1 and Delta 2 vortices. The SA-neg model has a different topology characterization from due to capture of interactions and vortex formation in a different way than other models. Arise of a wing tip vortex at the trailing edge and a secondary vortex on Delta 1, depicted in **Figure 64c**, confirms the missing topology characteristics in SA-neg results.

The highlighted box in **Figure 64c** is shown in **Figure 31**. This zoomed in vortex-vortex interaction is depicted along with the velocity vectors, where is described a counter-rotation between the core of each vortex. This counter rotation confirms the existence of a secondary vortex, as predicted by the attachment line $A_3$, caused by suction at the leading edge. Its presence will influence the size and location of the primary vortex, the Delta 1 vortex. As the angle of incidence increases, the secondary vortex will get wider and therefore it will push the primary vortex in the inboard direction. A similar sketch of Figure 3b was done including all friction effects not previously represented. This sketch, in **Figure 32** has a simplified 2D visualisation of what is happening in Figure 31.

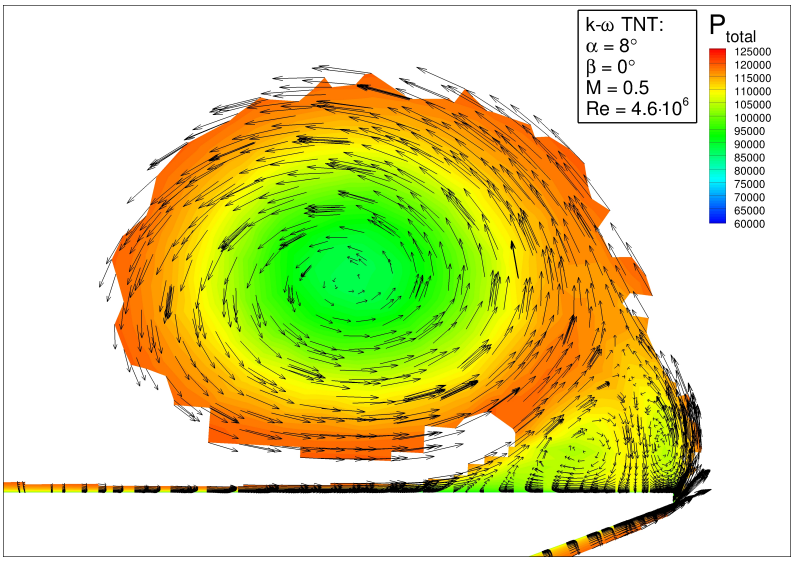



FIGURE 31: Total pressure projected with velocity vectors in a perpendicular view along the vortex core for k-$\omega$ TNT turbulence model at Delta 1 with an AoA of $\alpha = 8°$.

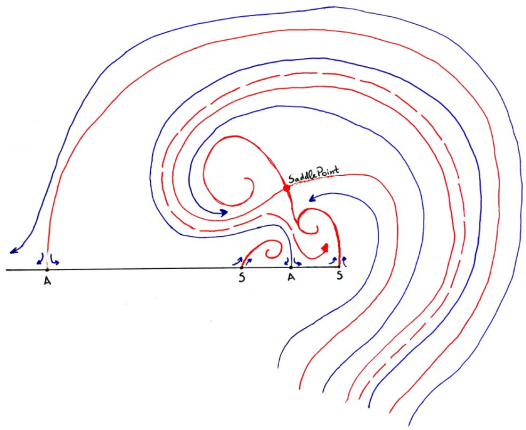



FIGURE 32: Hand made sketch representing a simplified topology of the secondary vortex interaction with the primary one as seen in the latter Figure.

The other highlighted area in the k-$\omega$ TNT figure is depicted in **Figure 65** representing the interaction between two vortices. This topology, explained in chapter 2 is just some of the possible examples to show the complexity of the vortex formation on the upper surface of a multiple delta wing. Both figures were taken in the perpendicular direction of the vortex core, i.e. perpendicularly to the leading edge.

The $C_P$ quantity evaluation for the first location at $x = 0.3m$ is depicted in **Figure 66**. Here it is visible the similarity between SA-neg and k-$\omega$ and between k-$\omega$ TNT and RSM. In the LEVCON vortex highlighted area, contrasts between models are clear, where the size, value and location of the vortex are different. In **Figure 67**, although with different values, k-$\omega$, k-$\omega$ TNT and RSM captures the secondary vortex that it is influencing the size and location of Delta 1 vortex. This can be said for the analyses at $x = 0.55m$, depicted in **Figure 68**, where the presence of $A_2$ and $A_3$ attachment lines influence the primary vortices Delta 1 and Delta 2; and a higher discrepancy for $C_P$ quantities in comparison with the SA-neg model.

The aerodynamic coefficients, in **Figure 33**, are also compared in this study. It is evident that there is no influence for lift and drag, however the pitching moment has a parallel shift between models. This is provoked by the different topology each model has, since there are changes for the loads on the surface upper side. The high difference at $\alpha = 10°$ between SA-neg and the other models can be caused by these load distribution changes, namely for the rear load.

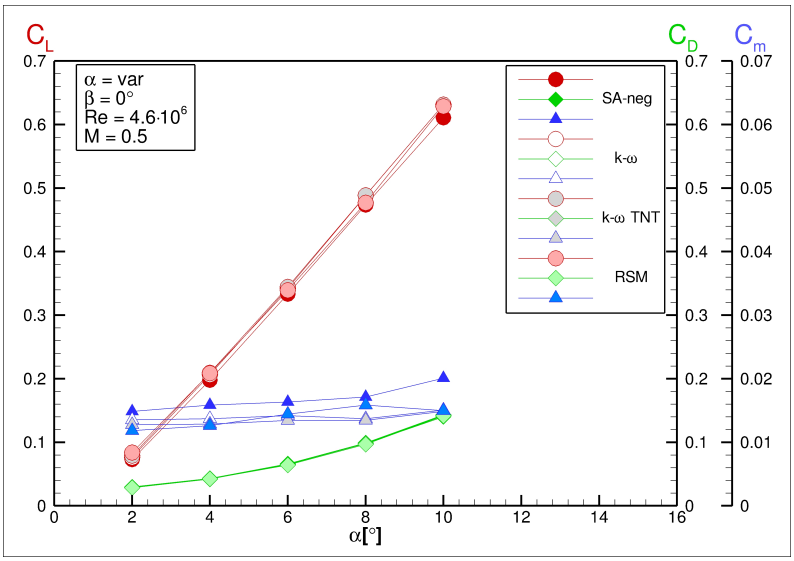


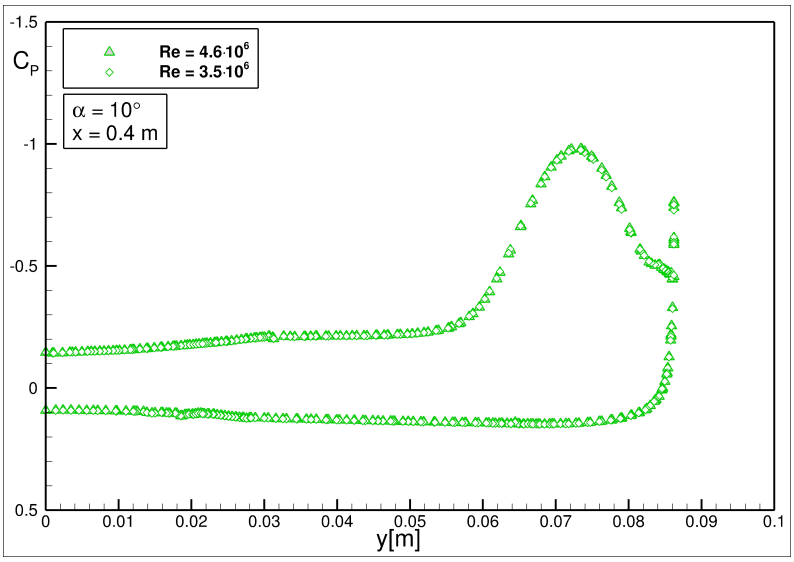

FIGURE 33: Comparison of $C_L$, $C_D$ and $C_m$ values between the four turbulence models used for the multiple AoA simulated.

Although further discussed in the last section of this chapter, the more sophisticated turbulence model, i.e. the more complex and physically complete, is expected to be more close to the experimental data. Therefore, the RSM results are predicted to be the closest to real in flight flow conditions.

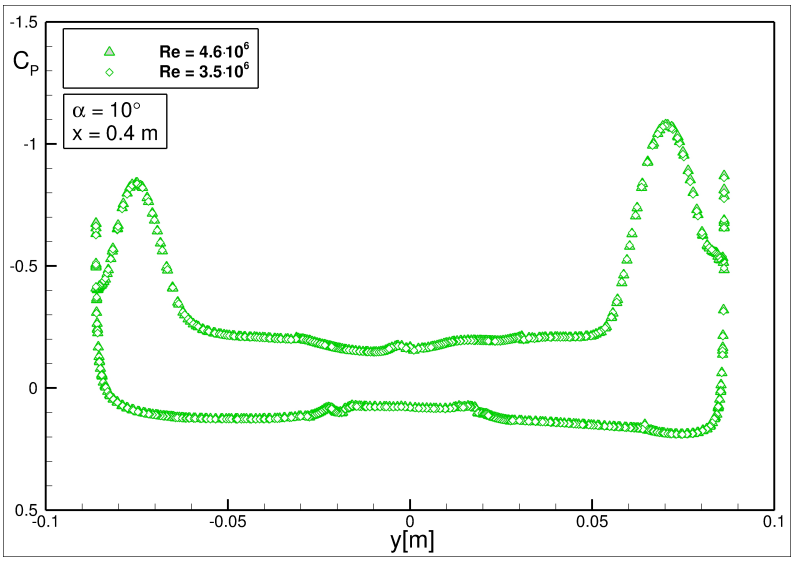
## 7.3 Reynolds Number Effect

The experimental results were obtained after the start of this investigation and it was necessary to change the Reynolds number used to be coincident with experimental data. For this reason, a comparison of the numerical results for the two different Reynolds number have been done for symmetric and asymmetric on flow conditions. The Mach number maintains the same and comparisons were made for SA-neg turbulence model for an AoA of $\alpha = 10°$.

As seen in surface pressure distribution, in **Figure 69 and 70**, for the symmetric and asymmetric on flow conditions, respectively, there is no visible difference between the two different Reynolds numbers of $Re = 4.6 \cdot 10^6$ and $Re = 3.5 \cdot 10^6$. When adding the skin friction lines, in **Figures 71 and 72**, the lack of difference is also noticeable. As expected the data for the $C_P$ values, in **Figure 34**, do not present visible differences as well.




(a)




(b)

FIGURE 34: Comparison of $C_P$ values between the two Reynolds number used for (a) symmetric and (b) asymmetric on flow conditions.

The small difference in using different Reynolds number can be confirmed when analysing the aerodynamic coefficients. While for the symmetric on flow conditions, in **Figure 35**, the values are almost coincident, as for the asymmetric, in **Figure 36**, the $C_m$ and $C_l$ present a larger difference than for the other coefficients comparison but it is nevertheless negligible. However, in order to obtain closest results to the experimental data, the Reynolds number to be used for the final section and comparisons is $Re = 3.5 \cdot 10^6$.

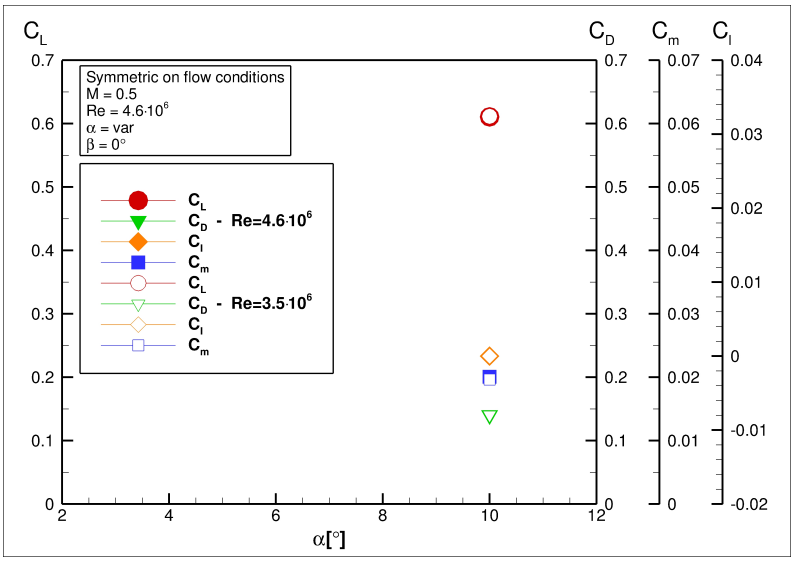



FIGURE 35: Comparison of $C_L$, $C_D$ and $C_m$ values between the different Reynolds number used in symmetric on flow conditions.

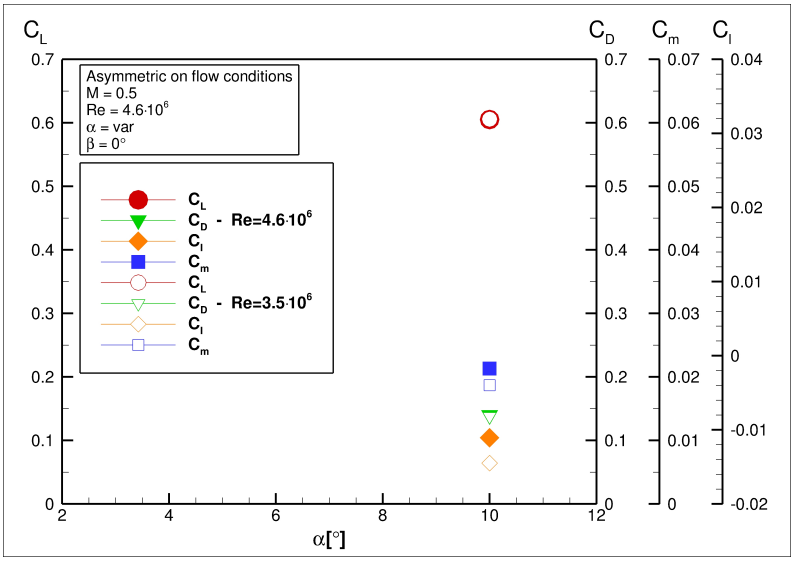



FIGURE 36: Comparison of $C_L$, $C_D$ and $C_m$ values between the different Reynolds number used in asymmetric on flow conditions.

## 7.4 Experimental data comparison

Data obtained from the wind tunnel tests in the DNW-TWG have been used to be compared with the results from simulations of the different used turbulence models. A comparison has been made for symmetric and asymmetric on flow condition. While for the symmetric flow the SA-neg, k-$\omega$, k-$\omega$ TNT and RSM were applied to be compared with the experimental data, for the asymmetric flow only the SA-neg and RSM models were used.

Comparison for symmetric on flow condition, of the aerodynamic coefficients is shown in **Figures 37, 38, 39 and 40**. Until AoA of $\alpha = 17°$ the SA-neg results present similar values and the same gradient, for lift and drag. In this comparison the $C_m$ numerical results

are over predicted and present a similar gradient until the AoA of $\alpha = 14°$. However, results obtained for higher incidence are under predicted and do not have a similar curve characteristics. Moreover, the discontinuity between $\alpha = 14°$ and $\alpha = 15°$ is not even slightly captured. Results from k-$\omega$ and k-$\omega$ TNT compared with the experimental data can be described as very similar for lift, drag and pitching moment coefficients. The latter coefficient, on the contrary, is under predicted when using SA-neg for the same AoA range.

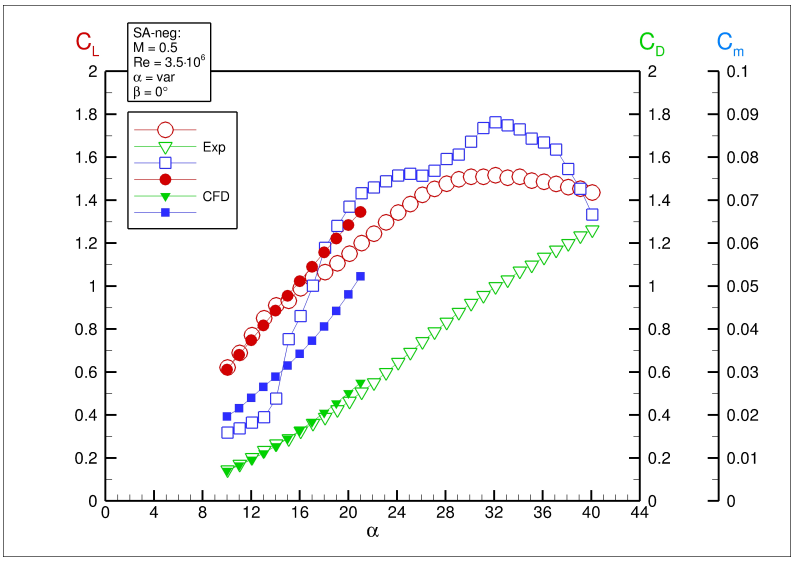



FIGURE 37: Comparison of $C_L$, $C_D$ and $C_m$ values between SA-neg turbulence model and experimental data for the multiple AoA simulated and tested.

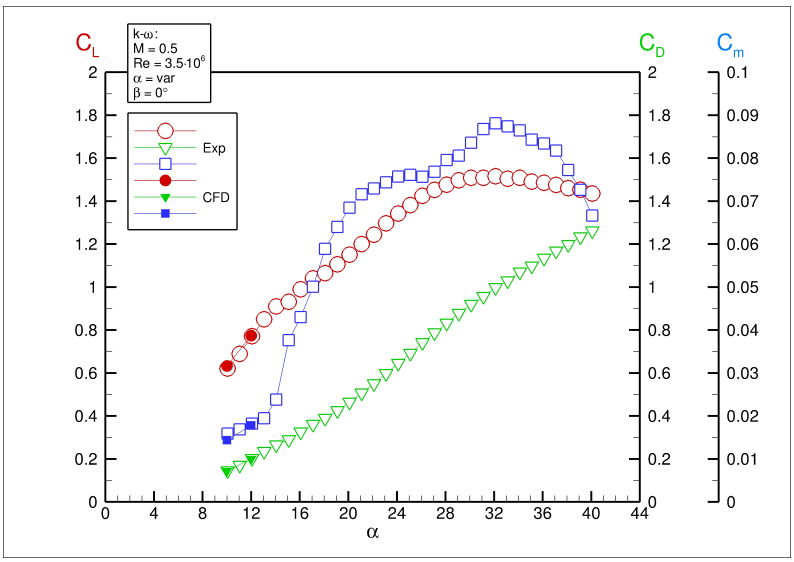



FIGURE 38: Comparison of $C_L$, $C_D$ and $C_m$ values between k-$\omega$ turbulence model and experimental data for the multiple AoA simulated and tested.

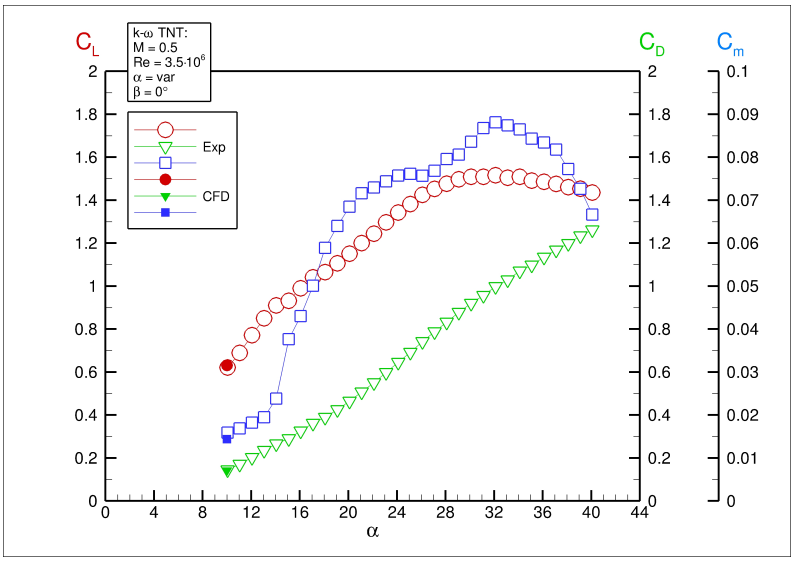



FIGURE 39: Comparison of $C_L$, $C_D$ and $C_m$ values between k-$\omega$ TNT turbulence model and experimental data for the multiple AoA simulated and tested.

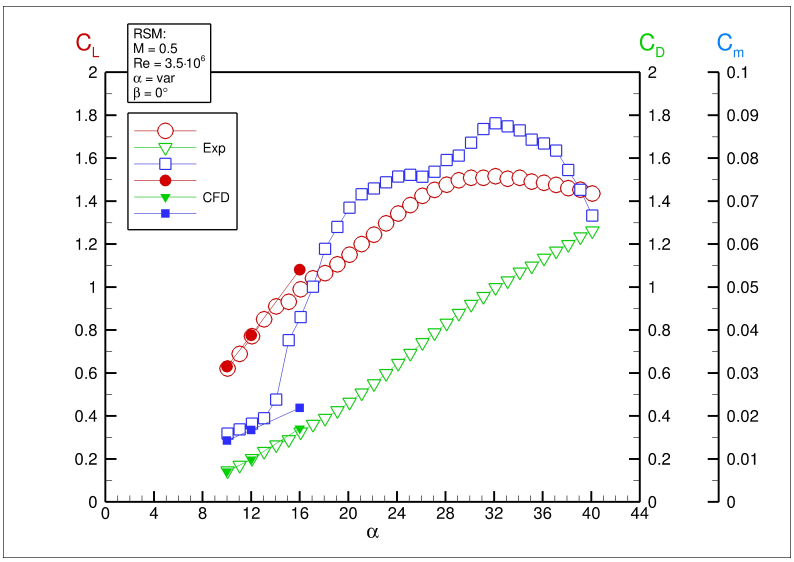



FIGURE 40: Comparison of $C_L$, $C_D$ and $C_m$ values between RSM turbulence model and experimental data for the multiple AoA simulated and tested.

The last compared turbulence model, RSM, has the same previously described behaviour for lift and drag. $C_m$ curve characteristics are the same than the experimental one at $\alpha = 10°$ and $\alpha = 12°$. However at $\alpha = 16°$ the gradient and value are different. Even though RSM is the most sophisticated turbulence model nevertheless its not accurately predicting the $C_m$ quantity and gradient. For some simulated angles of attack, even though the integral data is getting captured correctly it doesn't mean that the topology will be correctly represented.

For the topology comparison, the PSP results are depicted side by side with the simulated surface pressure distribution as seen in **Figures 73, 74, 75 and 76**. As referred before, although the aerodynamic coefficients quantities in the SA-neg are close to the experimental data the surface topology is not as close. For all AoA depicted Delta 1 and Delta 2 vortices it has a wider footprint causing as well a larger merging phenomenon

than the PSP results. The footprint gets similar when comparing with k-$\omega$ however both vortices are once again wider, the merging footprint is closer than the experimental surface pressure distribution. There are the same similarities and differences for k-$\omega$ TNT results but the Delta 2 vortex it is depicted slightly thinner, being closer to the PSP surface. Comparing the wind tunnel data with the RSM model, it is visible the similarities and differences seen in the last two models. Moreover, in **Figure 41**, focusing in the two highlighted circular areas is possible to see a different topology. This could be the reason for the low $C_m$ quantity at this AoA since there is a wider merged vortex causing a higher rear loading.

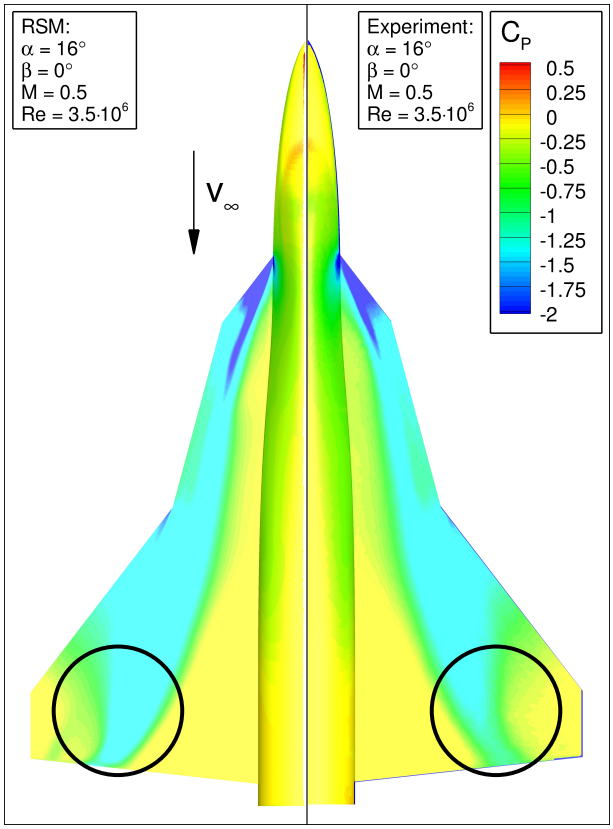
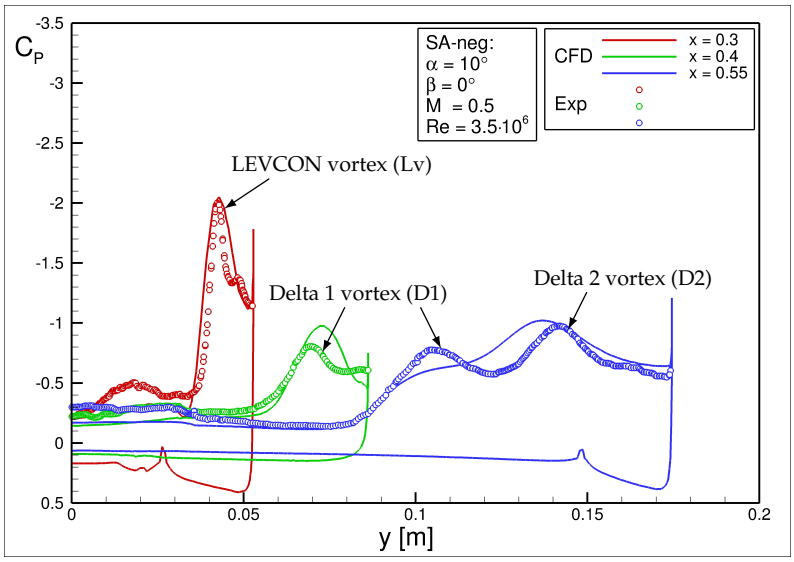
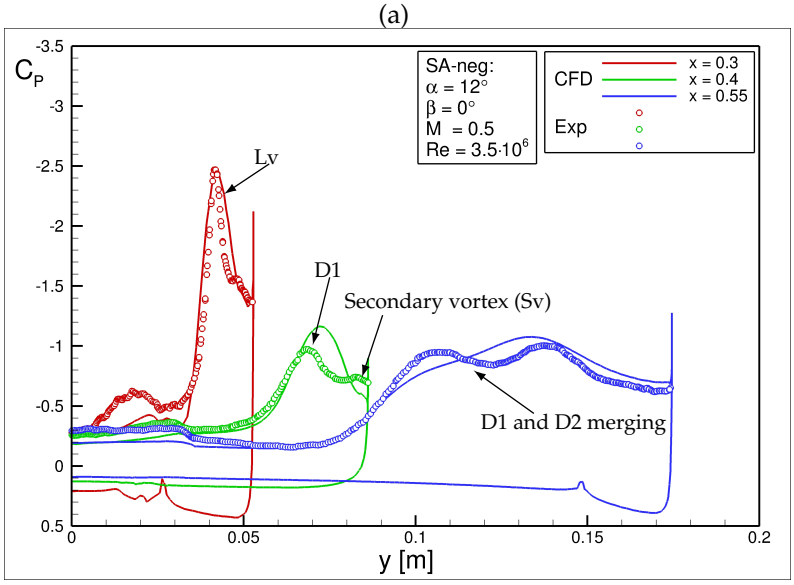



FIGURE 41: $C_P$ surface distribution resulting from RSM simulations for an AoA of $\alpha = 16°$ in comparison with PSP results.

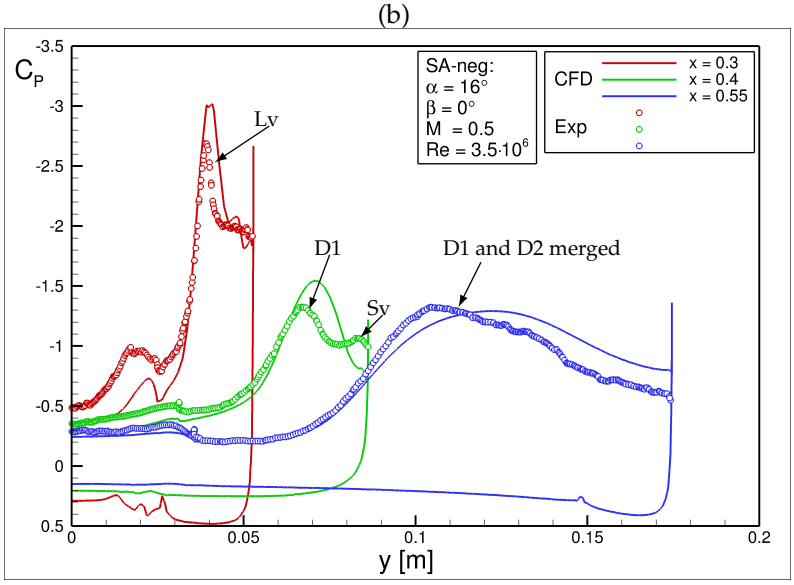
The $C_P$ evaluation between CFD and experiments is depicted in **Figures 42, 43, 44 and 45**, where the arrows are indicating what each low pressure peak means, the LEVCON vortex, Lv in short, the Delta 1 vortex, D1, the Delta 2 vortex, D2 and the secondary vortex, Sv. The SA-neg, in Figure 42, present the least accurate results, except for the LEVCON peak, where for the first two AoA depicted, values are very close to experiments results. All other vortices are wrongly predicted and off place, and the secondary vortex it is not captured at all for any AoA. The higher AoA at $\alpha = 16°$ depicted in **Figure 42c** there is a very small simulated secondary vortex at LEVCON, a phenomenon that is not happening in the experiments at this AoA.




(a)

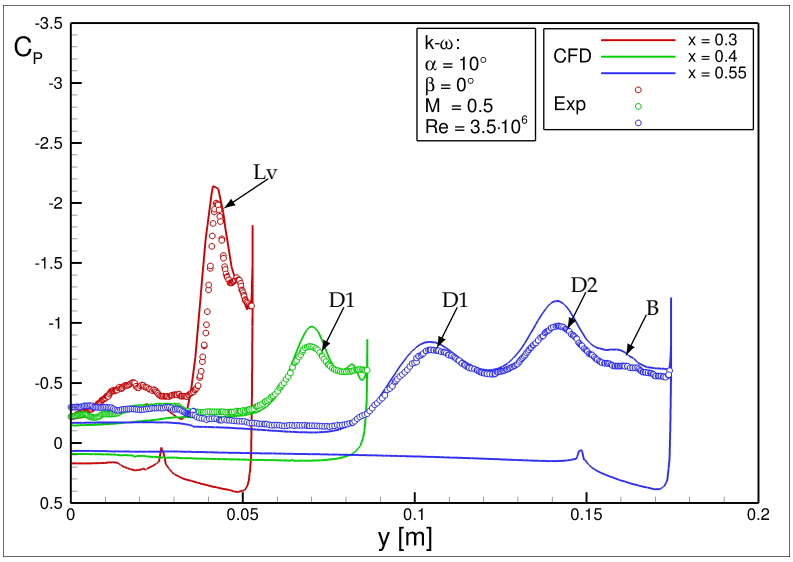



(b)

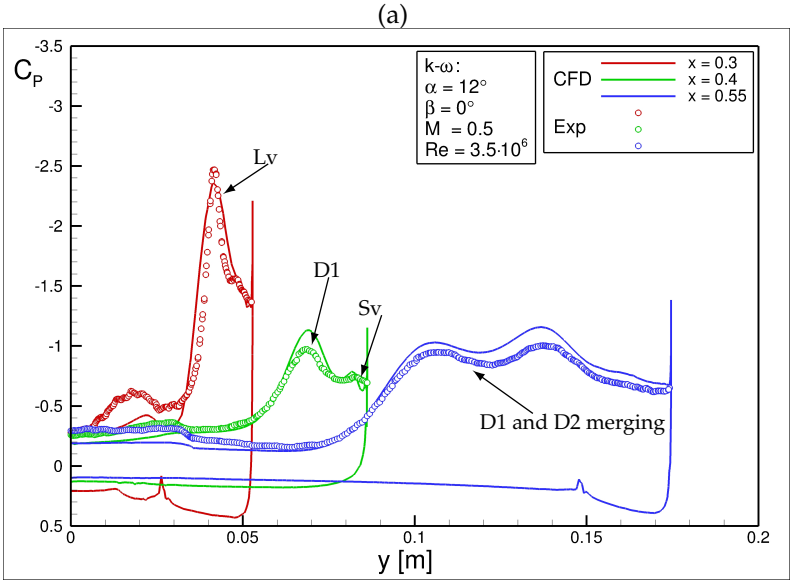



(c)

FIGURE 42: $C_P$ quantities resulting from SA-neg simulations for an AoA of (a) $\alpha = 10°$, (b) $\alpha = 12°$ and (c) $\alpha = 16°$ in comparison with PSP results.




(a)




(b)

FIGURE 43: $C_P$ quantities resulting from k-$\omega$ simulations for an AoA of (a) $\alpha = 10°$ and (b) $\alpha = 12°$ in comparison with PSP results.

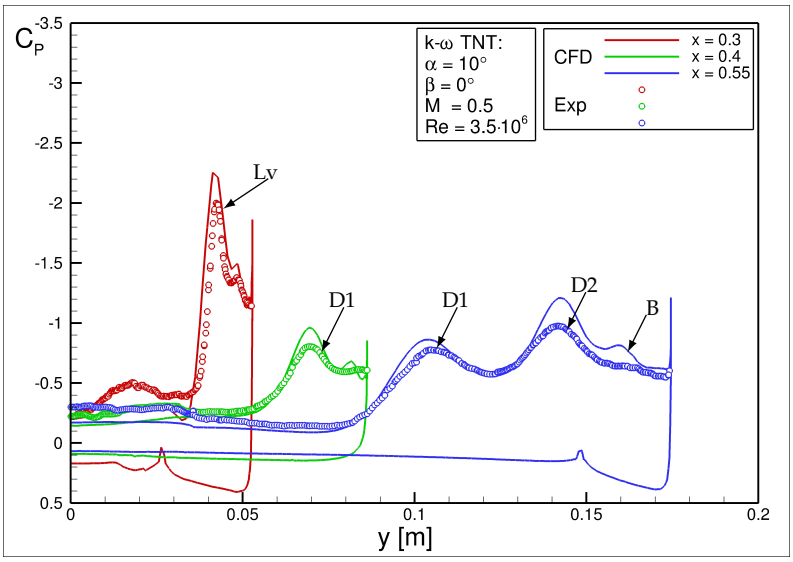
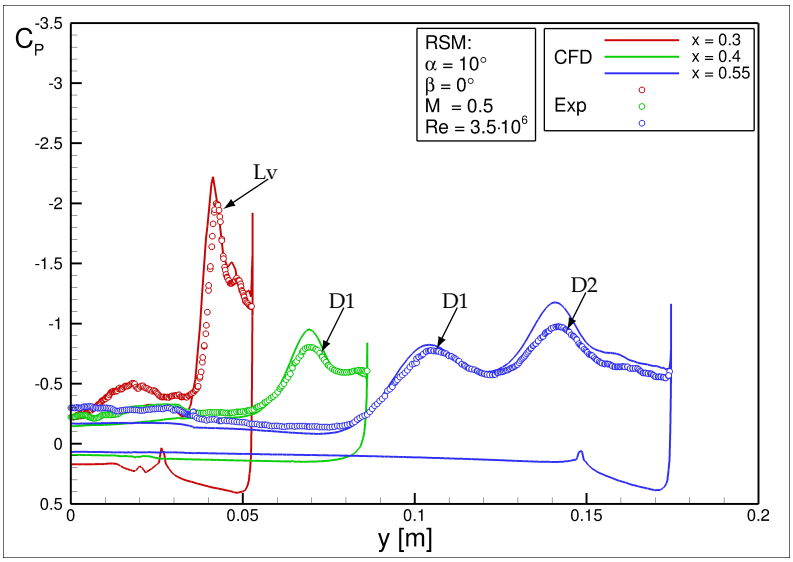



FIGURE 44: $C_P$ quantities resulting from k-$\omega$ TNT simulations for an AoA of $\alpha = 10°$ in comparison with PSP results.




(a)

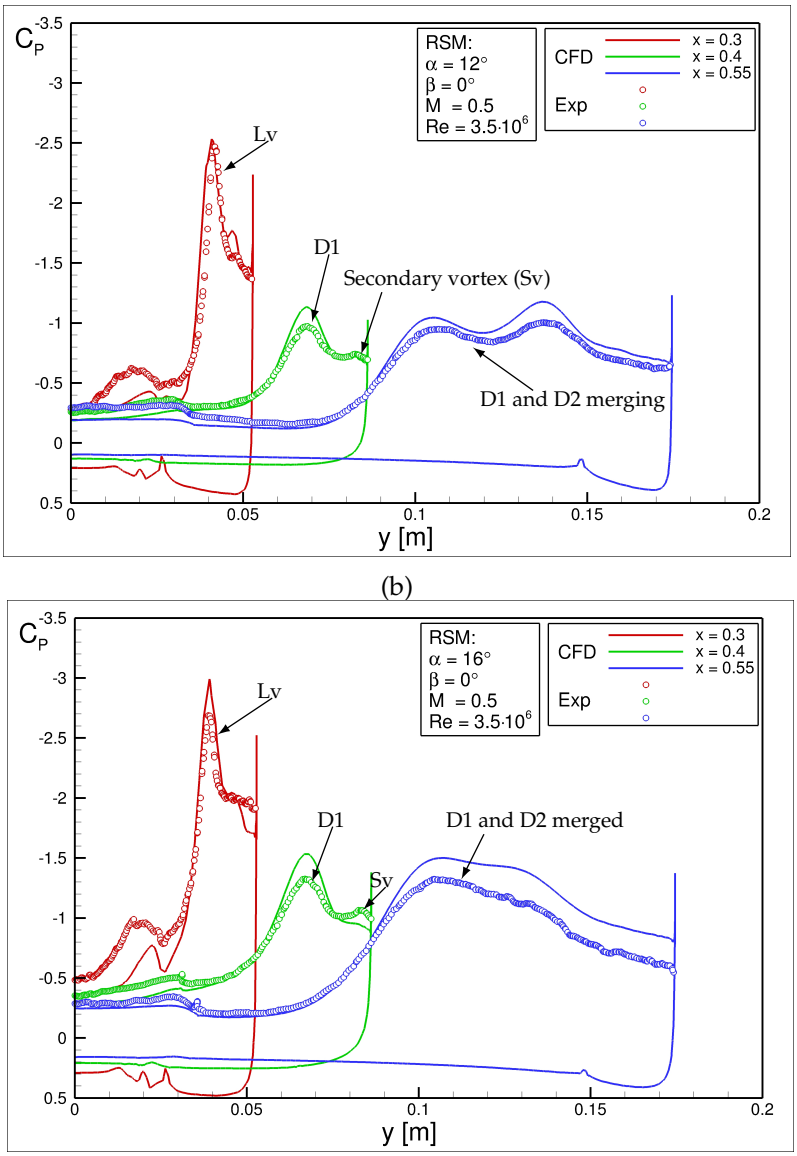



FIGURE 45: $C_P$ quantities resulting from RSM simulations for an AoA of (a) $\alpha = 10°$ and (b) $\alpha = 16°$ in comparison with PSP results.

When applying k-$\omega$ numerical method, the results, for both AoA, present a much closer curve characteristic. Although with poor accuracy on the vortex level, including an over prediction for the secondary vortex, location of each vortex corresponds with the one that occurred in the experiments. This model is predicting a stronger secondary vortex, highlighted by the arrow **B** at Delta 2, which is almost undetectable in in experimental data results.

The k-$\omega$ TNT $C_P$ curve has very similar behaviour to the experimental data with slightly higher levels for LEVCON and Delta 1 vortex. However, for Delta 2 vortex, present a higher pressure peak disparity and a secondary vortex, at the leading edge as depicted by the arrow **B**, which is very small on the experiments.

Finally, the RSM model is compared and, as expected, it presents the closest characteristic curve to the PSP results. However, there is an over prediction for Delta 1 and Delta 2 vortices and for suction at LEVCON for an AoA of $\alpha = 10°$, in Figure 45a. This

inaccuracy for the $C_P$ values happens at the other depicted Figures 45b and 45c respectively for an AoA of $\alpha = 12°$ and $\alpha = 16°$. For the lower AoA the secondary vortex is accurately calculated, although for the highest AoA it is very under predicted being almost nonexistent.

When analysing the asymmetric on flow conditions, besides the previously mentioned coefficients, the rolling moment is compared since it is a significant and sensitive coefficient for the stability prediction of the model configuration. In **Figures 46 and 47**, results from SA-neg and RSM, respectively, in comparison with the experimental data are depicted.

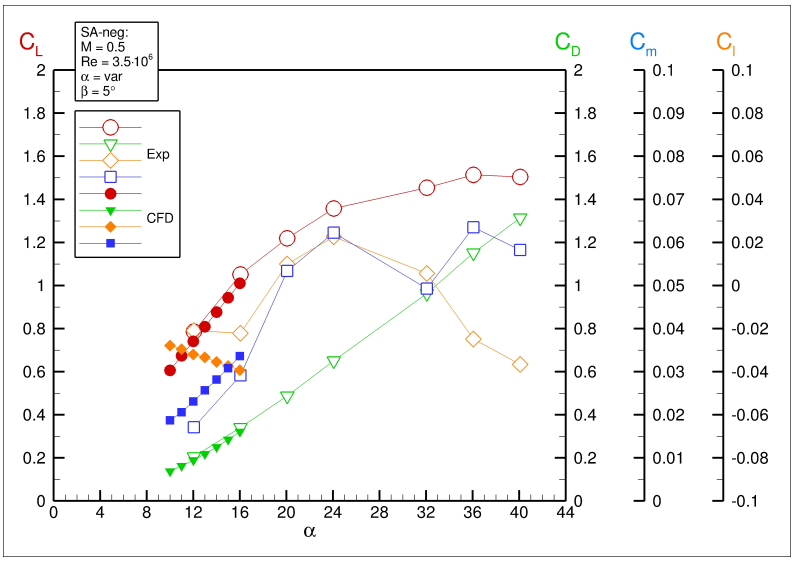



FIGURE 46: Comparison of $C_L$, $C_D$ and $C_m$ values between SA-neg turbulence model with experimental data for the multiple AoA simulated and tested.

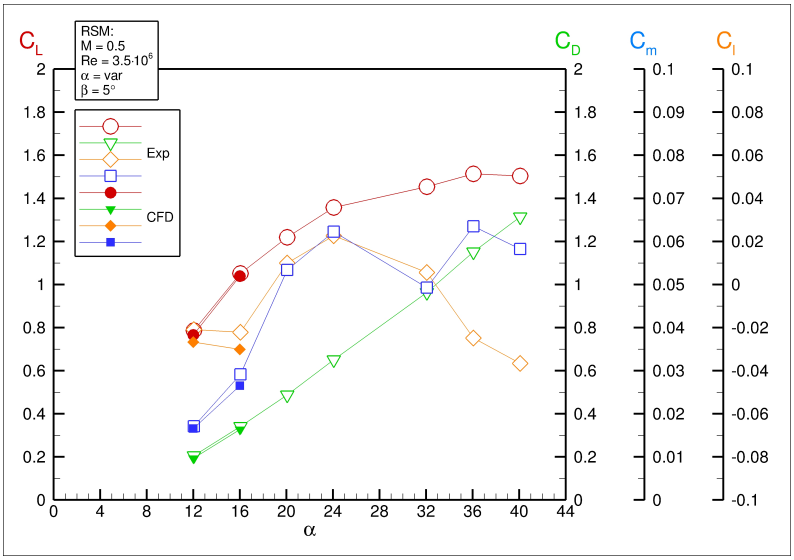



FIGURE 47: Comparison of $C_L$, $C_D$ and $C_m$ values between RSM turbulence model with experimental data for the multiple AoA simulated and tested.

The SA-neg computational results present the same curve characteristic and similar

value for lift as for drag. While the pitching moment is over predicted, the rolling moment is highly under predicted but both present a similarity for the curve gradient. The inaccurate calculation for surface pressure distribution leads to results obtained for $C_m$ and $C_l$. On the contrary, RSM turbulence model present much closer results to the experiments and almost the exact same curve characteristics. The results obtained for the tested angles of attack seem very promising for higher AoA. Nevertheless, the difference for the values of rolling and pitching moment cannot be over looked as for it is very important to accurately predict the configuration stability.

Topology wise, surface pressure distribution present a closer resemblance to the PSP results than the aerodynamic quantities, as depicted in **Figure 77** for an AoA of $\alpha = 12°$ and in **Figure 48** for $\alpha = 16°$. SA-neg surface has a clear difference from the PSP surface, as depicted for the AoA of $\alpha = 12°$, in **Figure 77a**, there are two different vortex footprint structures that are not captured by the SA-neg. A similar situation is noticeable for the AoA of $\alpha = 16°$, in **Figure 48a**, where the footprint of the merged vortex on the left wing surface is wider than the one in the experimental results. Furthermore on the right wing surface there is an over prediction of the LEVCON vortex that is compasated by the wider Delta 1 and Delta 2 vortices, hence the not so different absolute values for the aerodynamic coefficients.

Likewise the symmetric comparison, the RSM presents a better footprint representation of what was captured in the experiments. As depicted in **Figure 77b** for the AoA of $\alpha = 12°$ the separation of Delta 1 and Delta 2 vortex is well captured by the RSM. Despite predicting a stronger LEVCON vortex, this simulated surface pressure distribution have a great qualitative accuracy. When increasing the AoA to $\alpha = 16°$ on the right side of the wing, the LEVCON vortex has been even more overly predict in comparison with the experimental result. However, the simulated topology near the trailing edge balances this inaccurate prediction, thus maintaining a reasonably high accuracy for the aerodynamic coefficients.

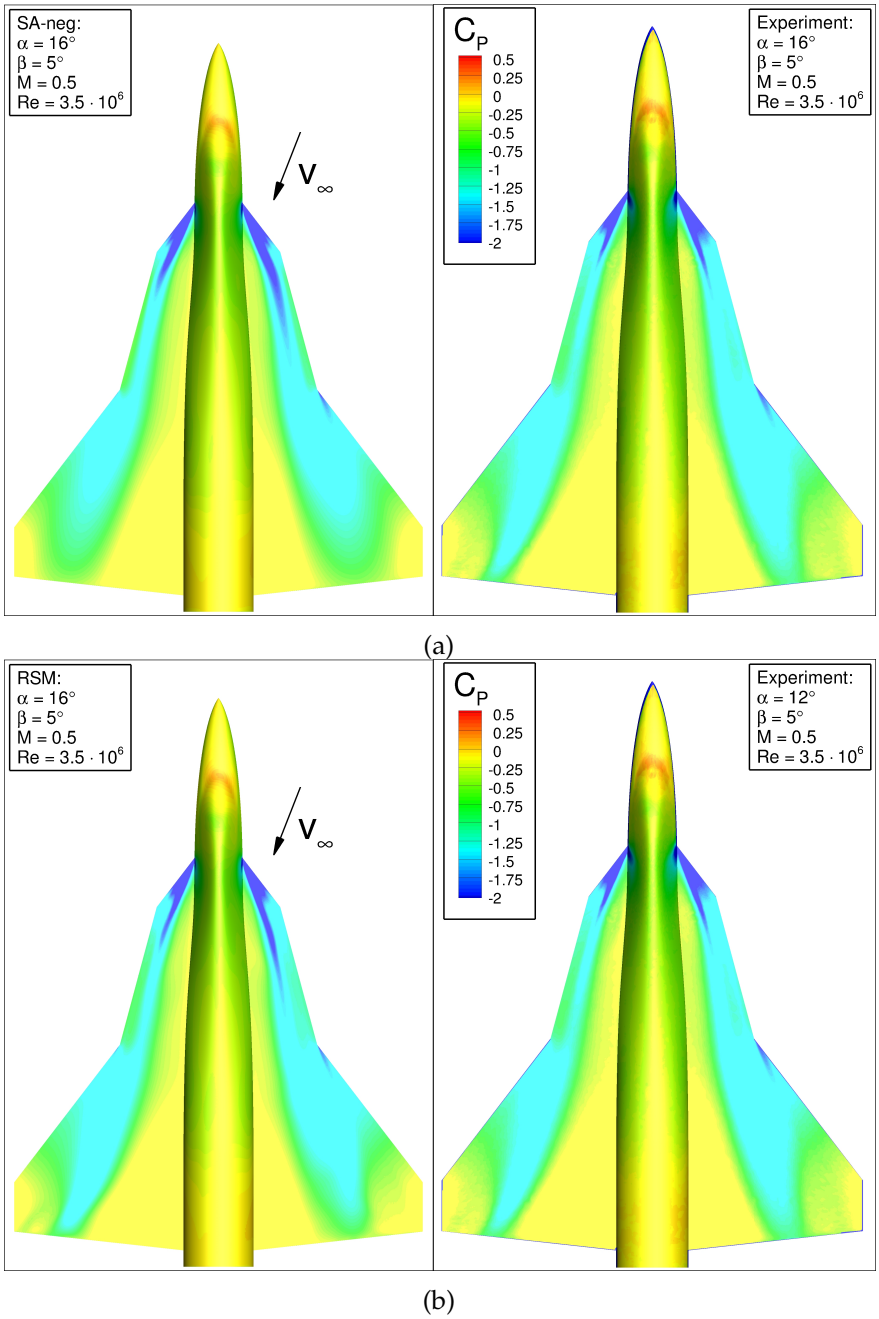
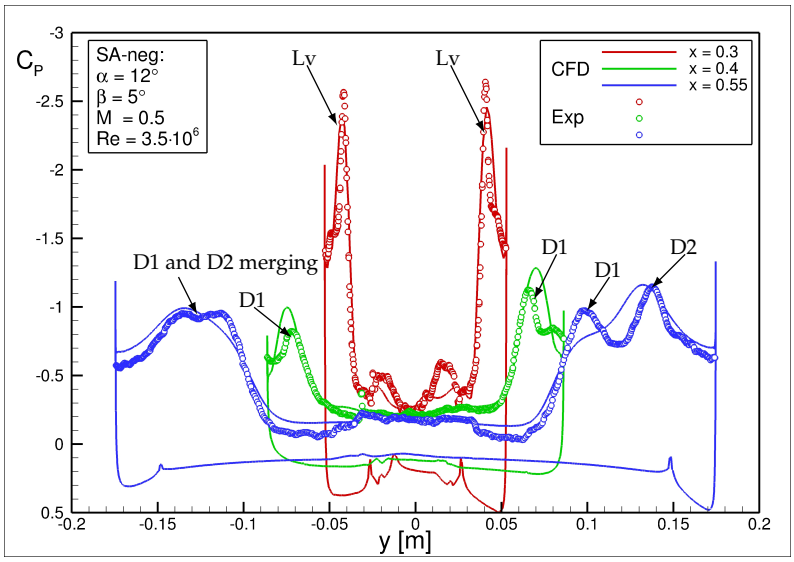
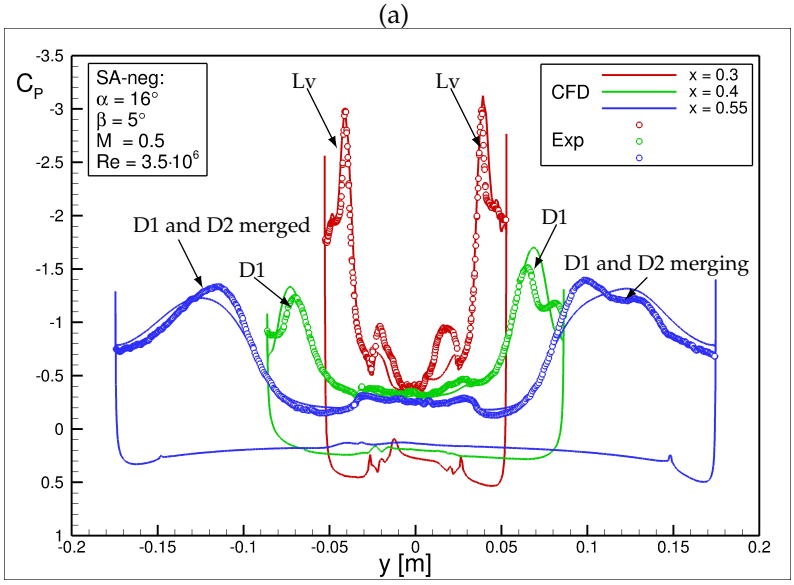



FIGURE 48: $C_P$ surface distribution resulting from (a) SA-neg and (b) RSM simulations for an AoA of $\alpha = 16°$ in comparison with PSP results.

To conclude this comparison, the $C_P$ integral data is plotted, as depicted in **Figures 49 and 50**, where the values of three longitudinal slices along a $x = constant$ are compared with the same location of the experimental data surface. The different vortices captured in PSP experiments are pointed out by the arrows drawn on the $C_P$ graphic. Results computed by SA-neg turbulence model accompanies, as expected, the differences seen in the surface pressure distribution. Similarly with the symmetric solution, this model does not accurately predict the topology starting at the end of LEVCON. For this comparison, neither the level, location and curve gradient are accurately calculated for both depicted AoA. On the other hand, the RSM results are, once more, closer to the experiments having a slightly over prediction for the vortex levels and an light divergence on curve characteristic for the merging phenomenon in both AoA.




(a)




(b)

FIGURE 49: $C_P$ integral data resulting from SA-neg simulations for an AoA of (a) $\alpha = 12°$ and (b) $\alpha = 16°$ in comparison with PSP results.

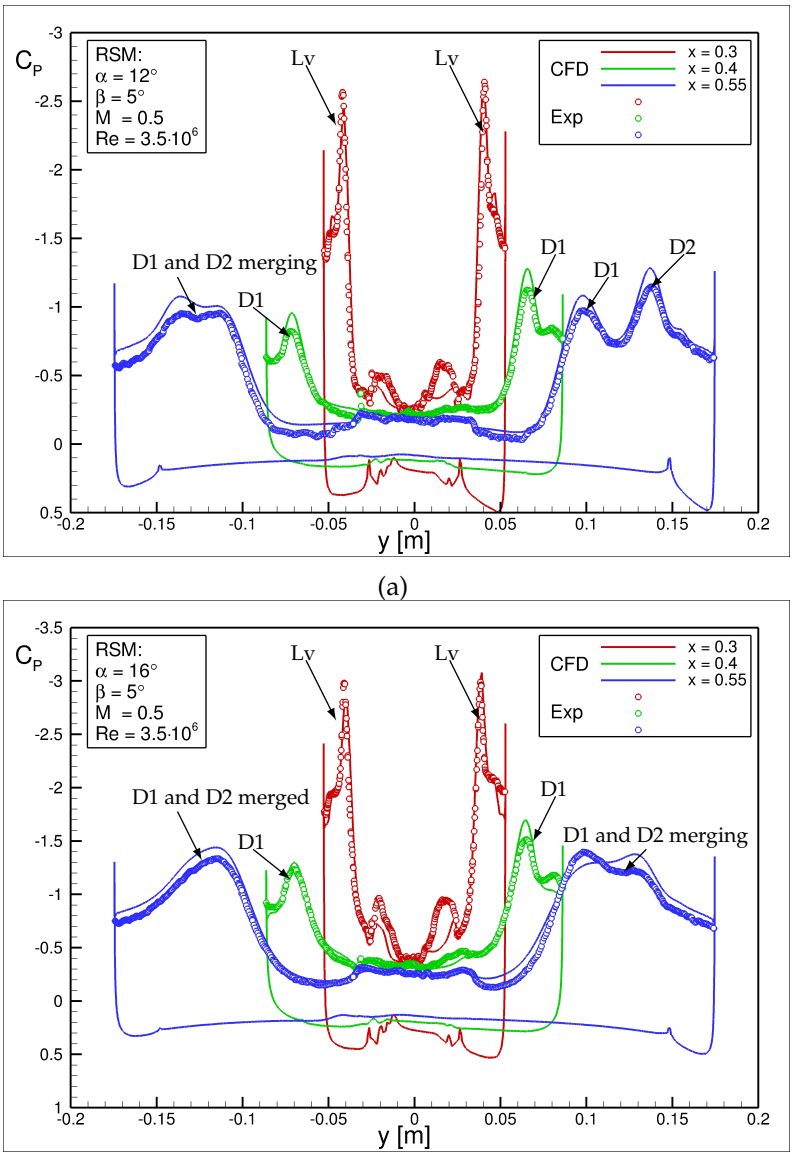



FIGURE 50: $C_P$ integral data resulting from RSM simulations for an AoA of (a) $\alpha = 12°$ and (b) $\alpha = 16°$ in comparison with PSP results.

For the symmetric and asymmetric solutions, the SA-neg model did not predict, in any case discussed in this thesis, the presence of a secondary vortex as the experimental results shows. So although qualitatively it doesn't seem extraordinarily different from the experimental data, when the quantities are compared it is clear that this difference is in fact significant. The k-$\omega$ turbulence models used present very good results for the symmetric on flow conditions, being predicted a similar accuracy for asymmetric simulations. Additionally, the k-$\omega$ TNT have a promising usage for higher AoA, since its results are quantitatively and qualitatively very close to the experiments. Finally, after all the comparisons done, the six equation model, RSM, is considered the best fit for the present thesis investigation.

# Chapter 8

# Conclusion and Further Work

This thesis scope was framed within a new AVT/STO Task Group, as DLR's Institute of Aerodynamics and Flow Technology found it feasible for this investigation to be taken course.

After better understanding of the flow physics complexity, natural to a fighter's in-flight conditions, the model, numerical methodology and grid generation processes were addressed. Experimental data was obtained by the wind tunnel tests performed in DLR/-DNW-TWG for symmetric and asymmetric on flow conditions.

The grid refinement showed no influence in results for an AoA range of $\alpha = 2°$ to $\alpha = 10°$ when applying the SA-neg turbulence model. It was concluded that for the remaining models this influence was the same.

A turbulence model sensitivity study was done to a symmetric on flow conditions for a range of $\alpha = 2°$ to $\alpha = 10°$ with a Reynolds number of $Re = 4.6 \cdot 10^6$. When comparing turbulence models, it was observed that for SA-neg presents the most distinct vortex footprint topology. This model also lacks prediction of certain vortex structures, as the secondary vortex. Quantitatively, SA-neg computes the most off pressure coefficient results when compared with results from other models. This is the case when comparing other aerodynamic quantities, even though drag is not influenced at all.

The Reynolds number effect was addressed since wind tunnel testing was done after this investigation had started and was necessary to diminish the Reynolds number from $Re = 4.6 \cdot 10^6$ to $Re = 3.5 \cdot 10^6$. The effect was evaluated for a single AoA of $\alpha = 10°$, for SA-neg turbulence model and for symmetric and asymmetric on flow conditions. Visually and quantitatively the effects were null, except for rolling moment and pitching moment in the asymmetric simulation. Even without this difference, the Reynolds to be used for subsequent simulations would be the same as in the wind tunnel tests to avoid further unnecessary differences.

Finally, a comparison with experimental data is performed in an attempt to validate different turbulence models. As expected, Spalart-Allmaras negative presents the worst results, being insufficient in predicting vortex footprint and aerodynamic quantities. On the other hand, k-$\omega$, k-$\omega$ TNT and RSM proved to be quite sufficient to be used when describing these complex flows. Additionally, RSM has the closest numerical solutions for the comparison taken place in this investigation.

Lastly, it is encouraged for future investigations to perform simulations with higher angles of attack for RSM. Its results are very close to experimental data for low to medium AoA range qualifying this turbulent model as very promising in obtaining an accurate prediction for vortex formation, vortex-vortex interaction and vortex breakdown for higher AoA. More investigations in this scope not only for RSM but as well for k-$\omega$ models can be also taken into account. These models, although having less accuracy than RSM, nevertheless have good results and so its development is of great benefit since it has an inherent lower computational cost than RSM.

# References


Anderson Jr., John D. (2007). *Fundamentals of Aerodynamics*. 4th Edition. McGraw-Hill, Inc.

Bertin, John J. and Russell M. Cummings (2009). *Aerodynamics for Engineers*. 5th Edition. Pearson Education, Inc.

CENTAUR (2018). *Centaur v12.0 Help*.

Cummings, Russell M and Andreas Schütte (2010). "An Integrated Computational/Experimental Approach to UCAV Stability & Control Estimation: Overview of NATO RTO AVT-161". In: *American Institute of Aeronautics and Astronautics Journal* July, pp. 1–23.

Cummings, Russell M. et al. (2015). *Applied Computational Aerodynamics*.

Délery, Jean M. (1992). "Physics of Vortical Flows". In: *Journal of Aircraft* 29.5.

DLR Institute of Aerodynamics and Flow Technology (2017b). *Tau-Code Technical Documentation*.

— (2017a). *TAU-Code User Guide*.

Drougge, G. (1988). "The international vortex flow experiment for computer code validation". In: *International Council of Aeronautical Sciences* 1, pp. XXXV–XLI.

Hitzel Stephan Maria & Boelens, Okko J. & van Rooj Michel & Hövelmann Andreas (2015). "Vortex Development on the AVT-183 Diamond Wing Configuration - Numerical and Experimental Findings". In:

Hitzel, Stephan (2017). "Sub- and Transonic Vortex Breakdown Flight Condition Simulations of the F-16XL Aircraft". In: *Journal of Aircraft* 54.2, pp. 428–443.

Hoeijmakers, H. W. M., W. Vaatstra, and N. G. Verhaagen (1983). "Vortex flow over delta and double delta wings". In: *American Institute of Aeronautics and Astronautics Journal* 20.9.

Hummel, Dietrich (1986). "On vortex formation over a slender wing at large angles of incidence". In: *High Angle of Attack Aerodynamics*.

Hummel, Dietrich, H. John, and W. Staudacher (1984). "Aerodynamic characteristics of wing body combinations at high angles of attack". In: *International Council of Aeronautical Sciences* 84.2.7.1.

Klein, Christian et al. (2005). "Application of pressure-sensitive paint for determination of the pressure field and calculation of the forces and moments of models in a wind tunnel". In: DOI: 10.1007/s00348-005-1010-8.

Kok, Johan C. (2000). "Resolving the Dependence on Freestream Values for the k-w turbulence model". In: 38.7. DOI: 10.2514/1.39026.

Lamar, John E. (1980). "Analysis and Design of Strake-Wing Configurations". In: *Journal of Aircraft* 17, pp. 20–27.

Lambourne, N. C. and D. W. Bryer (1961). *The Bursting of Leading Edge Vortices - Some Observations and Discussion of the Phenomenon*. Tech. rep. Ministry of Aviation.

Leveque, Randall J. (2004). *Finite Volume Method for Hyperbolic Problems*. Cambridge University Press, pp. 1–10, 64–85.

NATO Science and Technology Organization (2009b). *RTO-TR-AVT-080 - Vortex Breakdown over Slender Delta Wings*. Vol. 323. October. ISBN: 9789283700784.

— (2009a). *RTO-TR-AVT-113 - Understanding and Modeling Vortical Flows to Improve the Technology Readiness Level for Military Aircraft*. Vol. 323. October 2009. ISBN: 9789283700739.

Polhamus, Edward C (1969). "AlAA 61h Annual Meeting and Technical DisDlay". In: 69. DOI: 10.2514/6.1969-1133.

Pozrikidis, C. (1997). *Introduction to Theoretical and Computational Fluid Dynamcis*. Oxford University Press.

Rein, M. et al. (2018). *Transonic Wind Tunnel Measurements of Double and Triple Delta-Wing Configurations*. Tech. rep. DOI: DLR-IB-AS-GO-2018-79.

Schilichting, Hermann (1951). *Boundary-Layer Theory*. 7th edition. McGraw-Hill, Inc.

Schuette, Andreas, Dietrich Hummel, and Stephan M. Hitzel (2010). "Numerical and experimental analyses of the vortical flow around the SACCON configuration". In: *American Institute of Aeronautics and Astronautics* July, pp. 1–18. DOI: 10.2514/6.2010-4690. URL: http://arc.aiaa.org/doi/10.2514/6.2010-4690.

Schütte, Andreas, Dietrich Hummel, and Stephan M. Hitzel (2010). "Numerical and experimental analyses of the vortical flow around the SACCON configuration". In: *American Institute of Aeronautics and Astronautics*.

Spalart, P. R. and S. R. Allmaras (1992). "A One-Equation Turbulence Model for Aerodynamics Flows". In: *American Institute of Aeronautics and Astronautics*.

Spalart, P. R., S. R. Allmaras, and F. T. Johnson (2012). "Modifications and Clarifications for the Implementation of the Spalart-Allmaras Turbulence Model". In:

Thakur, S. and W. Shyy (1999). "Reynolds Stress Models for Flows in Complex Geometries: Review and Application". In: *American Institute of Aeronautics and Astronautics*.

Werlé, H. (1984). *On Vortex Bursting*. Tech. rep.

Wilcox, D. C. (2008). "Formulation of the k-$\omega$ Turbulence Model Revisited". In: *American Institute of Aeronautics and Astronautics* 46.11, pp. 2823–2838. DOI: 10.2514/1.36541.

Yorita, Daisuke, Ulrich Henne, and Christian Klein (2017). "Improvement of Lifetime-based PSP Technique for Industrial Wind Tunnel Tests". In: *American Institute of Aeronautics and Astronautics* January, pp. 1–13. DOI: 10.2514/6.2017-0703.

# List of Figures


1 From the project **F**uture **C**ombat **A**ir **S**ystem (FCAS). Courtesy of Airbus. . 2

2 Attachment (a) or separation (b) line schematic. Courtesy of ONERA. . . . 7
3 Two dimensional sketch of (a) two close together vortices and (b) a saddle point, where the lines represent flow mass. . . . . 8
4 Lift coefficient and angle of attack plot comparing a regular swept wing (red) and a delta wing (green). Copyright Dr.-Ing. Andreas Schütte. . . . . 9
5 Flow topology scheme over a delta wing (Anderson Jr., 2007). . . . . 9
6 Vortex topology with the pressure distribution along the wing (Hummel, 1986). . . . . 10
7 Total pressure distribution in the upper surface for 2° (a) and 16° (b) angle of attack. . . . . 11
8 Streamlines plot over a straked double delta for 2° (a) and 16° (b) angle of attack. . . . . 12
9 Pressure distribution over a straked double delta for 2° (a) and 16° (b) angle of attack. . . . . 13
10 Pressure distribution along with skin friction lines over a straked double delta for 2° (a) and 16° (b) angle of attack. . . . . 13

11 Model geometry without the representation of the sting and with reference lengths displayed. . . . . 15
12 Entire model representation, namely the sting and the sting support. . . . 16
13 Entire model representation, in lateral view. . . . . 16
14 Convention of moments on a generic aircraft, by (Bertin and Cummings, 2009). . . . . 17

15 Convergence history of an steady simulation. . . . . 25
16 Convergence history of an unsteady simulation. . . . . 26

17 Nose fuselage detail of the medium refined grid. . . . . 27
18 Three dimensional view of the whole model with the three generated grids. 29
19 $y = const$ at $y = 0.15m$ from the nose figure for prismatic layer visualization. 30
20 Leading edge number of surface elements comparison between grids. . . 30
21 Velocity vectors profile for medium refined grid. . . . . 31
22 $y^+$ distribution for each generated grid . . . . . 32

23 Photography of the entire model, the straked double delta with the sting and sting support. Courtesy of DLR/DNW-TWG. . . . . 33
24 TWG model. Courtesy of DLR/DNW-TWG. . . . . 34
25 Photography of the model close-up to see the tripping system on the nose. Courtesy of DLR/DNW-TWG. . . . . 35
26 Representation of the pressure distribution on the upper surface of the model using PSP technique. . . . . 35

27 $C_P$ surface distribution for an AoA $\alpha = 6°$ of (a) coarse, (b) medium and (c) fine grid. . . . . 37
28 Streamlines on the wing upper surface for an AoA $\alpha = 10°$ for (a) coarse, (b) medium and (c) fine grid. . . . . 38
29 Comparison of $C_L$, $C_D$ and $C_m$ values between the three generated grid for multiple AoA. . . . . 39
30 $C_P$ surface distribution with skin friction lines for an AoA $\alpha = 8°$ with (a) SA-neg, (b) k-$\omega$, (c) k-$\omega$ TNT and (d) RSM turbulence model. . . . . 41
31 Total pressure projected with velocity vectors in a perpendicular view along the vortex core for k-$\omega$ TNT turbulence model at Delta 1 with an AoA of $\alpha = 8°$. . . . . 42
32 Hand made sketch representing a simplified topology of the secondary vortex interaction with the primary one as seen in the latter Figure. . . . . 42
33 Comparison of $C_L$, $C_D$ and $C_m$ values between the four turbulence models used for the multiple AoA simulated. . . . . 43
34 Comparison of $C_P$ values between the two Reynolds number used for (a) symmetric and (b) asymmetric on flow conditions. . . . . 44
35 Comparison of $C_L$, $C_D$ and $C_m$ values between the different Reynolds number used in symmetric on flow conditions. . . . . 45
36 Comparison of $C_L$, $C_D$ and $C_m$ values between the different Reynolds number used in asymmetric on flow conditions. . . . . 45
37 Comparison of $C_L$, $C_D$ and $C_m$ values between SA-neg turbulence model and experimental data for the multiple AoA simulated and tested. . . . . 46
38 Comparison of $C_L$, $C_D$ and $C_m$ values between k-$\omega$ turbulence model and experimental data for the multiple AoA simulated and tested. . . . . 46
39 Comparison of $C_L$, $C_D$ and $C_m$ values between k-$\omega$ TNT turbulence model and experimental data for the multiple AoA simulated and tested. . . . . 47
40 Comparison of $C_L$, $C_D$ and $C_m$ values between RSM turbulence model and experimental data for the multiple AoA simulated and tested. . . . . 47
41 $C_P$ surface distribution resulting from RSM simulations for an AoA of $\alpha = 16°$ in comparison with PSP results. . . . . 48
42 $C_P$ quantities resulting from SA-neg simulations for an AoA of (a) $\alpha = 10°$, (b) $\alpha = 12°$ and (c) $\alpha = 16°$ in comparison with PSP results. . . . . 49
43 $C_P$ quantities resulting from k-$\omega$ simulations for an AoA of (a) $\alpha = 10°$ and (b) $\alpha = 12°$ in comparison with PSP results. . . . . 50
44 $C_P$ quantities resulting from k-$\omega$ TNT simulations for an AoA of $\alpha = 10°$ in comparison with PSP results. . . . . 51
45 $C_P$ quantities resulting from RSM simulations for an AoA of (a) $\alpha = 10°$ and (b) $\alpha = 16°$ in comparison with PSP results. . . . . 52
46 Comparison of $C_L$, $C_D$ and $C_m$ values between SA-neg turbulence model with experimental data for the multiple AoA simulated and tested. . . . . 53
47 Comparison of $C_L$, $C_D$ and $C_m$ values between RSM turbulence model with experimental data for the multiple AoA simulated and tested. . . . . 53
48 $C_P$ surface distribution resulting from (a) SA-neg and (b) RSM simulations for an AoA of $\alpha = 16°$ in comparison with PSP results. . . . . 55
49 $C_P$ integral data resulting from SA-neg simulations for an AoA of (a) $\alpha = 12°$ and (b) $\alpha = 16°$ in comparison with PSP results. . . . . 56
50 $C_P$ integral data resulting from RSM simulations for an AoA of (a) $\alpha = 12°$ and (b) $\alpha = 16°$ in comparison with PSP results. . . . . 57

51 $C_P$ surface distribution for an AoA $\alpha = 10°$ of (a) coarse, (b) medium and (c) fine grid. . . . 70
52 $C_P$ surface distribution and skin friction lines for an AoA $\alpha = 6°$ for the (a) coarse, (b) medium and (c) fine grid. . . . 71
53 $C_P$ surface distribution with skin friction lines for an AoA $\alpha = 10°$ with (a) coarse, (b) medium and (c) fine grid. . . . 72
54 Total pressure distribution on the wing upper surface for an AoA $\alpha = 6°$ for (a) coarse, (b) medium and (c) fine grid. . . . 73
55 Total pressure distribution on the wing upper surface for an AoA $\alpha = 10°$ for (a) coarse, (b) medium and (c) fine grid. . . . 74
56 Streamlines on the wing upper surface for an AoA $\alpha = 6°$ for (a) coarse, (b) medium and (c) fine grid. . . . 75
57 Comparison of $C_P$ values between the three generated grid for an AoA of $\alpha = 6°$ a $x = constant$ at 2/3 of LEVCON. . . . 76
58 Comparison of $C_P$ values between the three generated grid for an AoA of $\alpha = 6°$ a $x = constant$ at 2/3 of Delta 1. . . . 76
59 Comparison of $C_P$ values between the three generated grid for an AoA of $\alpha = 6°$ a $x = constantat$ 2/3 of Delta 2. . . . 77
60 Comparison of $C_P$ values between the three generated grid for an AoA of $\alpha = 10°$ a $x = constant$ at 2/3 of LEVCON. . . . 77
61 Comparison of $C_P$ values between the three generated grid for an AoA of $\alpha = 10°$ a $x = constant$ at 2/3 of Delta 1. . . . 78
62 Comparison of $C_P$ values between the three generated grid for an AoA of $\alpha = 10°$ a $x = constant$ at 2/3 of Delta 2. . . . 78
63 $C_P$ surface distribution at an AoA $\alpha = 8°$ for (a) SA-neg, (b) k-$\omega$, (c) k-$\omega$ TNT and (d) RSM turbulence model. . . . 79
64 Total pressure distribution for an AoA $\alpha = 8°$ for (a) SA-neg, (b) k-$\omega$, (c) k-$\omega$ TNT and (d) RSM turbulence model. . . . 80
65 Total pressure projected with velocity vectors in a perpendicular view along the vortex core for k-$\omega$ TNT turbulence model at an AoA $\alpha = 8°$ on Delta 2. See Figure 3a. . . . 81
66 Comparison of $C_P$ values between the four turbulence models for an AoA of $\alpha = 8°$ a $x = constant$ at 2/3 of the LEVCON. . . . 82
67 Comparison of $C_P$ values between the four turbulence models used for an AoA of $\alpha = 8°$ at a $x = constant$ at 2/3 of Delta 1. . . . 82
68 Comparison of $C_P$ values between the four turbulence models for an AoA of $\alpha = 8°$ a $x = constant$ at 2/3 of Delta 2. . . . 83
69 $C_P$ surface distribution for an AoA $\alpha = 10°$ for a symmetric on flow condition with a Reynolds number of (a) $Re = 4.6 \cdot 10^6$ and (b) $Re = 3.5 \cdot 10^6$. . . 84
70 $C_P$ surface distribution for an AoA $\alpha = 10°$ for an asymmetric on flow condition with a Reynolds number of (a) $Re = 4.6 \cdot 10^6$ and (b) $Re = 3.5 \cdot 10^6$. 85
71 $C_P$ surface distribution with skin friction lines for an AoA $\alpha = 10°$ for a symmetric on flow condition with a Reynolds number of (a) $Re = 4.6 \cdot 10^6$ and (b) $Re = 3.5 \cdot 10^6$. . . . 86
72 $C_P$ surface distribution with skin friction lines for an AoA $\alpha = 10°$ for an asymmetric on flow condition with a Reynolds number of (a) $Re = 4.6 \cdot 10^6$ and (b) $Re = 3.5 \cdot 10^6$. . . . 87
73 $C_P$ surface distribution resulting from SA-neg simulations for an AoA of (a) $\alpha = 10°$ and (b) $\alpha = 16°$ in comparison with PSP results. . . . 88
74 $C_P$ surface distribution resulting from k-$\omega$ simulations for an AoA of (a) $\alpha = 10°$ and (b) $\alpha = 12°$ in comparison with PSP results. . . . 89

75 $C_P$ surface distribution resulting from k-$\omega$ TNT simulations for an AoA of $\alpha = 10°$ in comparison with PSP results. . . . . 89
76 $C_P$ surface distribution resulting from RSM simulations for an AoA of (a) $\alpha = 10°$ and (b) $\alpha = 16°$ in comparison with PSP results. . . . . 90
77 $C_P$ surface distribution resulting from (a) SA-neg and (b) RSM simulations for an AoA of $\alpha = 12°$ in comparison with PSP results. . . . . 91

# List of Tables

1 Grid sensitivity study. . . . . 23
2 Turbulence model sensitivity study. . . . . 23
3 Reynolds effects study. . . . . 24
4 Experimental comparison study. . . . . 24

5 Parameters changed during the grid sensitivity study. . . . . 28

# Appendix A

# Results

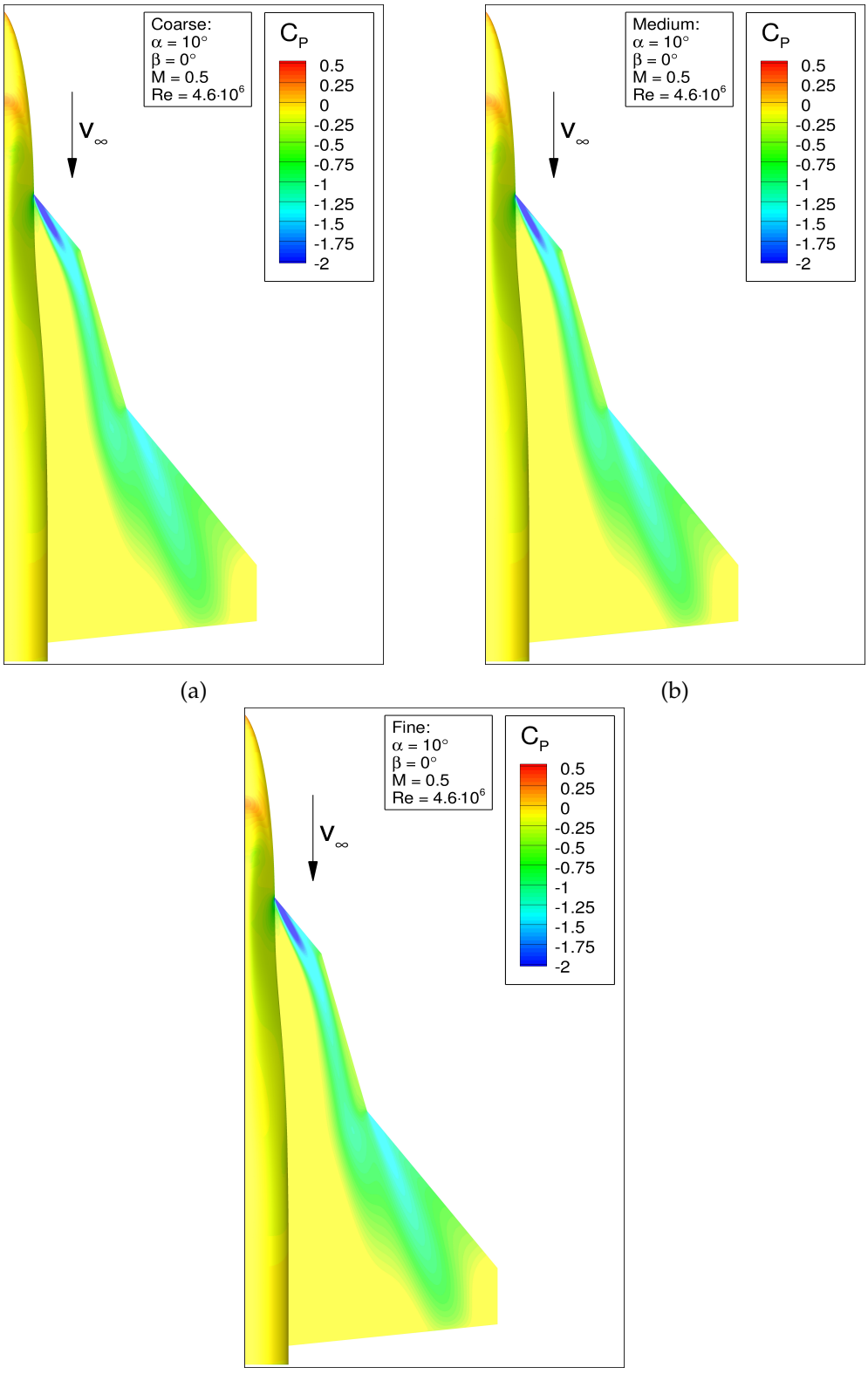



FIGURE 51: $C_P$ surface distribution for an AoA $\alpha = 10°$ of (a) coarse, (b) medium and (c) fine grid.

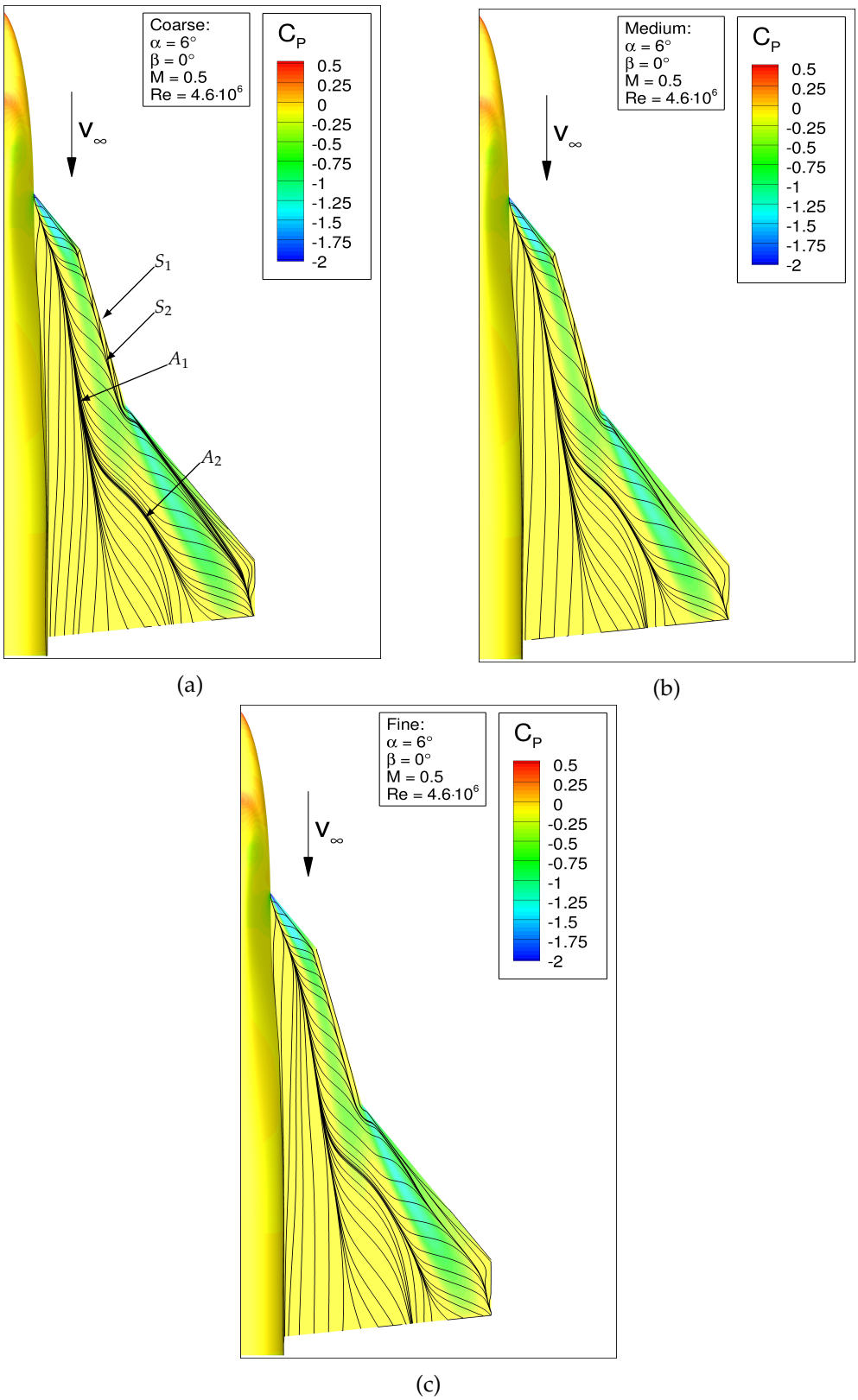



FIGURE 52: $C_P$ surface distribution and skin friction lines for an AoA $\alpha = 6°$ for the (a) coarse, (b) medium and (c) fine grid.

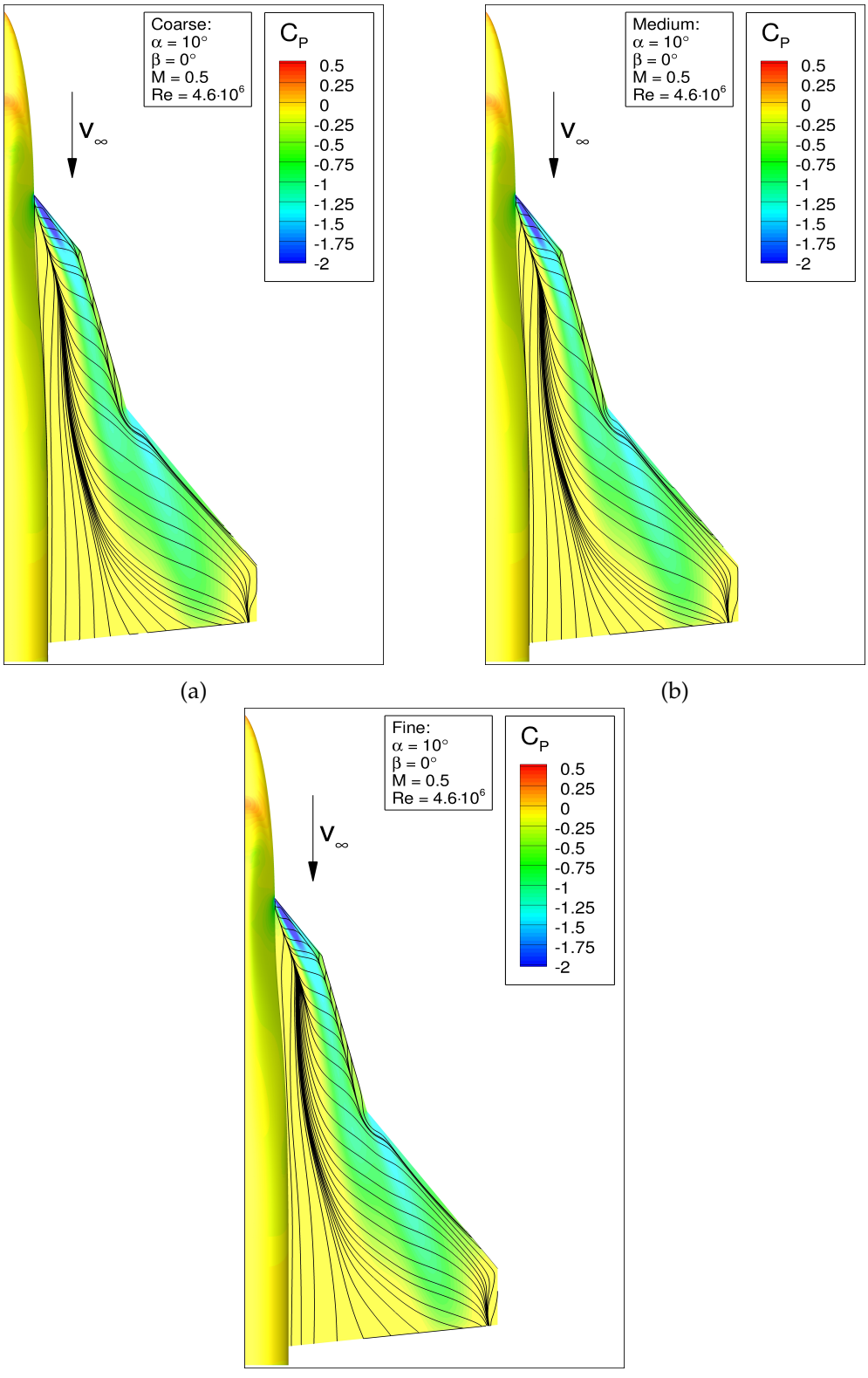



FIGURE 53: $C_P$ surface distribution with skin friction lines for an AoA $\alpha = 10°$ with (a) coarse, (b) medium and (c) fine grid.

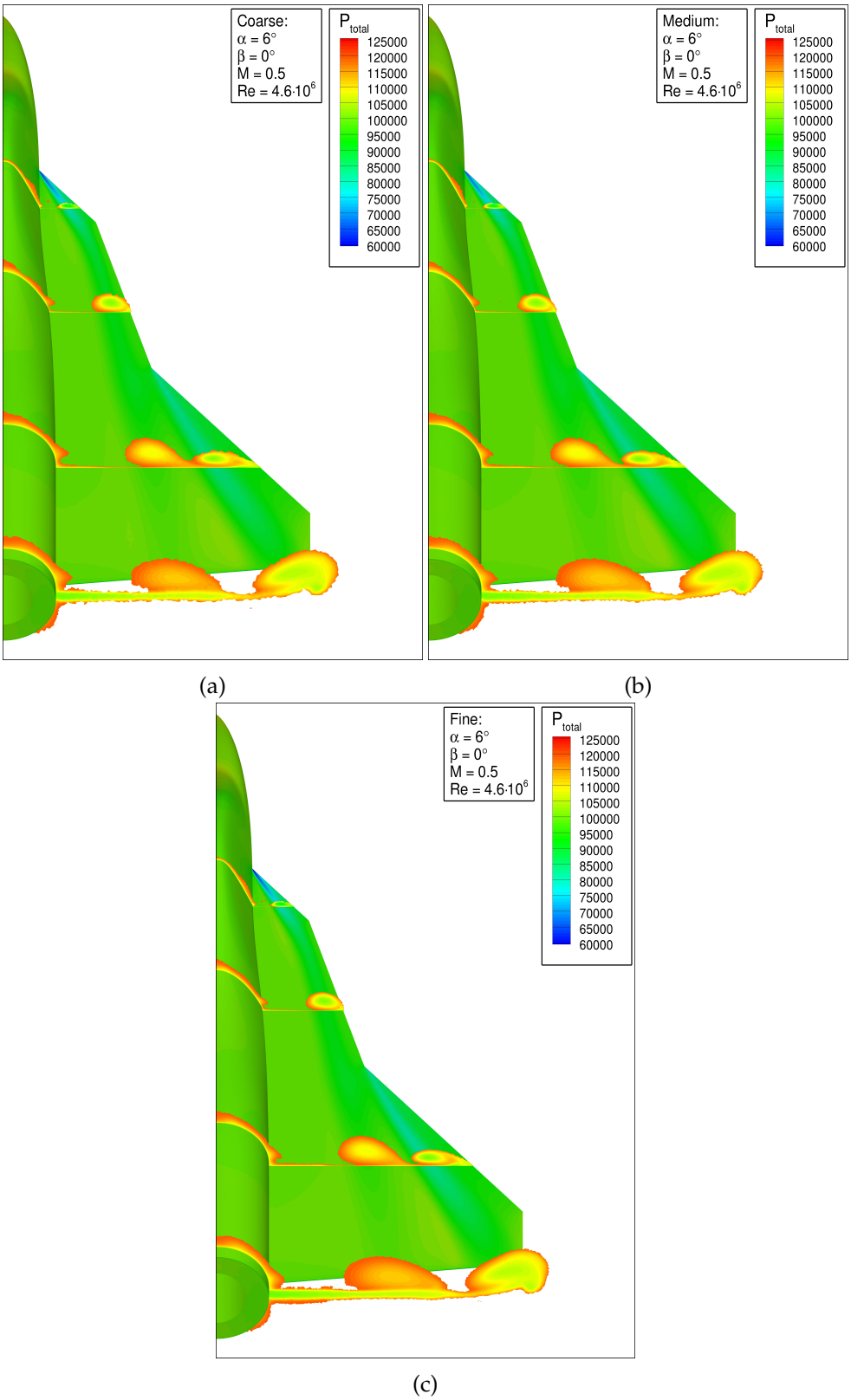



FIGURE 54: Total pressure distribution on the wing upper surface for an AoA $\alpha = 6°$ for (a) coarse, (b) medium and (c) fine grid.

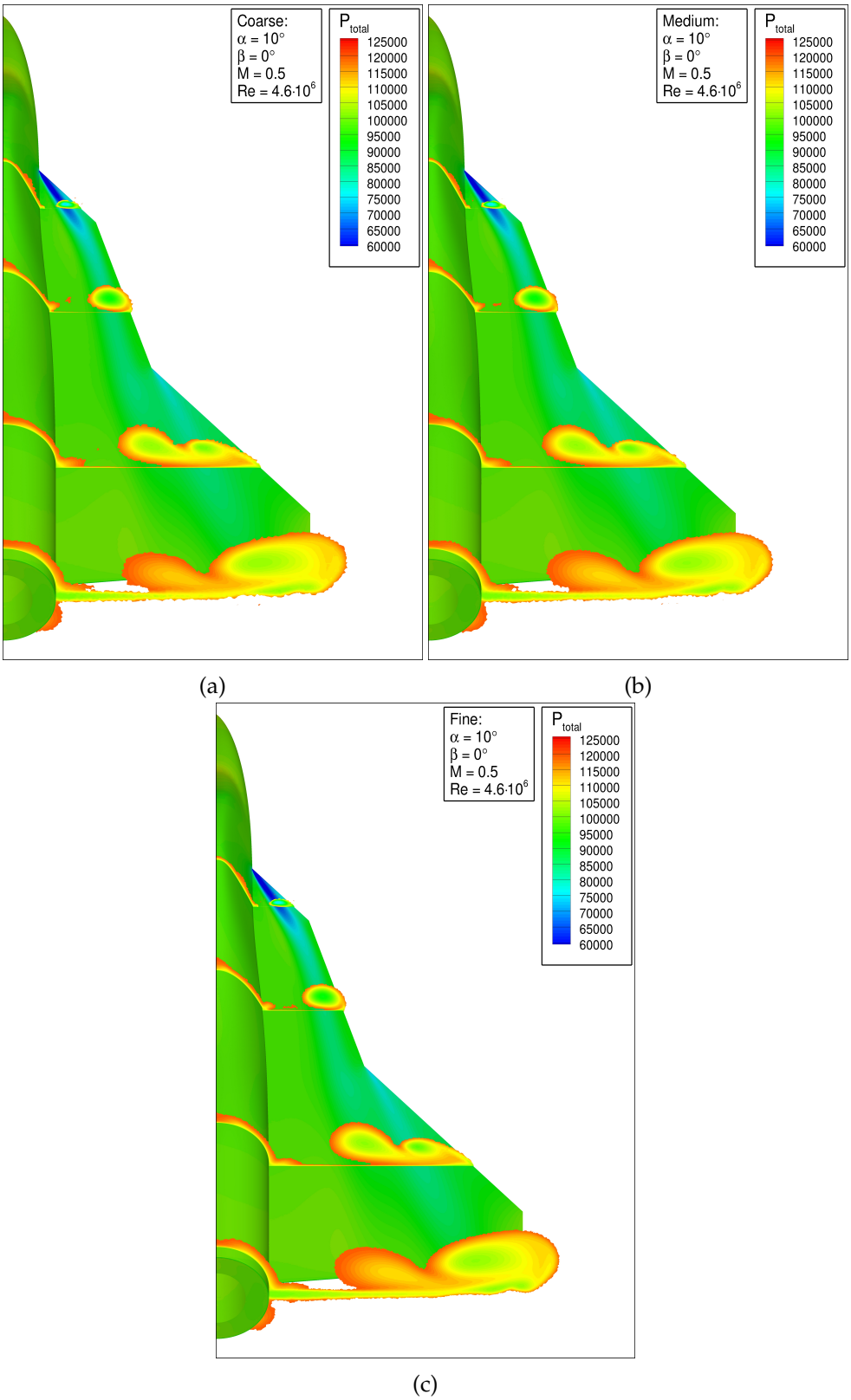



FIGURE 55: Total pressure distribution on the wing upper surface for an AoA $\alpha = 10°$ for (a) coarse, (b) medium and (c) fine grid.

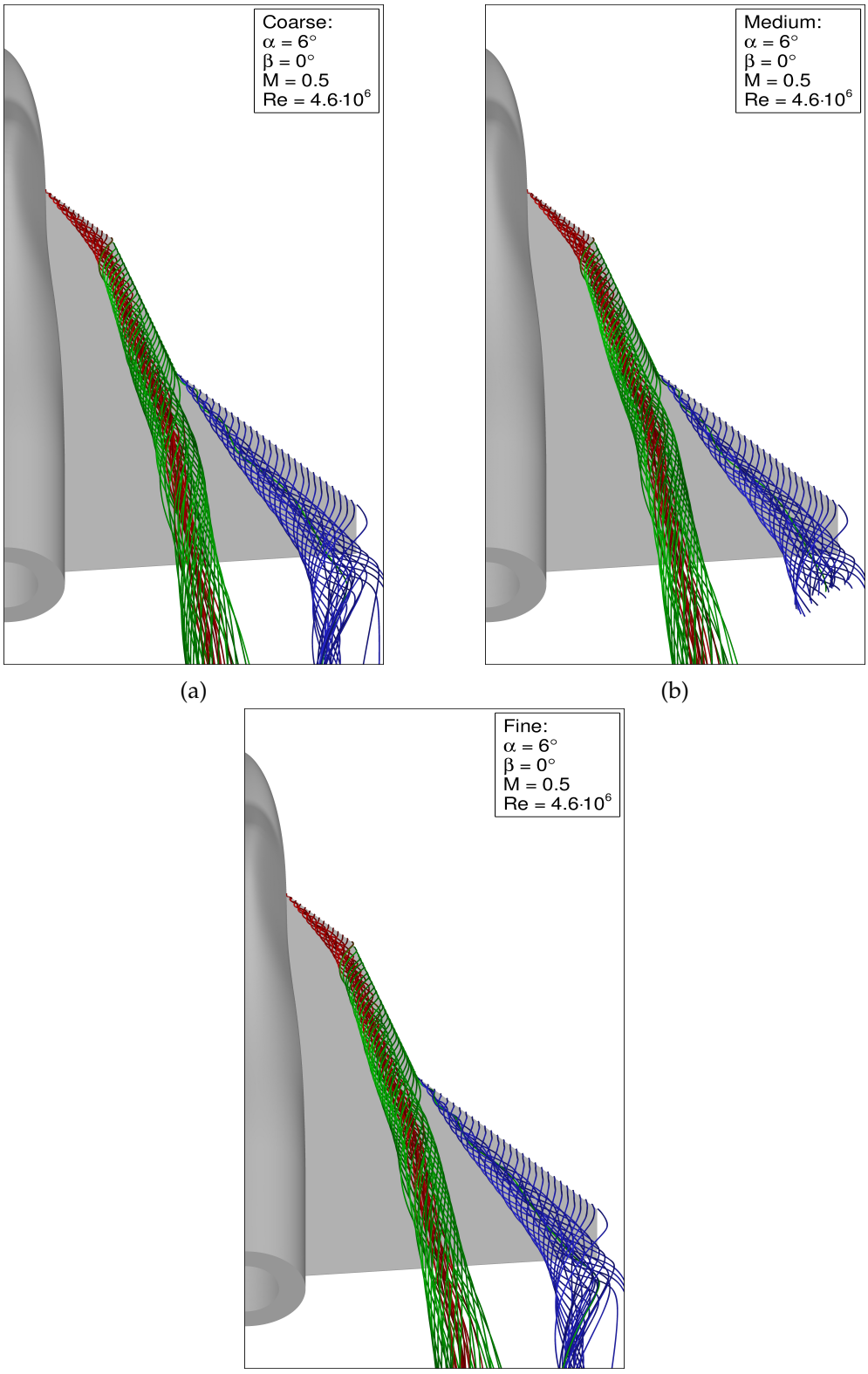



FIGURE 56: Streamlines on the wing upper surface for an AoA $\alpha = 6°$ for (a) coarse, (b) medium and (c) fine grid.

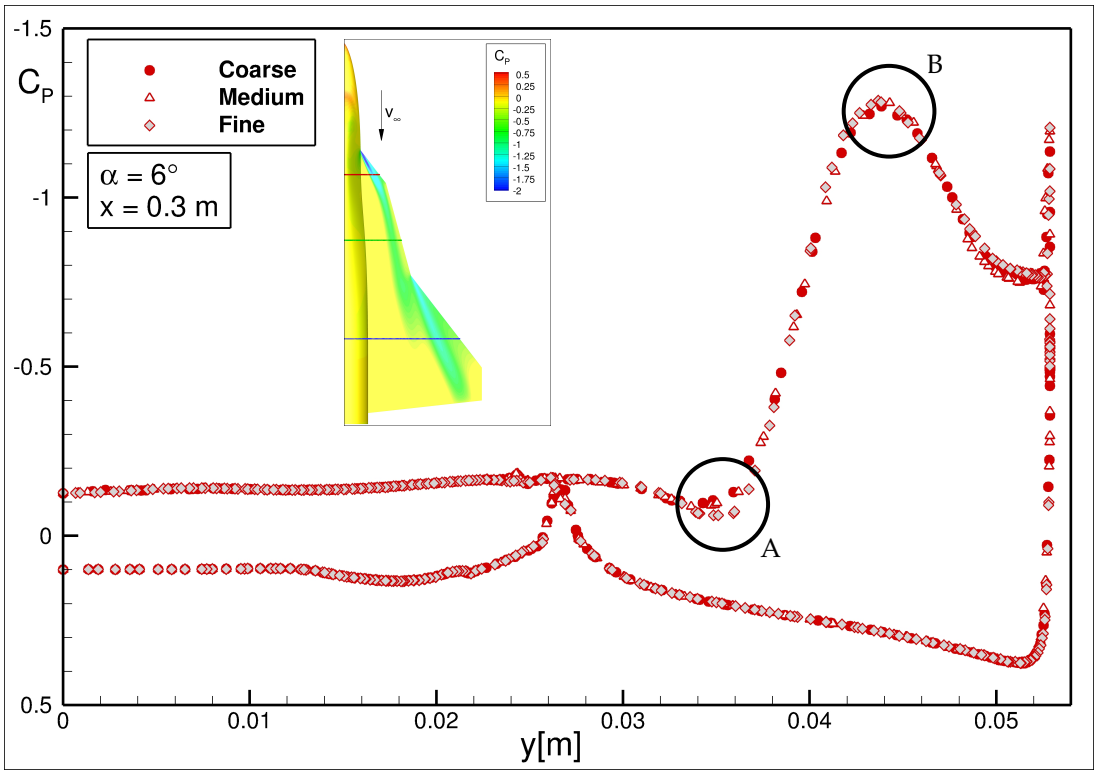



FIGURE 57: Comparison of $C_P$ values between the three generated grid for an AoA of $\alpha = 6°$ a $x = constant$ at 2/3 of LEVCON.

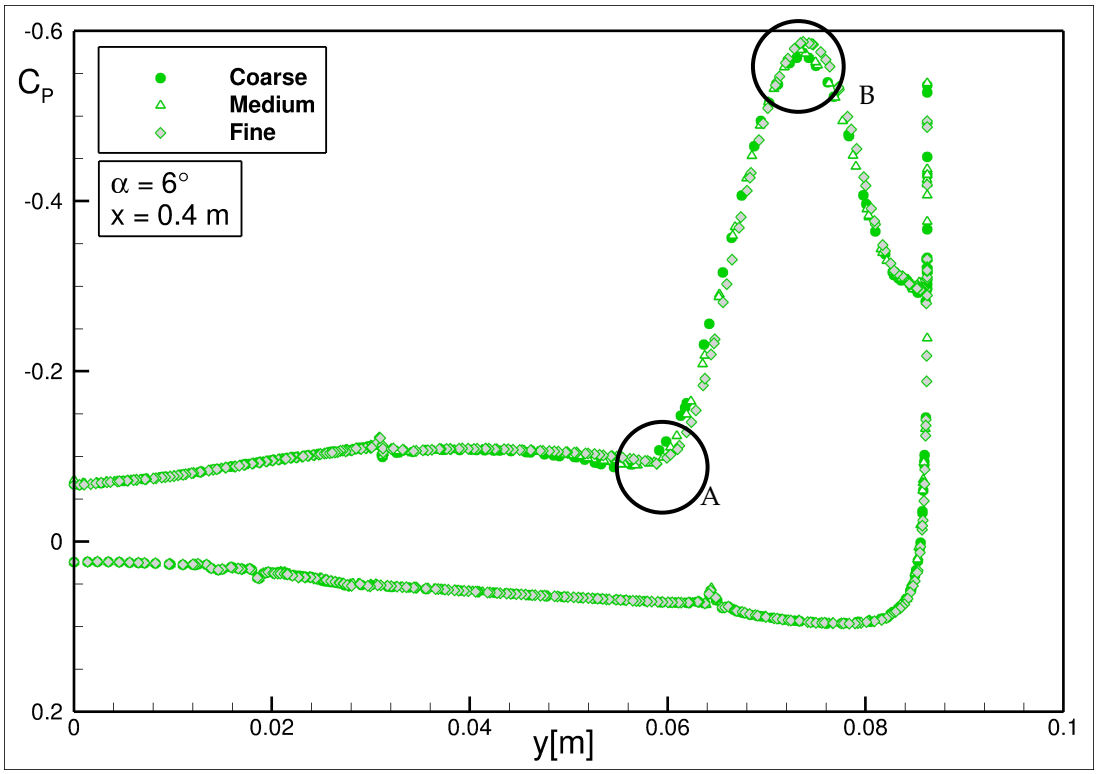



FIGURE 58: Comparison of $C_P$ values between the three generated grid for an AoA of $\alpha = 6°$ a $x = constant$ at 2/3 of Delta 1.

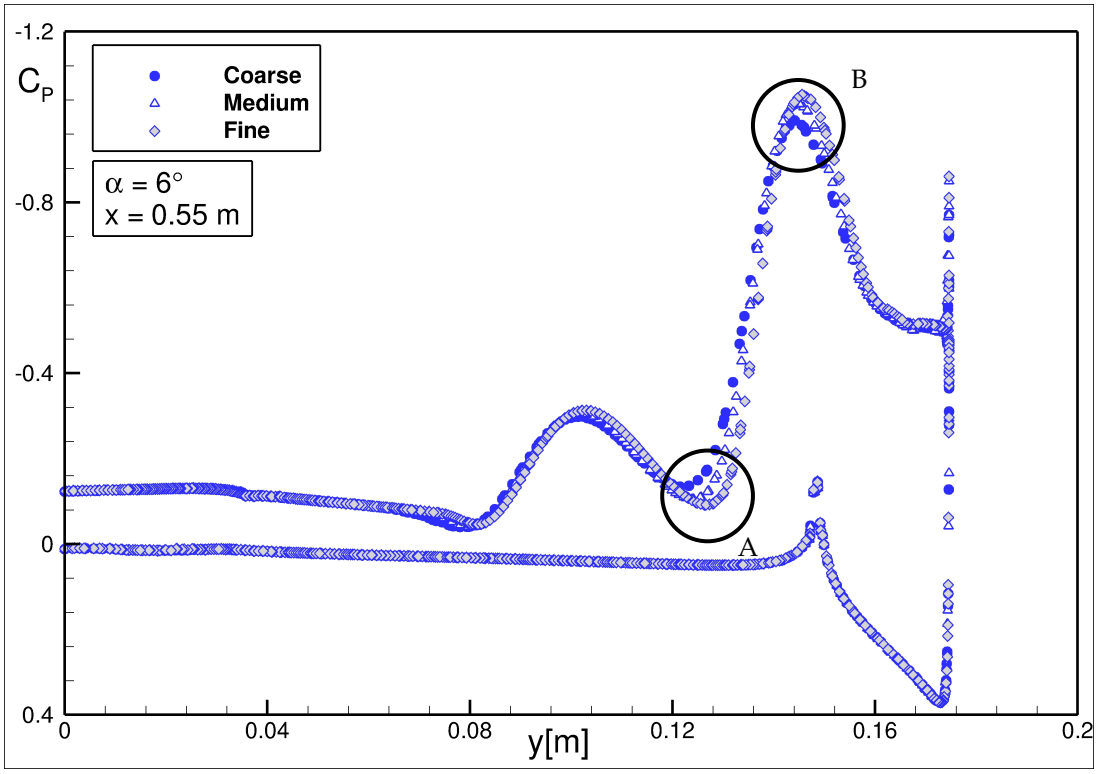



FIGURE 59: Comparison of $C_P$ values between the three generated grid for an AoA of $\alpha = 6°$ a $x = constantat$ 2/3 of Delta 2.

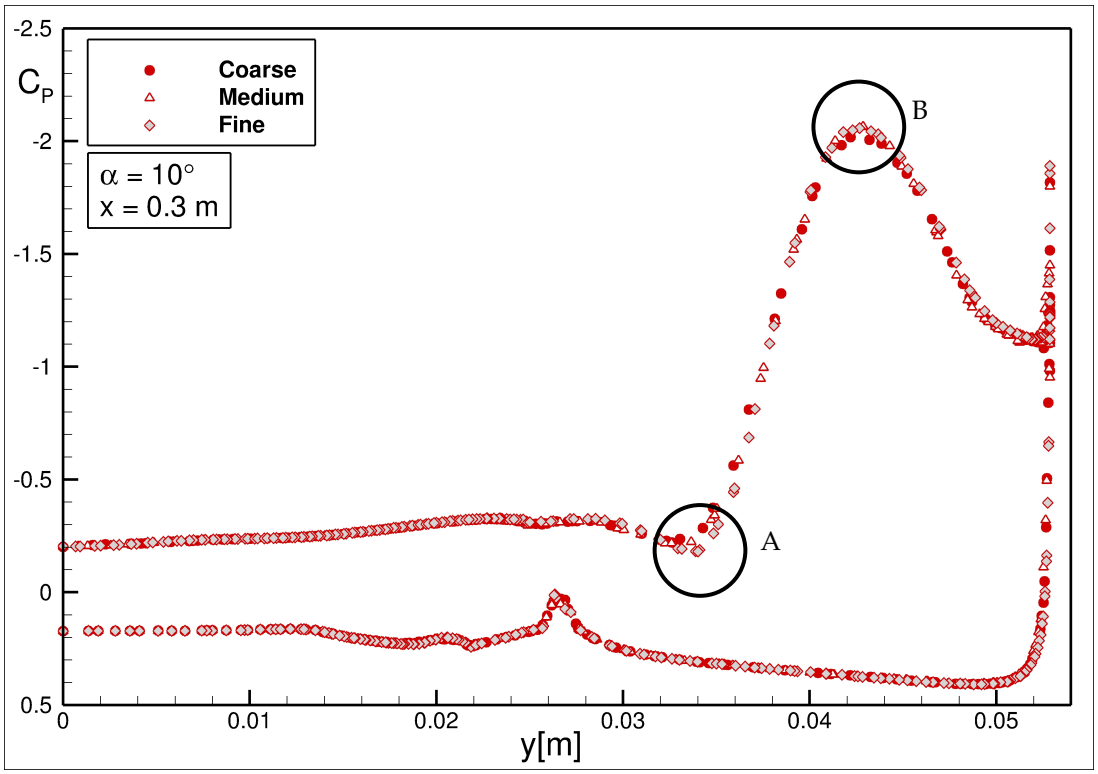



FIGURE 60: Comparison of $C_P$ values between the three generated grid for an AoA of $\alpha = 10°$ a $x = constant$ at 2/3 of LEVCON.

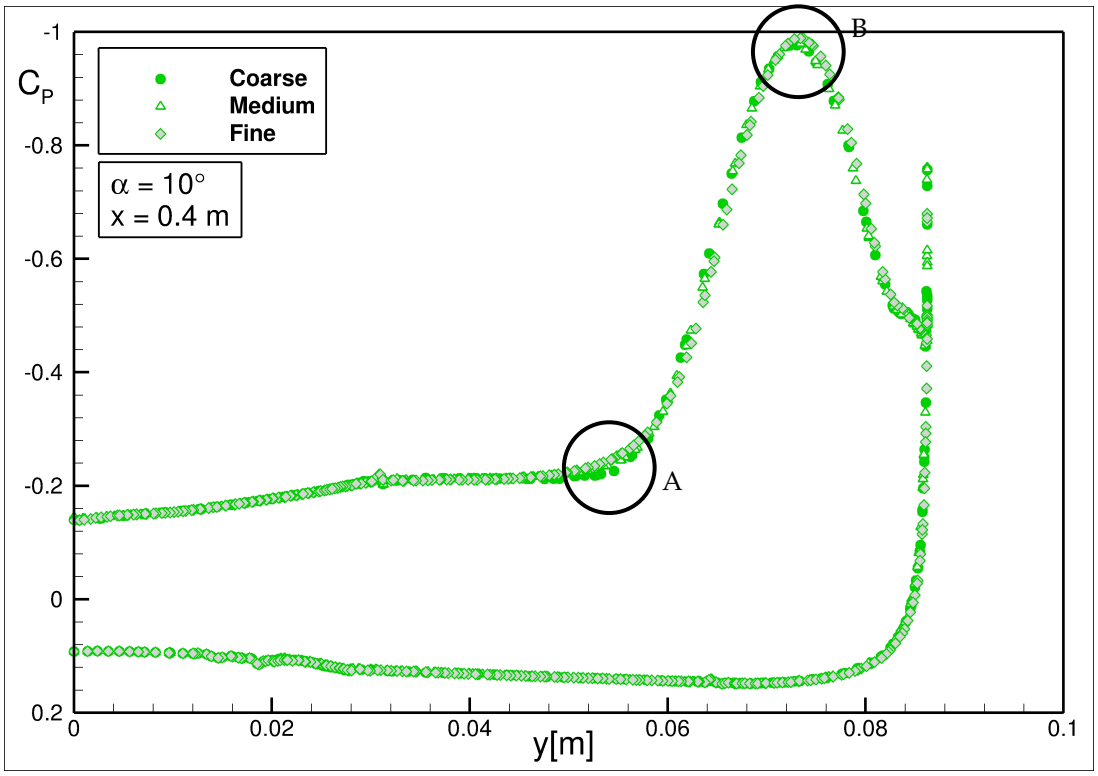



FIGURE 61: Comparison of $C_P$ values between the three generated grid for an AoA of $\alpha = 10°$ a $x = constant$ at 2/3 of Delta 1.

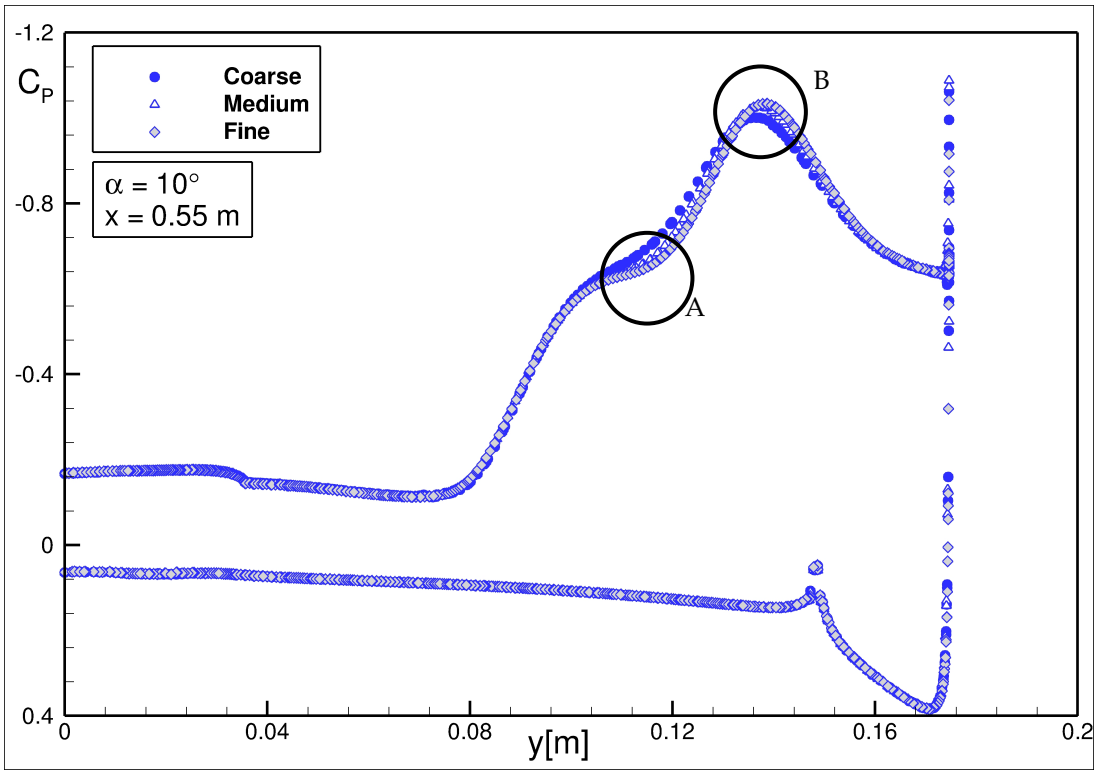



FIGURE 62: Comparison of $C_P$ values between the three generated grid for an AoA of $\alpha = 10°$ a $x = constant$ at 2/3 of Delta 2.

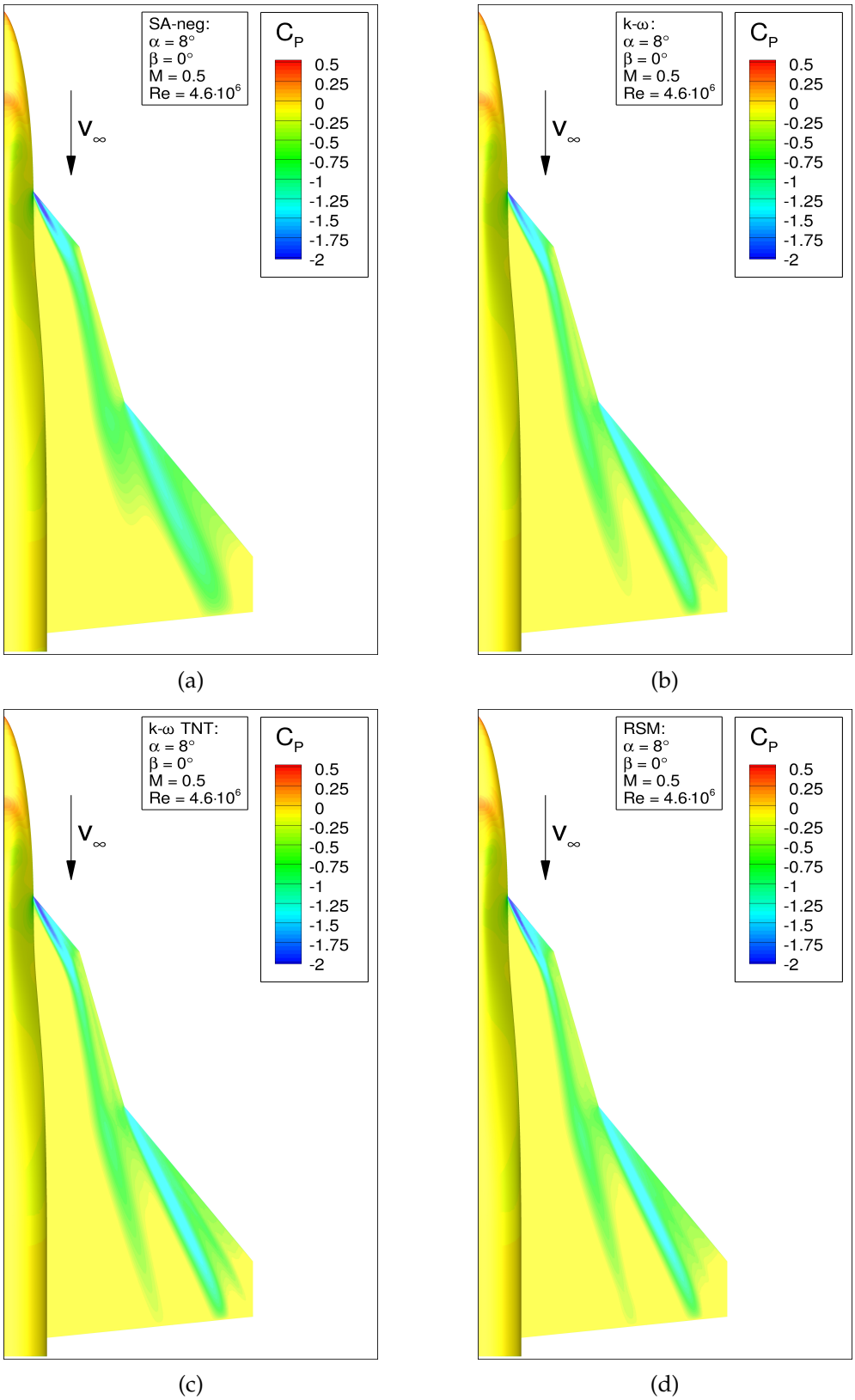



FIGURE 63: $C_P$ surface distribution at an AoA $\alpha = 8°$ for (a) SA-neg, (b) k-$\omega$, (c) k-$\omega$ TNT and (d) RSM turbulence model.

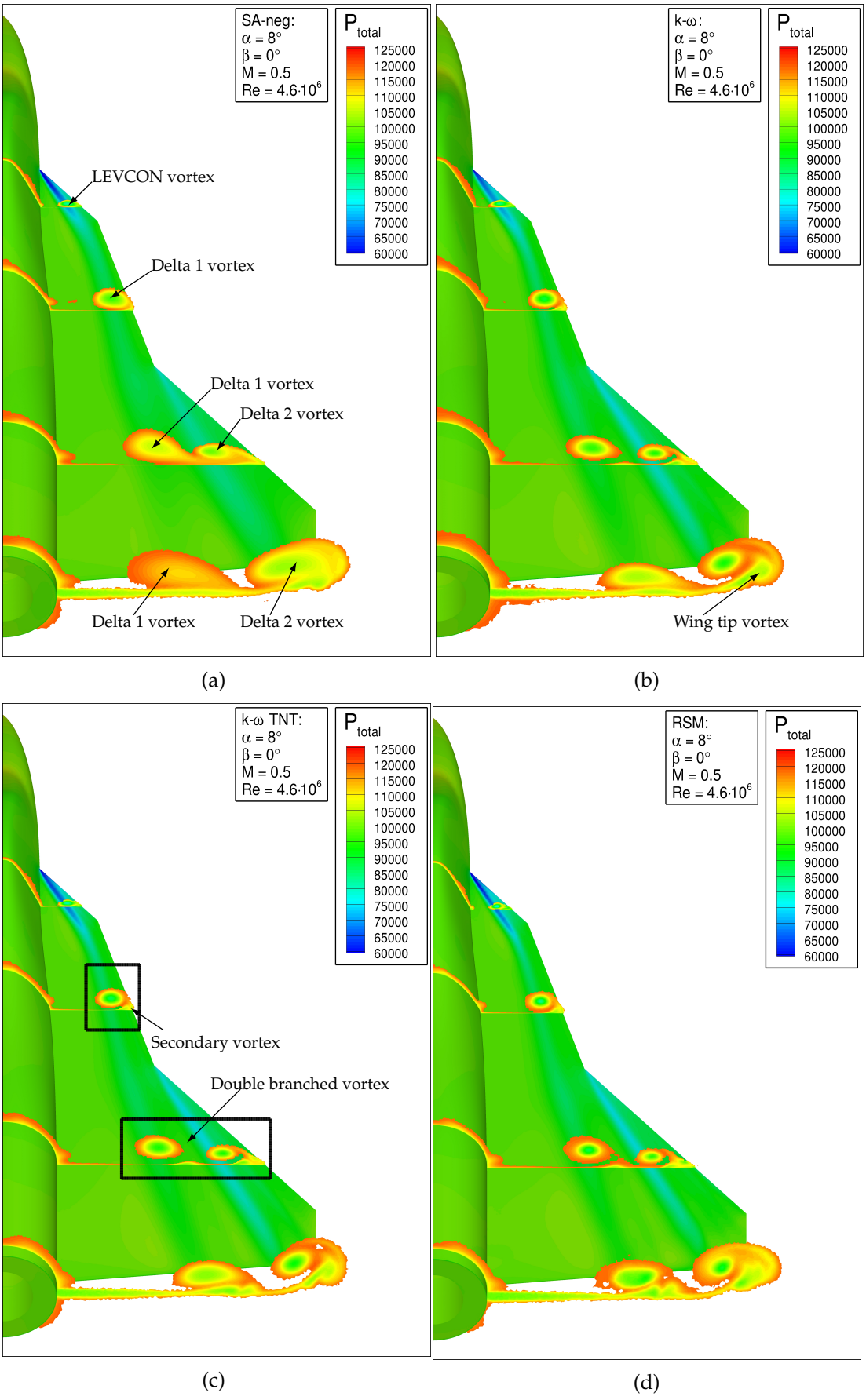



FIGURE 64: Total pressure distribution for an AoA $\alpha = 8°$ for (a) SA-neg, (b) k-$\omega$, (c) k-$\omega$ TNT and (d) RSM turbulence model.

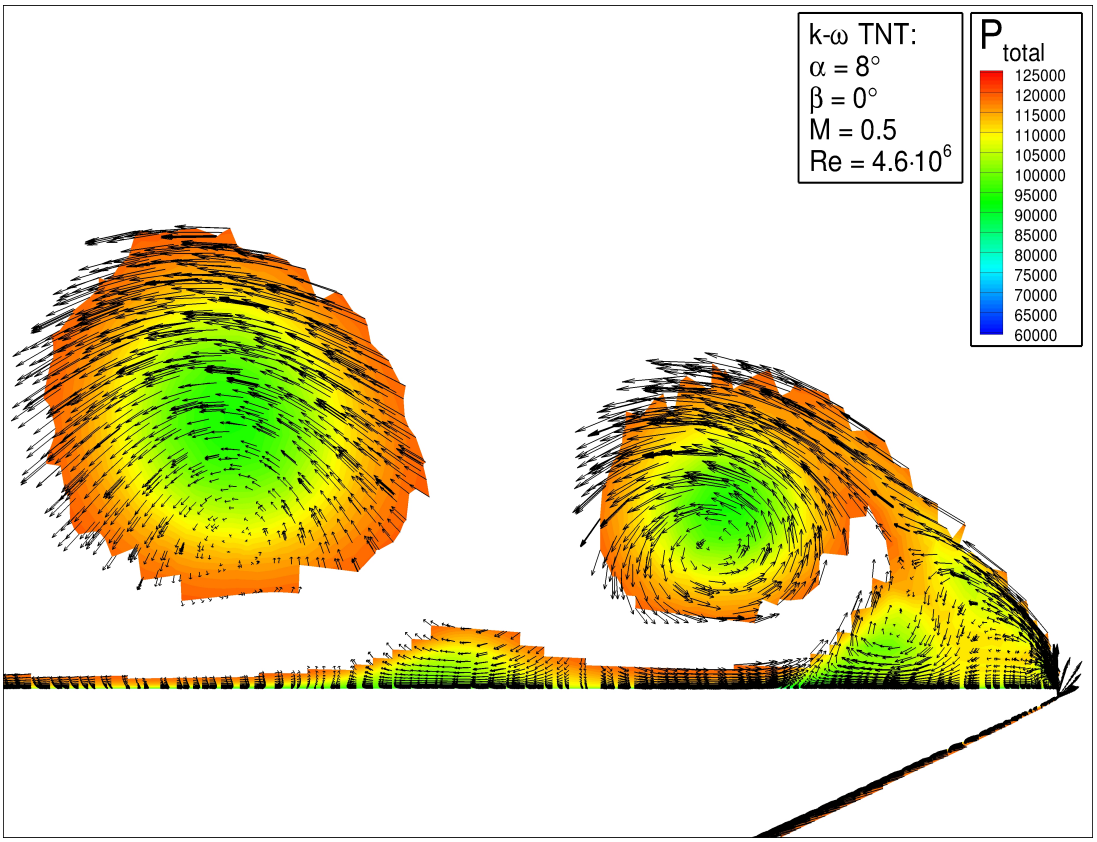



FIGURE 65: Total pressure projected with velocity vectors in a perpendicular view along the vortex core for k-$\omega$ TNT turbulence model at an AoA $\alpha = 8°$ on Delta 2. See Figure 3a.

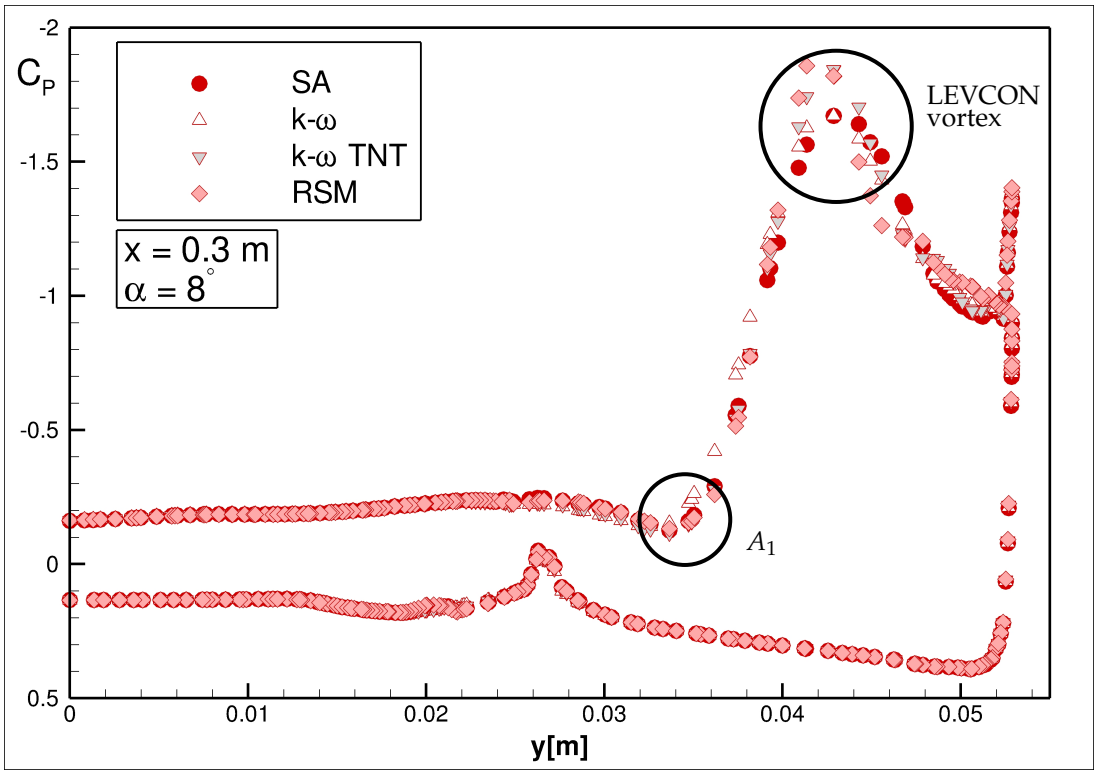



FIGURE 66: Comparison of $C_P$ values between the four turbulence models for an AoA of $\alpha = 8°$ a $x = constant$ at 2/3 of the LEVCON.

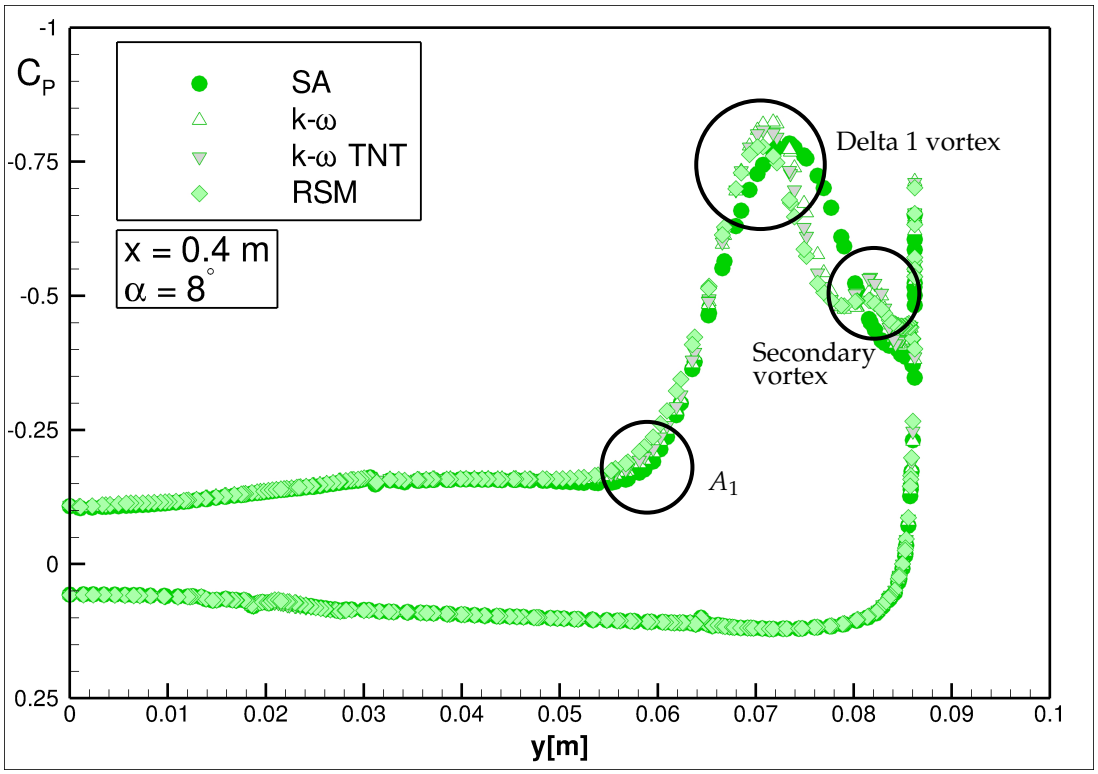



FIGURE 67: Comparison of $C_P$ values between the four turbulence models used for an AoA of $\alpha = 8°$ at a $x = constant$ at 2/3 of Delta 1.

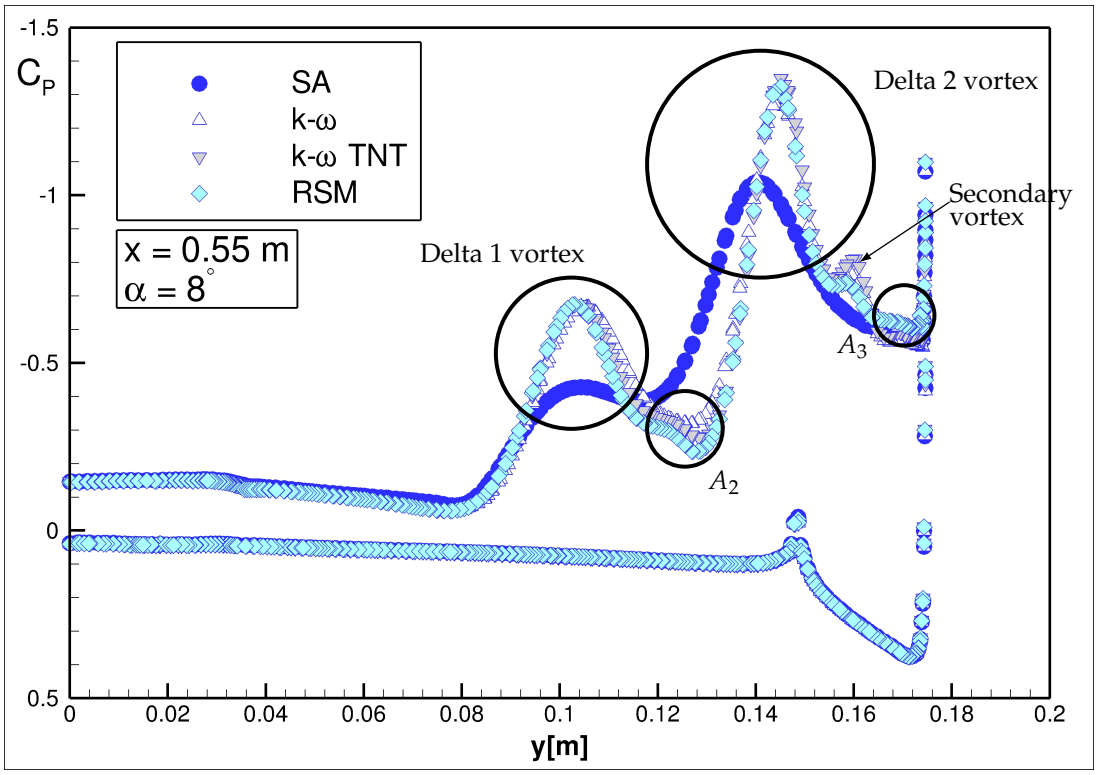
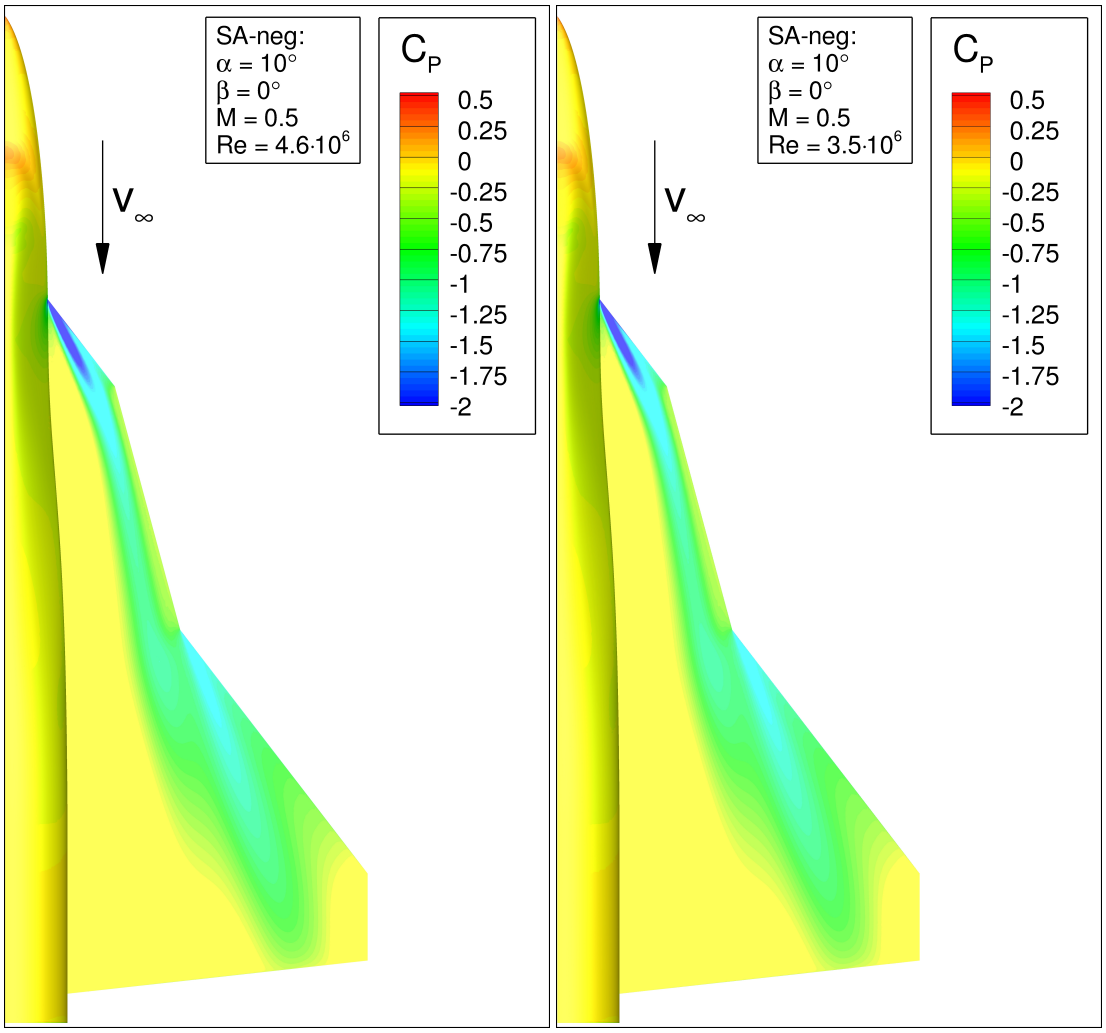
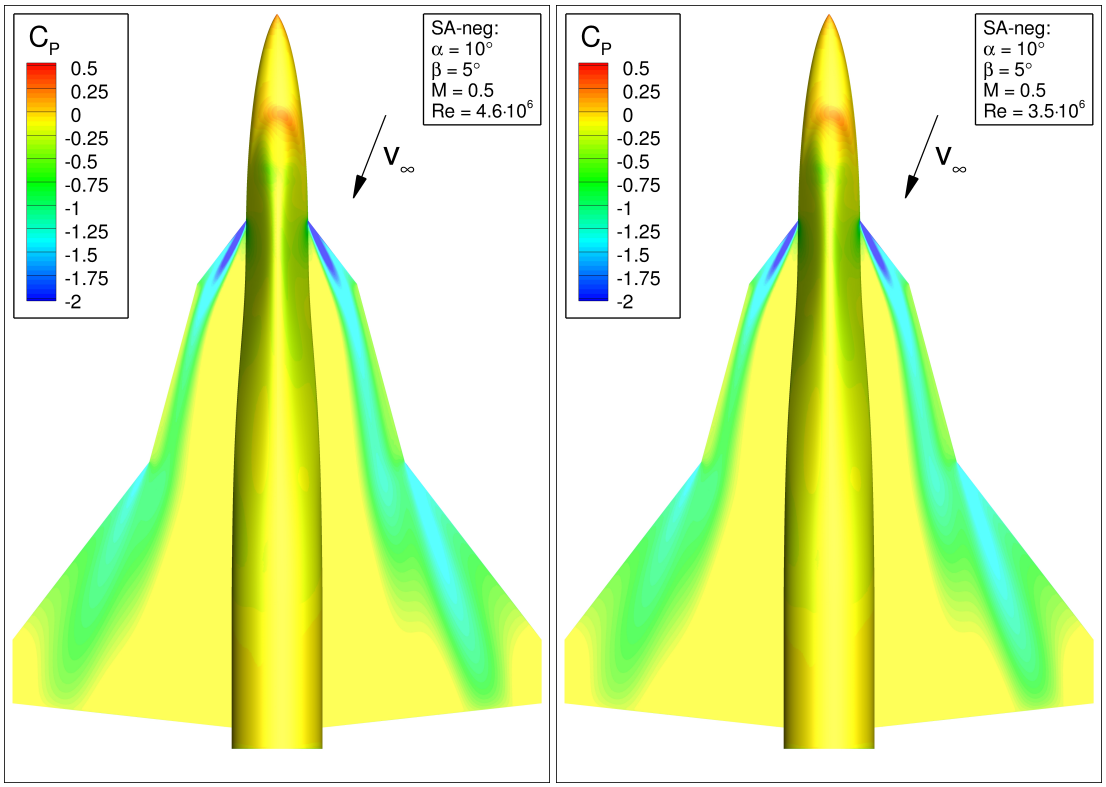



FIGURE 68: Comparison of $C_P$ values between the four turbulence models for an AoA of $\alpha = 8°$ a $x = constant$ at 2/3 of Delta 2.



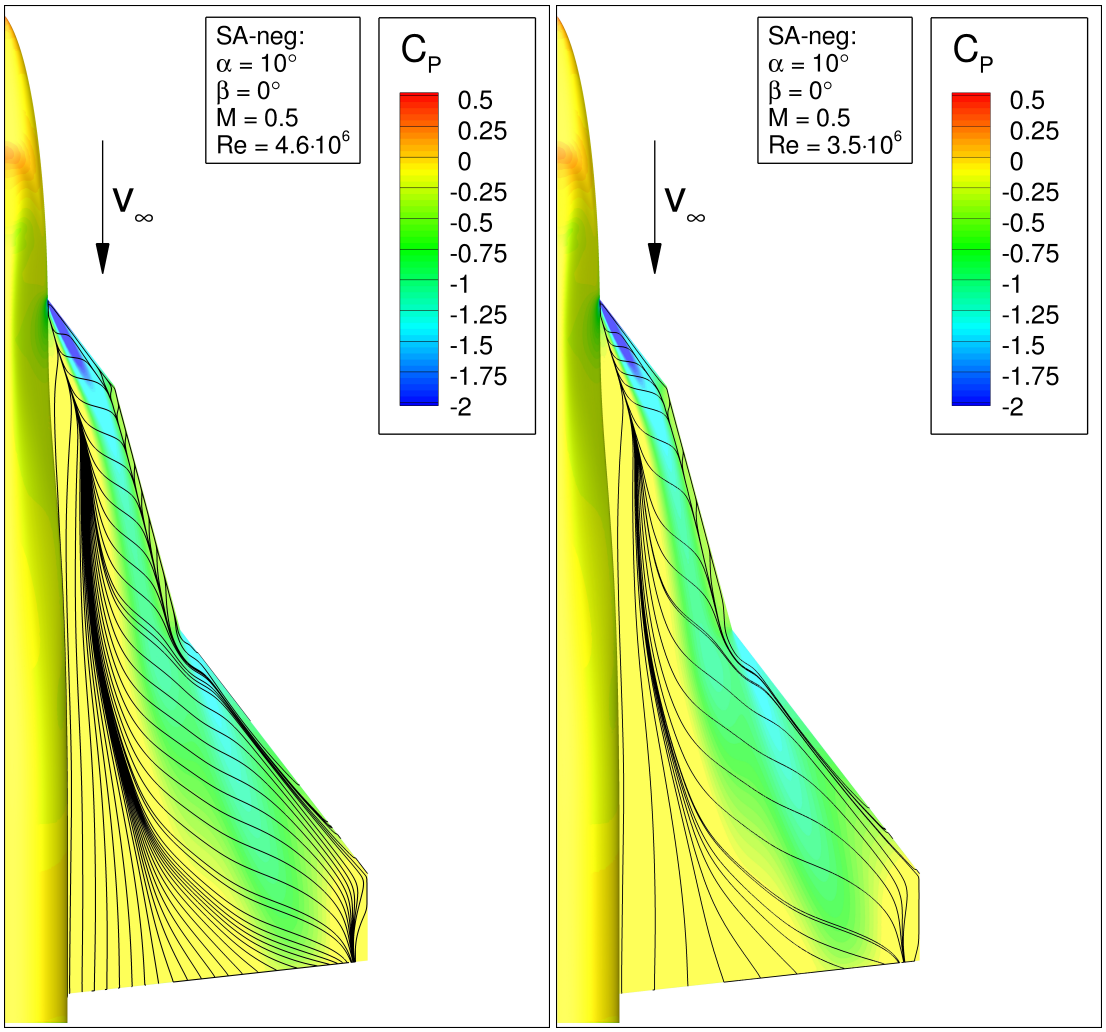

(a) (b)

FIGURE 69: $C_P$ surface distribution for an AoA $\alpha = 10°$ for a symmetric on flow condition with a Reynolds number of (a) $Re = 4.6 \cdot 10^6$ and (b) $Re = 3.5 \cdot 10^6$.



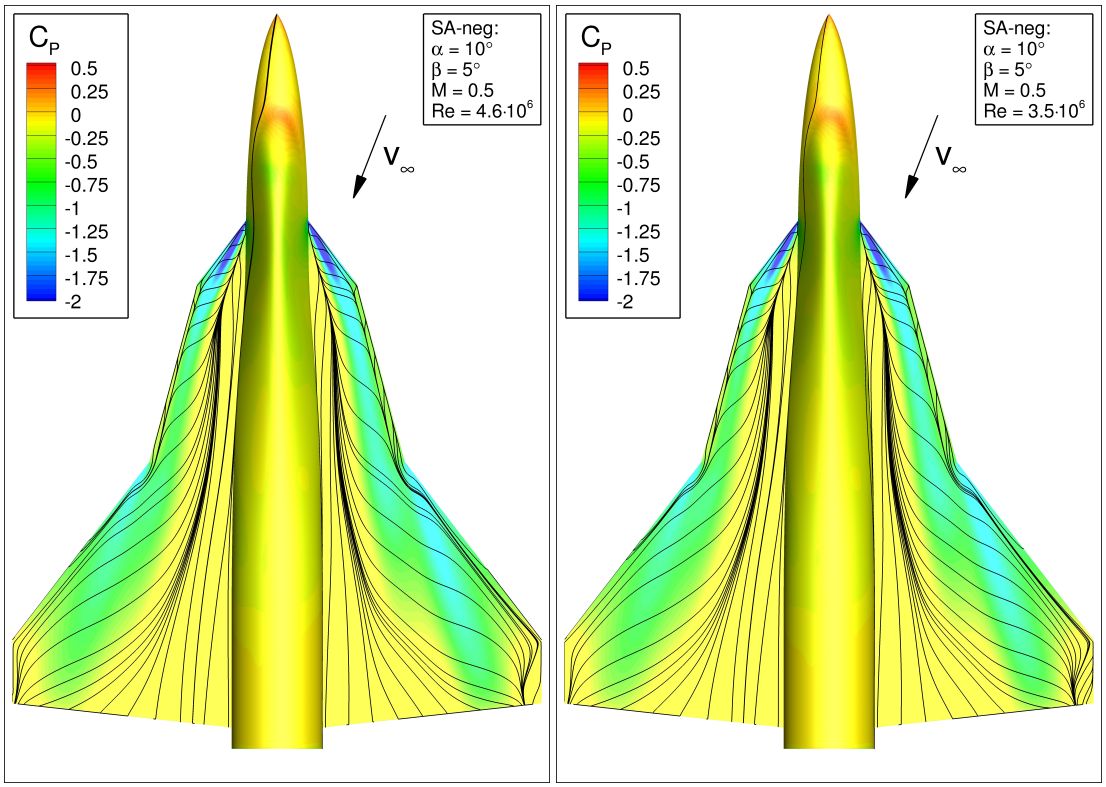

(a) (b)

FIGURE 70: $C_P$ surface distribution for an AoA $\alpha = 10°$ for an asymmetric on flow condition with a Reynolds number of (a) $Re = 4.6 \cdot 10^6$ and (b) $Re = 3.5 \cdot 10^6$.




(a) (b)

FIGURE 71: $C_P$ surface distribution with skin friction lines for an AoA $\alpha = 10°$ for a symmetric on flow condition with a Reynolds number of (a) $Re = 4.6 \cdot 10^6$ and (b) $Re = 3.5 \cdot 10^6$.




(a) (b)

FIGURE 72: $C_P$ surface distribution with skin friction lines for an AoA $\alpha = 10°$ for an asymmetric on flow condition with a Reynolds number of (a) $Re = 4.6 \cdot 10^6$ and (b) $Re = 3.5 \cdot 10^6$.

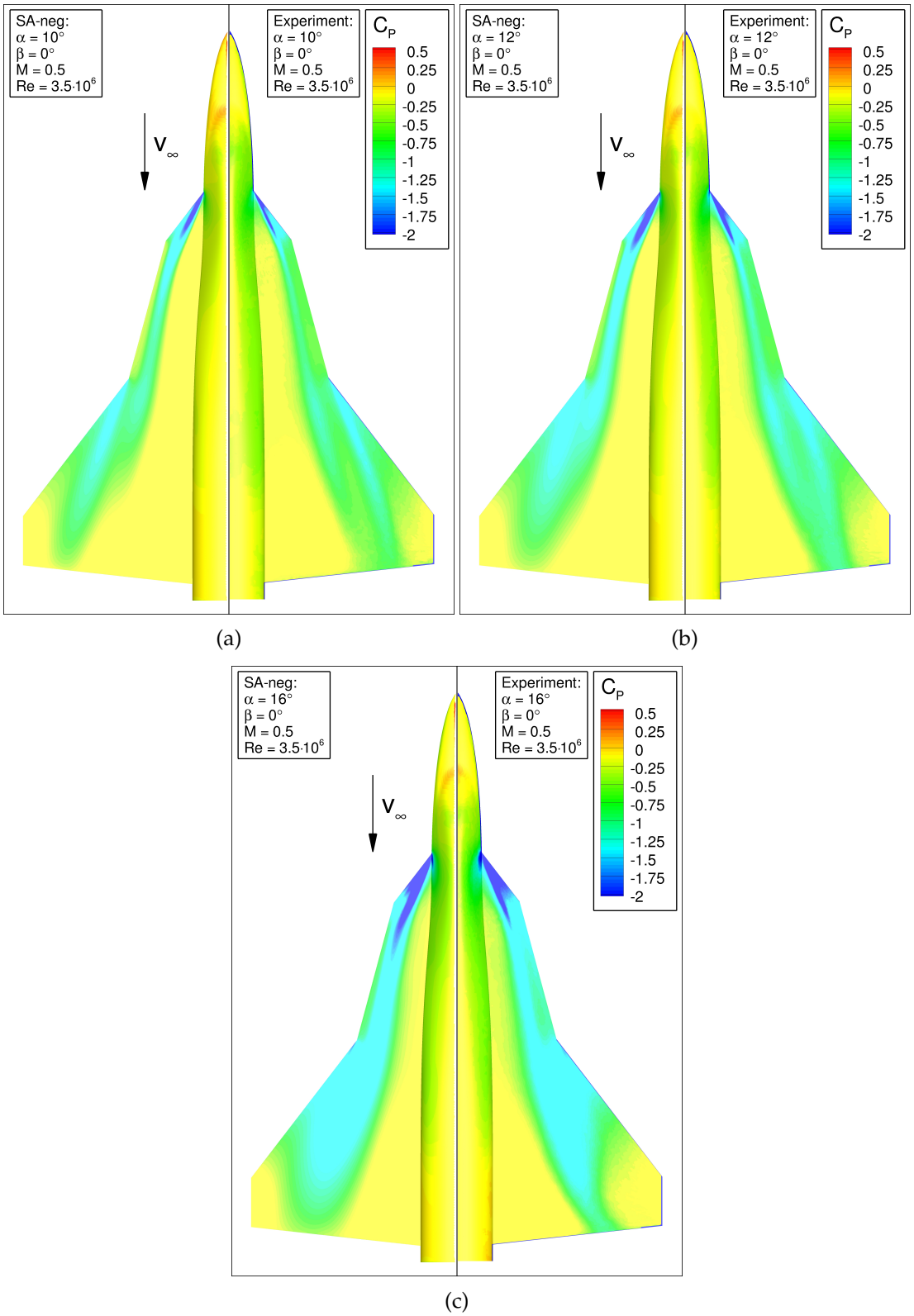
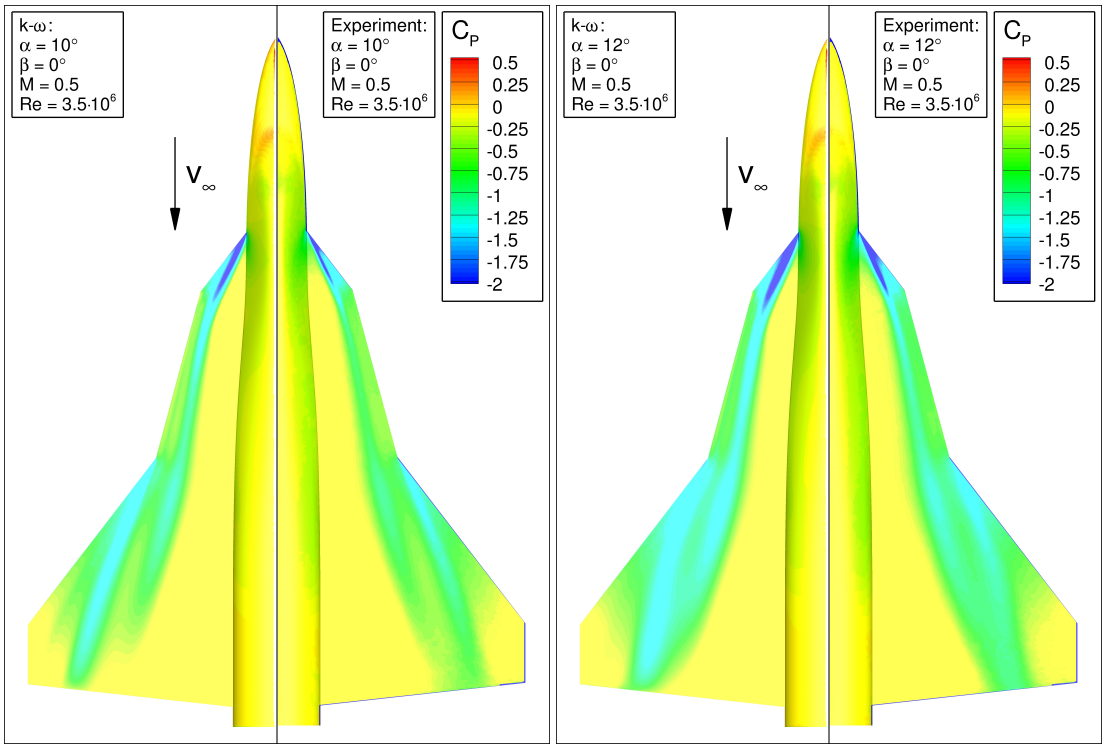



FIGURE 73: $C_P$ surface distribution resulting from SA-neg simulations for an AoA of (a) $\alpha = 10°$ and (b) $\alpha = 16°$ in comparison with PSP results.




(a) (b)

FIGURE 74: $C_P$ surface distribution resulting from k-$\omega$ simulations for an AoA of (a) $\alpha = 10°$ and (b) $\alpha = 12°$ in comparison with PSP results.

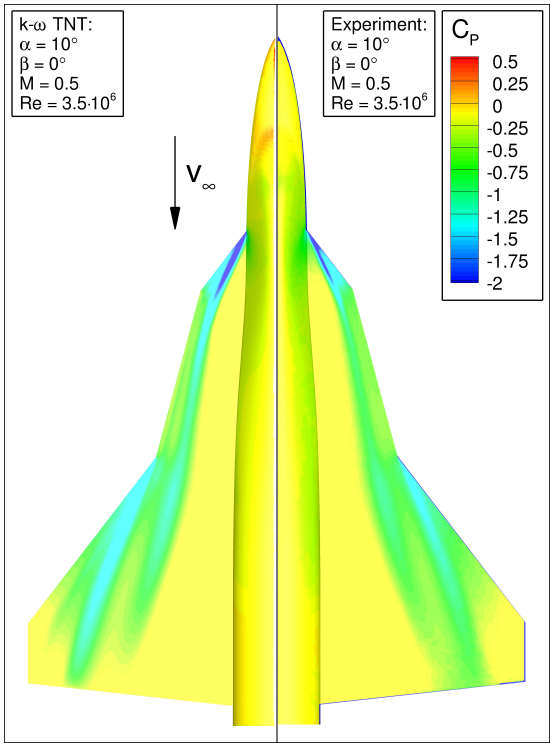



FIGURE 75: $C_P$ surface distribution resulting from k-$\omega$ TNT simulations for an AoA of $\alpha = 10°$ in comparison with PSP results.

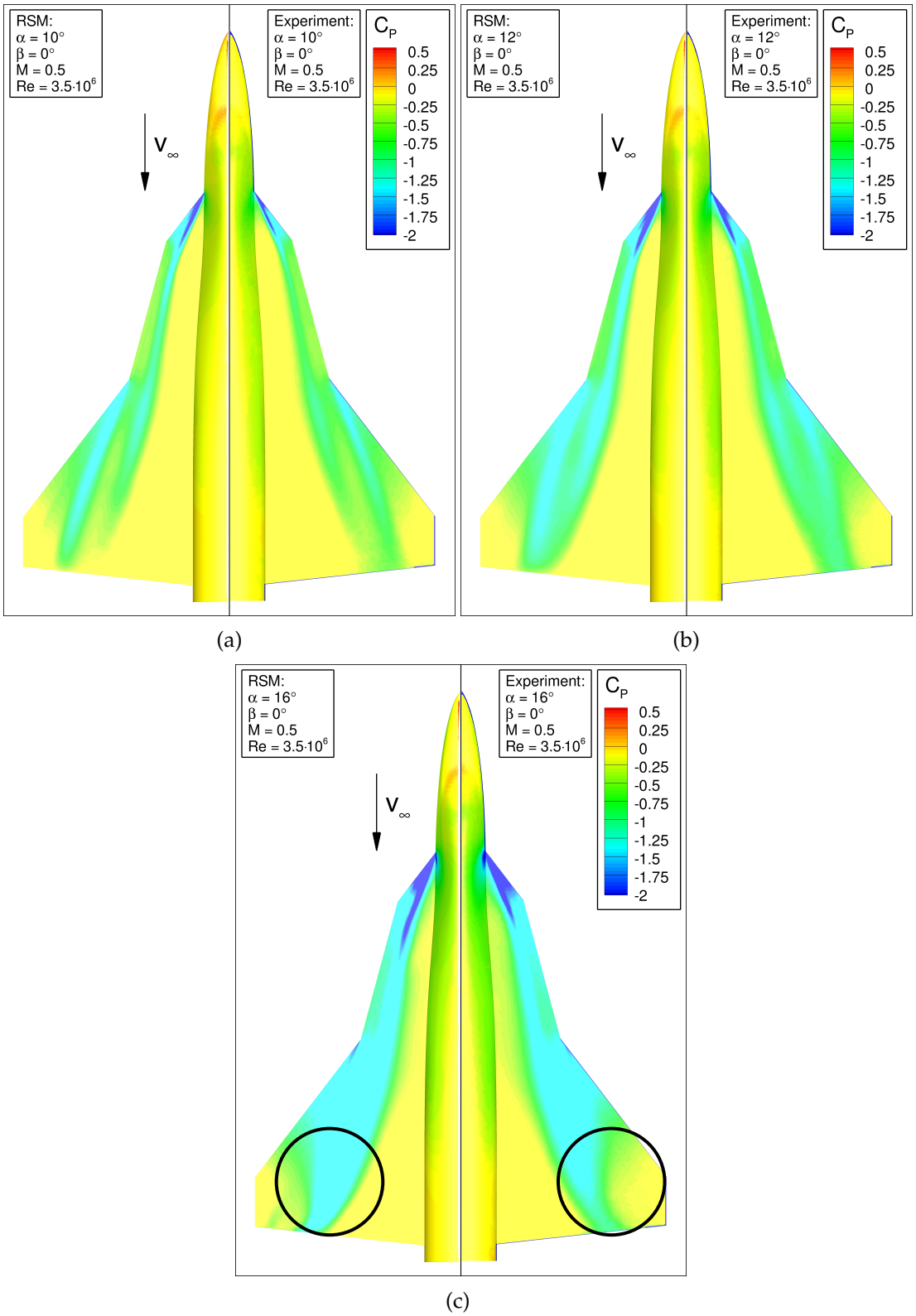
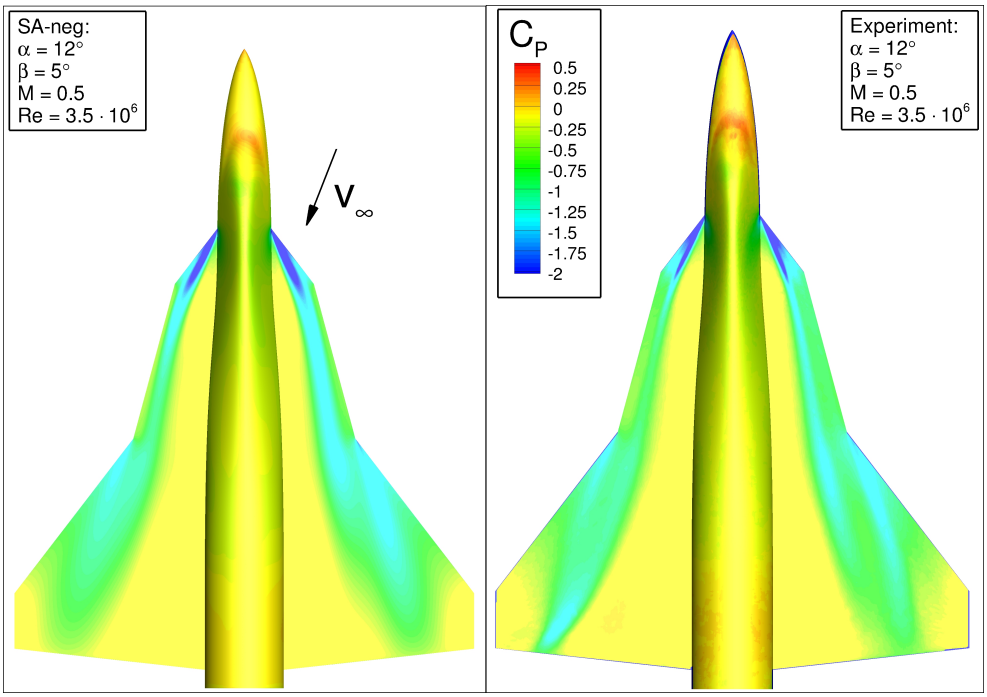
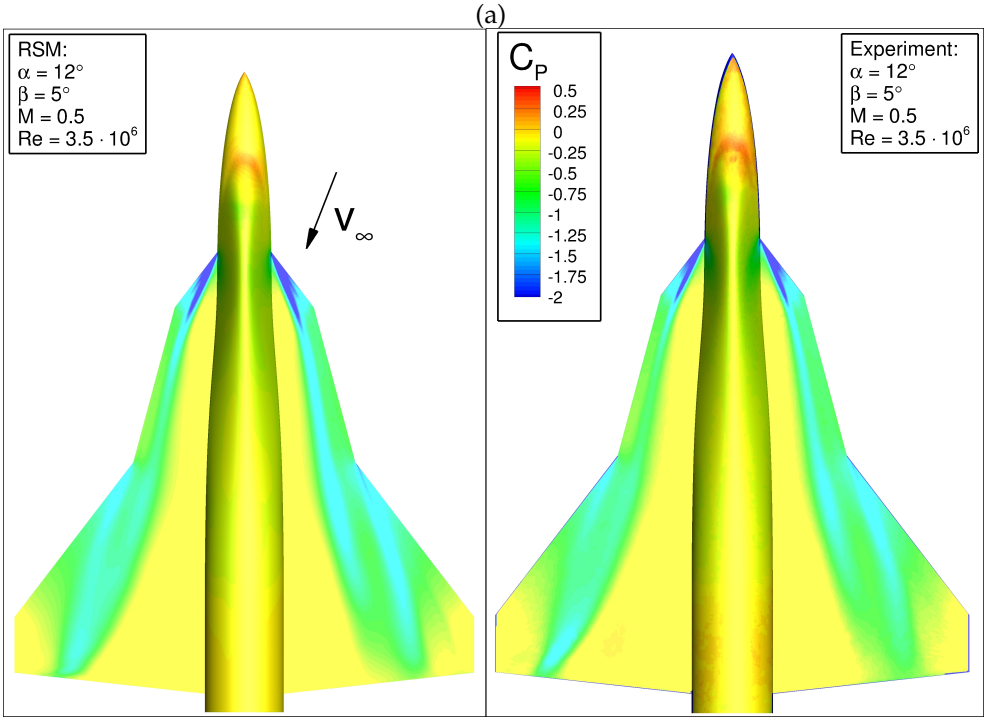



FIGURE 76: $C_P$ surface distribution resulting from RSM simulations for an AoA of (a) $\alpha = 10°$ and (b) $\alpha = 16°$ in comparison with PSP results.




(a)




(b)

FIGURE 77: $C_P$ surface distribution resulting from (a) SA-neg and (b) RSM simulations for an AoA of $\alpha = 12°$ in comparison with PSP results.